Wavelet Analysis of Geomagnetic Jerks

Tjaart de Wit

Thesis presented in fulfillment of the requirements for the degree of Masters of Science in the Department of Mathematics and Applied Mathematics and the Africa Earth Observatory Network (AEON), University of Cape Town

Supervisors

Peter Dunsby (Department of Mathematics - University of Cape Town, South Africa, *peter.dunsby@uct.ac.za*)

Pieter Kotzé (South African National Space Agency - SANSA, Hermanus, South Africa, *pkotze@sansa.org.za*)

Gauthier Hulot (Institut de Physique du Globe de Paris - IPGP, France, *gh@ipgp.fr*)

Dominique Gibert (Institut de Physique du Globe de Paris - IPGP, France, *gibert@univ − rennes1.fr*)

Plagiarism Declaration

1. I know that plagiarism is wrong. Plagiarism is to use another's work and pretend that it is one's own.
2. I have used the American Psychological Association (APA) convention for citation and referencing. Each contribution to, and quotation in this thesis from the work(s) of other people has been attributed, and has been cited and referenced.
3. This thesis is my own work.
4. I have not allowed, and will not allow, anyone to copy my work with the intention of passing it off as his or her own work.

Signature _____

Abstract

Geomagnetic jerks, or secular variation impulses, are abrupt changes in the slope of the first time derivative of the Earth's magnetic field. These changes occur on time scales of the order of a year. It has been demonstrated that the jerks might be more singular than previously supposed; their "regularity" is closer to 1.5 than to 2. Although discovered over 30 years ago, geomagnetic jerks remain poorly understood. Their origin probably lies in the magnetohydrodynamics that is responsible for the maintenance of the Earth's magnetic field produced within the Earth's liquid and convecting core (through a so-called geo-dynamo process).

A wavelet tool was programmed in MATLAB and a wavelet analysis applied to detect and characterize singular events, or jerks, in the time series made of monthly mean values of the east component of the geomagnetic field from 45 selected worldwide observatories. The analysis was first performed on various synthetic series made up of a "main" signal of smooth variation intervals separated by singular events, a white noise and an "external" signal made up of the sum of a few harmonic signals. Conditions, in which the singular events could be clearly isolated and their associated "regularities" recovered, are highlighted.

Geomagnetic jerks were detected globally in 1969, 1978, 1991 and 1999. Furthermore, geomagnetic jerks are also thought to have also occurred in 1901, 1913 and 1925, but due to the small number of observatories with long enough records to allow for detection during this period, their extent is unclear. Two further geomagnetic jerks were found to have occurred around 1937 and 1952, but due to these events not being detected by all the observatories with records covering this period, these events might not be of the same extent or origin. The results of the geomagnetic jerks detected here and the phase jumps detected in the Chandler wobble are compared and the remarkable coincidence highlighted. The spatio-temporal behaviour of jerks, for example where jerks arrive in the northern hemisphere before the southern hemisphere, is explored. Using k-means clustering, an antipodal relationship is proposed between regional trends in the time delay in the detection of geomagnetic jerks at the surface of the Earth. It is possible that this finding may shed some new light on the origin of geomagnetic jerks.

The wavelet analysis was also used to investigate whether the nature of geomagnetic jerks could be classified into one of the following three categories: geomagnetic jerks are the result of some instability starting at the time of the jerk; geomagnetic jerks are the result of some continuous oscillations; that geomagnetic jerks possibly reflect a process ending at the time of the jerk. A startling pattern emerged that suggested that the 1969 jerk corresponded to an event starting at that time, the 1978 jerk corresponding to an event ending at that time, and lastly an event again starting in 1990. This implied that the 1969 and 1978 jerks might have been the result of a common phenomenon starting in 1969 and ending almost a decade later in 1978.

Contents

List of Figures

List of Tables

List of Symbols

t time (months)

α regularity of a singularity

a dilation parameter

β singularity coefficient

$\psi(t)$ analysing wavelet as a function of time

$r_j(a)$ ridge function associated with the j^{th} line of maxima as a function of dilation.

List of Acronyms

AMSL above mean sea level

CMB core-mantle boundary

IAGA International Association of Geomagnetism and Aeronomy

INTERMAGNET International Real-time Magnetic Observatory Network

TRM Thermo-remanent magnetism

WDC World Data Centre

WMMD World Monthly Mean Database

Chapter 1

Introduction

The Earth's interior is made up of four major layers or spherical shells - the solid outermost lithosphere (including the crust), the viscous silicate mantle, the liquid iron outer core and the solid iron inner core (e.g. Figure 1). This structural layering of the Earth's interior was largely uncovered using seismological methods - the travel times of reflected and refracted seismic waves created by earthquakes and artificial detonations, providing insight into the materials they passed through. Like the ringing of a giant bell, longitudinal compressional P-waves and transverse shear S-waves (at speeds of about 10 $km.s^{-1}$) reflect and refract as they encounter discontinuities in the material they are travelling through (Appell, 2012).

Evidence for the existence of a core was first given by Oldham in 1906 (Davies, 1999). It was inferred that the core of the earth was liquid since it transmitted P-waves but not S-waves; the latter of which cannot pass through liquids, as liquids do not shear (Davies, 1999). Furthermore, in 1936, Inge Lehmann first realized the Earth had a solid inner core after carefully examining the P-waves through this region (e.g. Lehmann, 1936, 1987). Further evidence for a solid inner core have been found in shear-mode body waves (converted P-waves) that traverse it, albeit difficult to detect (Wookey and Helffrich, 2008).

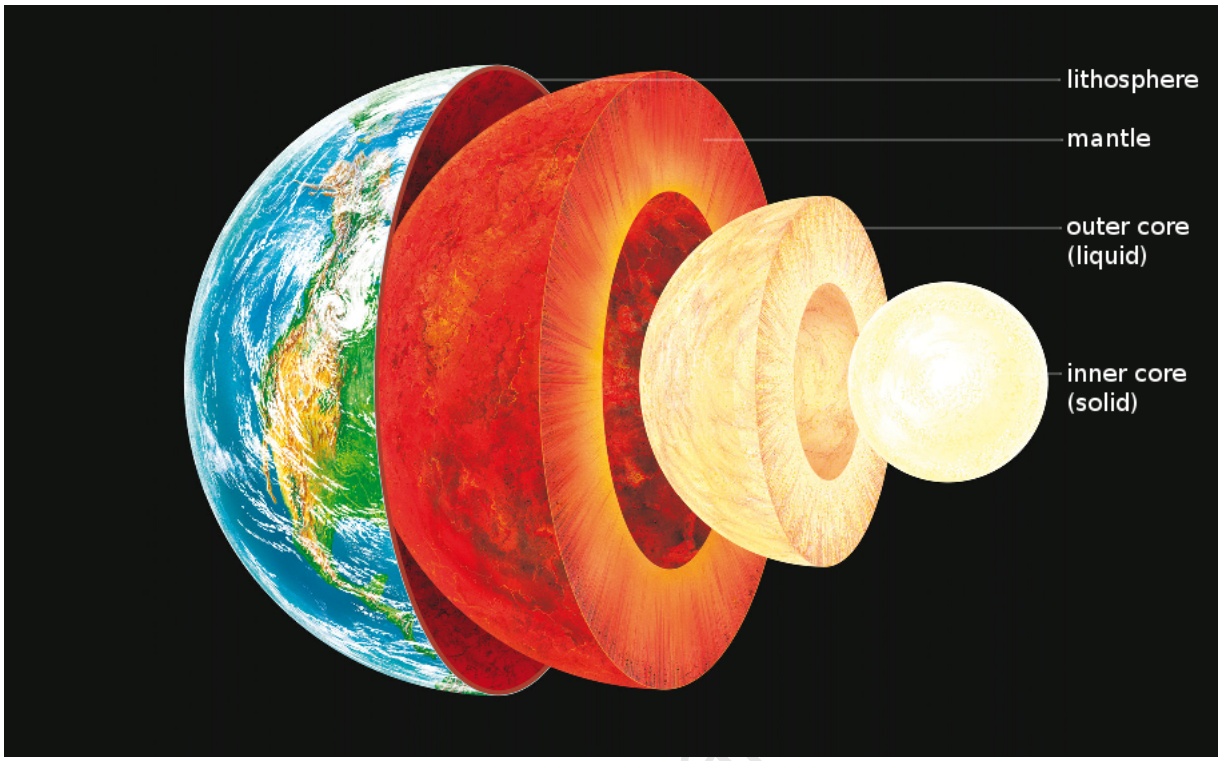

Figure 1: The internal structure of the Earth. (Modified from Appell, 2012)

The Earth is thought to have begun about 4.6 billion years ago as a near-homogenous molten mixture, heated by large meteorite impacts and radioactivity, from which iron and silicate minerals crystallized and separated differentially due to their vastly different crystallization temperatures and densities. During this process, the liquid iron core formed from molten iron draining towards the centre of the Earth, greatly increasing the temperature of the Earth due to the change in gravitational energy (Anderson and Hanks, 1972). From the analysis of ancient rocks found in South Africa's Barberton greenstone belt, the Earth's magnetic field, produced by a geo-dynamo, is thought to have been present at least as early as 3.45 billion years ago (Tarduno et al., 2010). It is believed that over the past billion years or so, solidification of iron started to form an inner core, which, over time, slowly grew in size to its present size of approximately 1220 km in diameter (Tarduno et al., 2010, Figure 2).

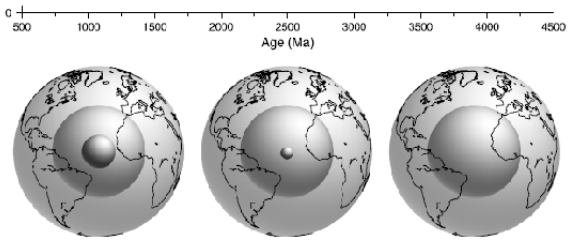

Figure 2: Visually highlights the growth of the inner core over time. (Source Tarduno et al., 2006)

The liquid outer core is believed to be made up of predominately iron, of very low viscosity, but possibly mixed with nickel. Evidence for this has come from metallic iron to be commonly found in iron meteorites and its abundance on the sun. Furthermore, laboratory experiments, at appropriate temperature and pressures, have identified iron as the likely candidate. Although, evidence also indicates that lighter elements constitute a significant portion of the core material (perhaps 10-20%) to match the observed seismic properties of the inner and outer core (Davies, 1999). It is thought that these lighter elements, namely hydrogen, carbon, nitrogen, oxygen, sulphur and silicon, could have been included in the core during the accretion of the early Earth (Helffrich and Satoshima, 2010).

The solid inner core formed and grew after slow cooling lead to liquid iron freezing. This crystallization process is thought to provide the energy to drive thermal and chemical convection in the liquid outer core. As iron solidifies at the inner core boundary, lighter elements separate and rise upwards to the core-mantle boundary (CMB) to assist thermal currents in driving convection in the outer core (e.g. Pozzo et al., 2012; Gubbins, 2008).

Seismic data from the core reveals that the inner core is anisotropic and suggests that the rotation rate of the inner core is faster (about 1° per year) than the rotation of the mantle and crust, so-called super-rotation (Song and Richards, 1996). Seismic properties have also shown remarkable differences between the west and east hemispheres of the inner core (e.g. Bergman, 2010; Buffett, 2010). From this data it has been proposed that as the Earth's inner core grows, material moves laterally within the core inducing melting and solidification on the opposite hemispheres (Buffett, 2010). Figure 3 shows how it is thought that this asymmetry between the eastern and western hemispheres could be coupled with mantle convection and related lithospheric plate motion by helical convection currents in the outer core (e.g. Aubert et al., 2008; Lister, 2008).

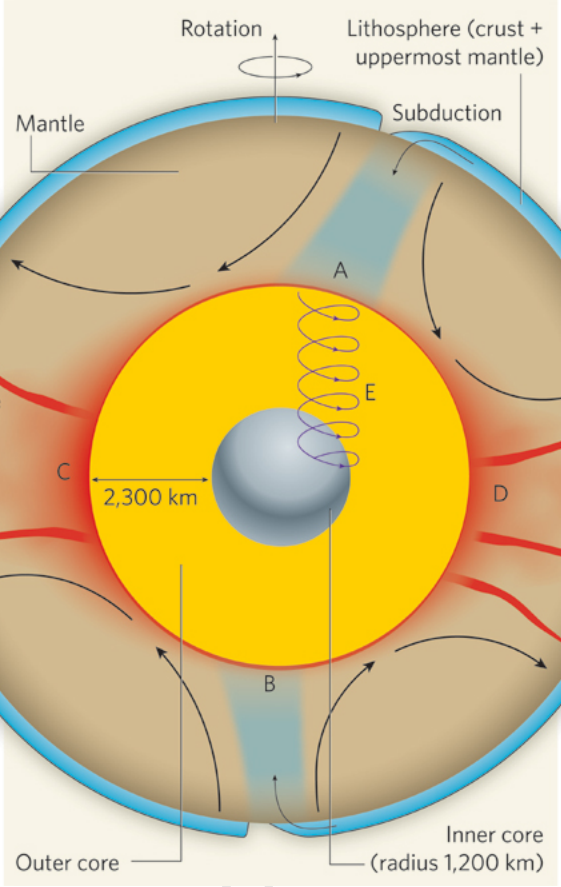

Figure 3: Schematic section through the Earth's interior showing how mantle convection and lithosperic plate recycling at subduction zones maybe related to helical convection currents in the inner core via the heat flux across core-mantle boundary, and subsequent correlation to solidification at the inner core boundary. The heat flux out of the outer core is greater below subduction zones (A and B), like the Pacific "rim of fire", causing more rapid convection in the liquid outer core and greater melting rates at the inner core boundary below these zones. Conversely, less heat is extracted from the outer core through upwelling "plumes" (C and D) along the equatorial regions where they manifest themselves as hot-spots such as Hawaii in the central Pacific. This is thought to provide an explanation for the asymmetry between the eastern and western hemispheres of the inner core found in seismological evidence. (Source: Lister, 2008)

1.1 The Earth's Magnetic Field

The main Earth's magnetic field, or geomagnetic field, is predominately dipolar with antipodal North and South magnetic poles, but it also has significant multipolar components. The Earth's total magnetic field is therefore the superposition of various magnetic fields of differing sources (Olsen et al., 2007).

The "internal field", or "field of internal origin", is generally recognized as the sum of the main field and crustal field since both originate within the Earth (Olsen et al., 2007).

The main field of the Earth's magnetic field is thought to be generated by a self-sustaining geo-dynamo in the fluid outer core (Olson, 2007). The fluid flow in the outer core (on the order of $\sim 1\,\mathrm{mm.s^{-1}}$) is thought to be generally driven by thermal and chemical convection in helical patterns and although the Earth's rotation affects the alignment of these helical convection currents along the rotational axis, it does not drive it (Gubbins, 2008).

The details of fluid flow patterns in the outer core are complex and turbulent, much like weather systems - determining these flow patterns has been a focus of much research. To calculate the flow patterns throughout the outer core would require knowledge of the entire magnetic field, but our knowledge of the magnetic field does not extend deep into the core because of the high conductivity of the core, restricting mapping the fluid flow to the core-mantle boundary (Bloxham and Jackson, 1991), but data assimilation could help circumvent this (Fournier et al., 2010).

The crustal field is produced by magnetized rocks, found in the Earth's crust. Rocks in the Earth's upper crust retain a fossilized temporal record of the Earth's magnetic field. When rocks cool below the Curie point (about $600^{\circ}C$), magnetic minerals in the rocks become permanently magnetized by, and in the direction of, the present ambient magnetic field, called thermo-remanent magnetism, TRM (Olsen et al., 2007). These minerals lock-in a record of the intensity and direction of the magnetic field at the time of cooling. The Curie temperature of the Earth's crust varies with magnetic mineralogies, but is approximately $580^{\circ}C$ as this is the Curie temperature of Magnetite - a common magnetic mineral in the Earth's crust (Tanaka et al., 1999). The crustal field is the combination of the permanent magnetization and induced magnetization of magnetized rocks inside the solid Earth. The crustal field is weaker, on average, than the main field, but is spatially very variable resulting from complex crustal compositions and concentrations of magnetized rocks (Olsen et al., 2007).

The "external field", "or field of external origin", is made up of magnetic fields caused by electrical currents in the ionosphere ("ionospheric field") and magnetosphere ("magnetospheric field"). The "ionospheric field" is produced by currents in the ionosphere driven by a dynamo process of plasma in the ionosphere moving within the main field (Olsen et al., 2007). The "magnetospheric field" is produced by currents formed from the movement of charged particles in the magnetosphere distorting the shape of the internal field (Olsen et al., 2007). The Earth's magnetic field shields the Earth from this flow of charged particles emitted by the Sun (solar wind), which would otherwise strip away the atmosphere.

One of the most enigmatic features of the Earth's magnetic field is that it episodically reverses polarity. These reversals can be observed in the history of the Earth, fossilized in its rocks. The reversal patterns were first identified in lava flows and baked clay, but are best observed from magnetic stripes on the ocean floor (Gubbins, 2008). As two tectonic plates move apart, oceanic crust forms and becomes permanently magnetized by the present ambient magnetic field, forming a pattern of stripes. By combining absolute dating techniques to approximate the age of these rocks, the past orientation of the magnetic field (chrons) can be elucidated (e.g. Figure 4). Periods, or more accurately episodes,

in the Earth's history when the magnetic field did not reverse polarity for long periods of time are called superchrons (Figure 4).

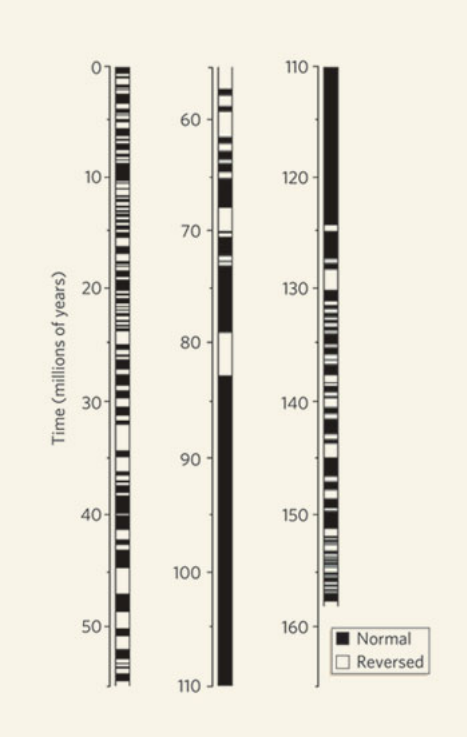

Figure 4: Timeline of reversal periods and frequency of which during the past 160 million years. The black and white intervals indicate episodes (chrons) when the magnetic field was oriented normally and of opposite polarity, respectively. The so-called Cretaceous normal superchrons during which no reversals took place is clear from about 85-125 million years ago. (Source: Gubbins, 2008)

Through the study of the Earth's magnetic field recorded in rocks (paleomagnetism), it has been revealed that the main field has remained predominantly an axial dipole, except for relatively short periods of time leading up to a reversal ($\sim 10{,}000$ years) when the main field weakens considerably and becomes dominated by non-dipole components. This weakening of the magnetic field is followed by either a geomagnetic reversal or a geomagnetic excursion (the pole orientation varies from its original position by up to 45 degrees), before returning back to a "stable polarity" (Hulot et al., 2010). The Earth's magnetic field has reversed its polarity several hundred times during the past 160 million years with a reversal taking approximately $1{,}000 - 6{,}000$ years to complete (Glatzmaier et al., 1999) and having an average interval of $300{,}000$ years between reversals (Gubbins, 2008). The last geomagnetic reversal occurred $780{,}000$ years ago, followed by about 14 major geomagnetic excursions occurring since then (Glatzmaier et al., 1999). Biggin et al. (2008) have highlighted that polar reversals have happened more frequently in recent times

than in the past, and that this could suggest a more stable magnetic field being related to a smaller inner core size, compared to the inner core size it has grown to at present. Further suggestion has been made that variability of the geomagnetic field on very long time-scales may be related to changes in heat flow associated with mantle convection processes. Periods during which the geo-dynamo experienced high reversal frequency, perhaps due to a high heat flux out of the core across the core-mantle boundary, could be associated with a weak dipole component of the geomagnetic field and vice versa (Biggin et al., 2012).

1.2 Detecting the Earth's magnetic field

The Earth's magnetic field has been used for many centuries by humans for navigation by utilising a compass needle roughly orienting itself towards geographic North. Bacteria, some fish, birds and sea turtles have also been found to use the Earth's magnetic field to guide them during natal homing (Lohmann et al., 2008). Rapid changes in the Earth's magnetic field could subsequently disrupt this natal homing process.

Discoveries of temporal changes in the Earth's magnetic field brought about the establishment of magnetic observatories to monitor these changes for navigation purposes and to regularly update magnetic field maps (Hulot et al., 2010). Magnetic observatories were first established in the 19th century following work done measuring the Earth's magnetic field by German scientist Carl Friedrich Gauss (Love, 2008). Some geomagnetic observatories have been continuously monitoring the Earth's magnetic field ever since. Modern geomagnetic observatories use highly accurate (to about $1\,nT$) magnetometers to measure the vector components and the total intensity of the magnetic field at intervals of as short as 1 second. Magnetic measurements taken are typically given in a local "topocentric" coordinate system relative to the reference ellipsoid. The magnetic components X, Y and Z of a magnetic field vector are given along the axes pointing towards geographical north, geographical east and vertically down respectively (Figure 5). These can also be derived from the the angular measurements D and I in conjunction with the intensity of the magnetic field vector. D, or declination is the angle between geographical north and the horizontal direction in which a compass needle would point, and I, or inclination, is the angle between the horizontal plane and the field vector (Olsen et al., 2007).

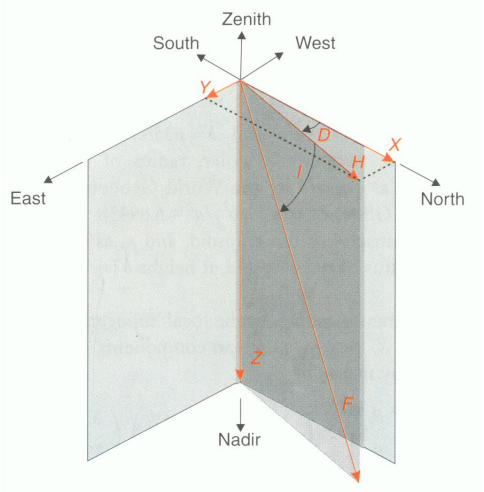

Figure 5: The magnetic elements in the local topocentric coordinate system, seen from the northeast. (Source: Olsen et al., 2007)

Currently, INTERMAGNET and the World Data Centre (WDC) collect and compile magnetic observatory data from almost all of the observatories worldwide (Olsen et al., 2007). INTERMAGNET (`www.intermagnet.org`), is a global network of geomagnetic observatories that has 128 observatories collaborating standardized magnetic observatory data. Unfortunately, geomagnetic observatories are not evenly spread around the globe, with many geomagnetic observatories clustered in the European region (e.g. Figure 6).

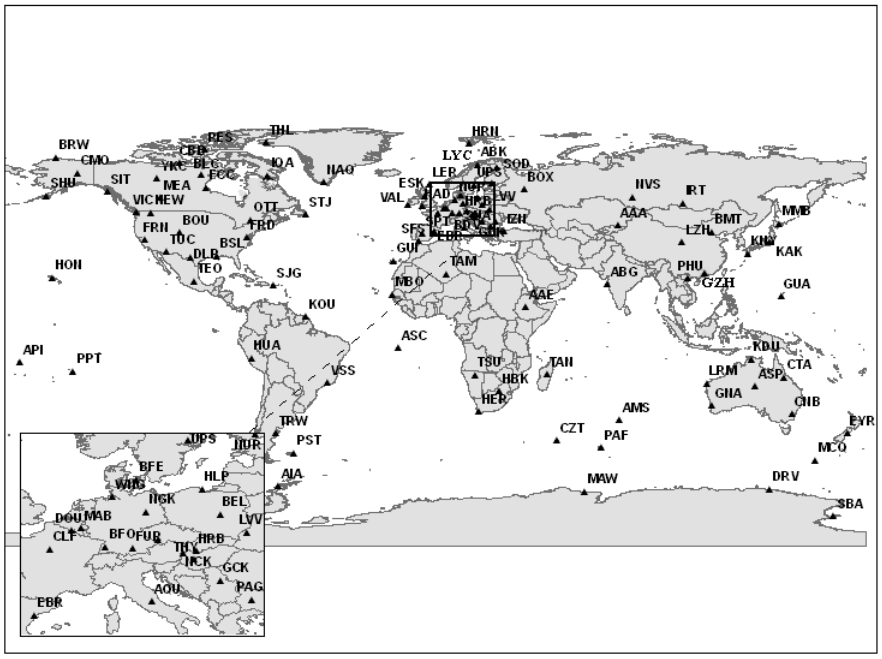

Figure 6: Worldwide locations of the magnetic observatories in the INTERMAGNET Network. Note the unequal distribution of these observatories, resulting in less data from the southern hemisphere (Source: INTERMAGNET, 2010).

The introduction of satellites brought about navigation with GPS, but also ushered in a new era of global magnetic observations. The first magnetic measurements from space were taken by the Sputnik 3 satellite in 1958 (Olsen et al., 2007). Thereafter many satellites, such as POGO, OGO, Magsat, Ørsted, CHAMP, Ørsted-2, Swarm (Table 1), have been taking measurements of the Earth's magnetic field.

Table 1: Table outlining the history of high-precision magnetic satellites (from Olsen et al., 2007 and private communication with Gauthier Hulot, 2012).

Satellite	Period of Operation	Altitude (km)	Type of data recorded
OGO-2	1965-1976	410-1510	Scalar only
OGO-4	1967-1969	410-910	Scalar only
OGO-6	1969-1971	400-1100	Scalar only
Magsat	1979-1980	325-550	Scalar and vector
Ørsted	1999-present	650-850	Scalar and vector
CHAMP	2000-present	350-450	Scalar and vector
Ørsted-2	2001-2004	698-705	Scalar only
Swarm	2013-2017	530-450	Scalar and vector

This satellite data has significantly contributed to our understanding of the evolution of the Earth's magnetic field over time (Olsen et al., 2007), and has enabled the emergence of substantial new research relating to the changing of the Earth's magnetic field. Although not using satellite data, Courtillot et al. (2007), for example, showed that a correlation may exist between climate and magnetic field variations, albeit rather controversially in the field of climate change research. Furthermore, studying the time-varying geomagnetic field is one of the best means of gaining information about the core dynamics, particularly fluid flow at the core surface (Alexandrescu et al., 1995).

1.3 Geomagnetic jerks

Secular variation is the non-periodic, long-term trend of the geomagnetic field (Olsen and Mandea, 2007; Mandea et al., 2010). Geomagnetic jerks, or secular variation impulses, are abrupt changes (on the order of $2-40\,nT.yr^{-2}$) in the secular variation. They are singular events occurring at the time of a sudden change in the gradient of the first time derivative of the geomagnetic field (Figure 7). These events occur on time scales of the order of a year.

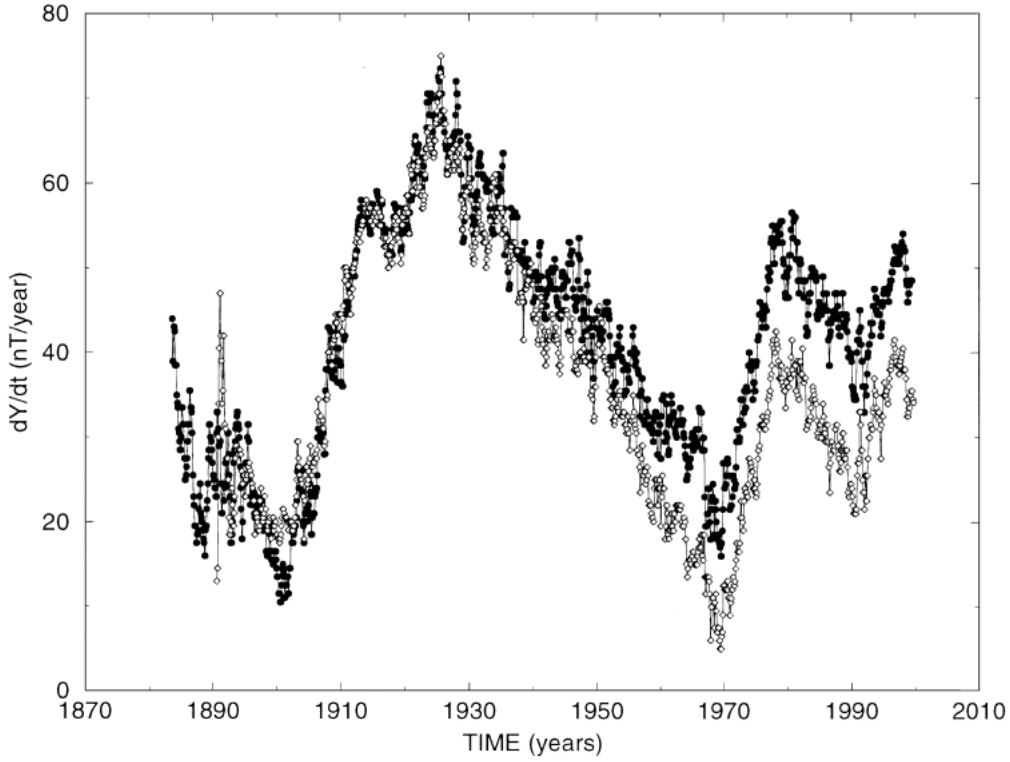

Figure 7: The secular variation, in nT per year, of the East magnetic component $\left(\frac{dY}{dt}\right)$ for Chambon la Forêt Observatory (solid circles), from 1883 to 2000 and Niemegk Observatory (opaque diamonds), from 1890 to 2000 (Source: Mandea et al., 2000).

Courtillot et al. (1978) were the first to observe a geomagnetic jerk. The jerk took place in 1969 and was detected after they found that they needed to combine two parabolic trends instead of one to model the data around the late 1960s (Courtillot et al., 1978). However, Alldredge (1984) highlighted that the method of piecemeal fitting of parabolas to the data will always create a discontinuity in the secular acceleration where the parabolas join and that the place where the parabolas join is an *a priori* assumption and not a result of the analysis.

Since then many other studies (Mandea et al., 2010 and references therein) using geomagnetic observatory data have noted geomagnetic jerks to have also occurred in 1978, 1991, 1999, 2003 and also possibly 1901, 1913, 1925, 1932 and 1949, although the latter group of jerks were not detected at every observatory on the globe and few observatories have monthly mean magnetic data extending to these early epochs. These studies used a variety of techniques to detect and characterise geomagnetic jerks including piece-wise regression analysis (e.g. Le Huy et al., 1998; Pinheiro et al., 2011) and wavelet analysis (e.g. Alexandrescu et al., 1995, 1996; Rotanova et al., 2003).

Wavelet analysis is a technique used to study abrupt changes in signals, and Alexandrescu et al. (1995) pioneered the wavelet analysis technique to determine exactly when geomagnetic jerks occurred. Wavelet analysis is well suited to detecting localized singular events without any *a priori* assumptions. Alexandrescu et al. (1996) then applied the same technique to magnetic observatory data from observatories worldwide. Although geomagnetic jerks are most readily observed in the East (Y) component of observatory magnetic data (as this component is the least contaminated by external fields, see figure 5), Alexandrescu et al. (1996) analysed both the North (X) and East (Y) components to determine the direction in which a geomagnetic jerk was strongest. This study went on to assess the spatial characteristics of geomagnetic jerks showing that some geomagnetic jerks do not occur at the same time all over the globe. They showed that the geomagnetic jerks in 1969 and 1978 arrived first in the northern hemisphere, then 'lagged' behind in the southern hemisphere. It was hypothesized that this could be due to the mantle behaving like a causal time-invariant real linear filter (Backus, 1983) and thus the delay was thought to be because of regional differences in mantle conductivity. Furthermore, Pinheiro and Jackson (2008) demonstrated that a simple mantle electrical conductivity model was able to generate differential jerk time delays that could account for this regional "lag" effect. However, Holme and de Viron (2005) suggested that each jerk might rather consist of two separate events, than a single event delayed in parts of the world.

Mandea et al. (2000) hinted of a geomagnetic jerk occurring in 1999, whereafter Olsen and Mandea (2007) detected a geomagnetic jerk possibly occurring in 2003 using monthly mean satellite magnetic data from CHAMP collected during 2001 to 2005. Olsen and Mandea (2007) went on to also highlight the regional trends of secular variation in their analysis of the 2003 jerk and suggested that geomagnetic jerks, or at least the 2003 jerk, need not be worldwide phenomena, and, significantly, that the 2003 jerk was strongest in the vertical component (Z) rather than just the horizontal

components used in other studies (e.g. Alexandrescu et al., 1995, 1996). Furthermore, using global geomagnetic models, Chambodut and Mandea (2005) estimated the occurrence dates of geomagnetic jerks and also found that geomagnetic jerks might not have been worldwide in occurrence. A geomagnetic jerk was also detected occurring in 2007 by Chulliat et al. (2010) using a similar method to Olsen and Mandea (2007), and went on to show that the 2003 and 2007 jerks could be explained by a single core field acceleration pulse occurring in 2006.

1.3.1 Chandler wobble, length of day variations and geomagnetic jerks

The Earth's rotation is not constant - both the rate of rotation and position of the rotation axis vary with time. Sudden variations in the Earth's rotation have been found to have remarkably similar timing to geomagnetic jerks.

The variation of the position of the rotation axis with respect to the Earth's surface is called "polar motion" and with respect to inertial space is called "nutation". This variability of polar motion has been well observed over the past 150 years. At the end of the 19^{th} century, American astronomer S.C. Chandler, showed that this motion was made up of the sum of two periodic oscillations - annual oscillations and the so called Chandler wobble (Wahr, 1988). The Chandler wobble component having been shown to have a period of approximately 434 ± 0.5 solar days (Gibert and le Mouël, 2008). The amplitude of the Chandler wobble varies with time, and so does its phase. Furthermore, the phase of the Chandler wobble has also been shown to have undergone rapid changes (phase jumps) over time, which have shown a remarkable correlation to the dates of geomagnetic jerks (e.g. Gibert et al., 1998; Bellanger et al., 2001, 2002; Gibert and le Mouël, 2008). Various mechanisms driving the Chandler wobble have been proposed, from atmospheric variations to earthquakes (Gibert and le Mouël, 2008), but Wahr (1988) highlighted that these excitation sources might not be able to provide the necessary power to catalyze the wobble, so he proposed that core motions outlined by Gire and le Mouël (1986) might be exciting the Chandler wobble - thus indicating an internal origin of the Chandler wobble. Bellanger et al. (2001) have showed that strong core-mantle torques ($\sim 10^{20}\,Nm$) might further explain the phase jumps in the Chandler wobble.

Changes in length-of-day (LOD) are directly proportional to variations in the rotation rate (Wahr, 1988). The rotation rate of the Earth is known to vary on long time-scales due to tidal torques and on shorter time-scales (of the order of a year) from the exchange of angular momentum between the atmosphere and the Earth (Holme and de Viron (2005); and references therein). After removing contributions from atmospheric angular momentum from high resolution length-of-day data, Holme and de Viron (2005) showed that inflexions (or "wiggles") in the first time derivative of splines fitted to the LOD data series correlated to the occurrence of geomagnetic jerks and suggested a direct link between geomagnetic jerks and length-of-day variations; although this was disputed by Mandea et al. (2010).

Considering the coincidence of singular events found in length-of-day variations and polar motion data, a common

mechanism could be at their origin.

1.3.2 Origin of geomagnetic jerks

The method of spherical harmonic analysis was originally developed by Gauss to determine whether the main Earth's magnetic field was of internal or external origin. The internal origin of geomagnetic jerks was first established by Malin and Hodder (1982) also using spherical harmonic analysis, and further studies have also confirmed this internal origin of geomagnetic jerks (Le Huy et al., 1998). Because jerks were still detectable at the Earth's surface after passing through the mantle, the internal nature and short time-scale (of the order of a year) of geomagnetic jerks then implied a much lower value for mantle conductivity than previously thought (Malin and Hodder, 1982). As geomagnetic jerks diffuse from the core-mantle boundary (through the mantle) to the Earth's surface, they should undergo distortion. Alexandrescu et al. (1999) determined the distortion of a pure singularity as it traversed the mantle by looking at ridge functions formed from a wavelet analysis of the distorted singularity. This yielded an estimate of the electrical conductivity of the mantle of less than $10\,Sm^{-1}$, which agreed with values obtained from high pressure experiments of a silicate mantle (Shankland et al., 1993).

Given the internal origin of geomagnetic jerks, it is clear that geomagnetic jerks originate in the magnetohydrodynamics responsible for the maintenance of the Earth's magnetic field produced within the Earth's liquid and convecting core. Bloxham et al. (2002) suggested that geomagnetic jerks are due to changing fluid flow at the core-mantle boundary based on their short time-scales. They go on to suggest that geomagnetic jerks could be explained by a combination of steady flow and simple time-varying, axisymmetric, equatorially symmetric toroidal zonal flow - so called torsional oscillations (Figure 8), but this has been questioned by various authors (e.g. Wardinski et al., 2008; Silva and Hulot, 2012).

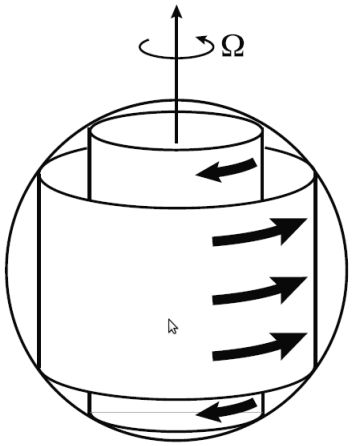

Figure 8: Visual representation of torsional oscillations thought to be related to the origin geomagnetic jerks. (Source: Hulot et al., 2010).

It has also been suggested that geomagnetic jerks are produced by a sudden change in the rate of flow of the fluid at the CMB (Le Huy et al., 1998). Considering the remarkable correlation between geomagnetic jerks, length-of-day variations and phase jumps in the Chandler wobble, another proposed mechanism is that geomagnetic jerks are caused by an instability in the form of a density heterogeneity in the topmost layer of the core, this then causes a downward flow, in turn inducing a step (discontinuity) in the core-mantle torque at the CMB (Bellanger et al., 2001). Although discovered over 30 years ago, the exact nature of geomagnetic jerks remains uncertain. This thesis focusses on wavelet analysis to try make further in-roads towards better understanding the origin of jerks.

1.4 Wavelet analysis

Signals carry an overwhelming amount of data from which relevant information can be difficult to extract (Mallat, 2009). "The Fourier Transform is probably the most widely applied signal processing tool. It reveals the frequency composition of a time series by transforming it from the time domain into the frequency domain" (Gao and Yan, 2011). In 1807, Joseph Fourier suggested that any signal, $x(t)$, can be made up of a weighted sum of sine and cosine functions:

$$x(t) = \int_{-\infty}^{\infty} X(f) e^{i2\pi f t} df \tag{1}$$

where $X(f)$ is the Fourier transform of $x(t)$, given as

$$X(f) = \int_{-\infty}^{\infty} x(t) e^{-i2\pi ft} dt \tag{2}$$

In practice, most signals that are analysed are discrete signals. The discrete Fourier Transform can be used to transform these signals - although this operation becomes computationally very expensive as the number of samples in the signal increases. This was dealt with by the indroduction of the Fast Fourier Transform (FFT) (Gao and Yan, 2011). Unfortunately, the Fourier Transform does not reveal how a signal's frequency changes with time (Mallat and Hwang, 1992).

In 1946, Dennis Gabor overcame this limitation by introducing a time-frequency analysis, short-time Fourier Transform (STFT), that uses a sliding window function, $y(t)$, to perform a "time-localized" Fourier Transform, as outlinedby Gao and Yan (2011):

$$STFT(\tau, f) = \int x(t) y(t-\tau) e^{-i2\pi ft} dt \tag{3}$$

Generally, higher resolutions provide a better transformation, but when using the short-time Fourier Transform, the time ($\triangle\tau$) and frequency ($\triangle f$) resolutions are constrained by Heisenberg's inequality as follows:

$$\triangle\tau . \triangle f \geq \frac{1}{4\pi} \tag{4}$$

Unfortunately, the choice of an appropriate window size is not known beforehand and as a result effective signal decomposition using the short-time Fourier Transform is not guaranteed Gao and Yan (2011). Although first referenced by Alfred Haar in 1909, and subsequent contributions by various others, it wasn't until Jean Morlet developed the technique for scaling and shifting an analysing function with acoustic signals while working for an oil company, was the wavelet transform born Gao and Yan (2011).

Wavelet analysis is a technique to extract information from signals at different positions and scales. This thesis outlines a similar formulation as in Alexandrescu et al., 1995, which seeks to utilise the continuous wavelet transform to study abrupt changes - singularities - in signals. Wavelets are well localized (around $t = 0$) oscillating functions with a vanishing integral. Wavelet analysis involves translating and dilating an analysing wavelet (or mother wavelet) $(\psi(t))$ to form a family of wavelets $(\psi_a(t))$ as follows:

$$\psi_a(t) = \frac{1}{a}\psi\left(\frac{t}{a}\right) \tag{5}$$

where a is the dilation parameter ($a > 0$).

We define the regularity (α) of a singularity as a singularity that results from discontinuity in the α^{th} derivative of the signal. The regularity of a singularity need not necessarily be an integer (for non-integer derivatives see Riewe, 1997). Regularity can be thought of as a measure of how singular an event is. Geomagnetic jerks are classically thought of as a jump in the second time derivative of a magnetic signal (i.e. $\alpha = 2$), but interestingly Alexandrescu et al. (1995, 1996) found that geomagnetic jerks are more singular than previously thought with a regularity of $\alpha = 1.5$, indicating a jump in 1.5^{th} derivative of the signal.

Since the observatory data we are analysing is a sum of the main field, containing singularities, and external fields, the signal, $f(t)$, is proposed to have the followings structure:

$$f(t) = \beta(t - t_0)^{\alpha} + h(t) + n(t) \tag{6}$$

where $h(t)$ represents harmonic components and $n(t)$ background noise in the signal.

The wavelet transform is defined as the convolution of the signal with the analysing wavelet. The convolution of signal with the analysing wavelet is the integral of the product of them, after the signal is translated and reversed:

$$W f(t,a) = f(t) * \psi_a(t) = \int_{-\infty}^{\infty} f(t)\psi_a(t-\tau)\, d\tau \tag{7}$$

The linearity of the wavelet transform allows:

$$W f(t,a) = \{[\beta(t - t_0)^{\alpha}](t,a) + h(t,a) + n(t,a)\} * \psi_a(t) \tag{8}$$

Let the analysing wavelet be written as the n^{th} derivative of a positive localized function, $\phi(t)$:

$$\psi(t) = \frac{1}{a} \frac{d^n}{d\left(\frac{t}{a}\right)^n} \phi\left(\frac{t}{a}\right) \tag{9}$$

.

Focussing on the term containing the singularity:

$$W f(t,a) = \beta(t - t_0)^{\alpha} * \frac{1}{a} \frac{d^n}{d\left(\frac{t}{a}\right)^n} \phi\left(\frac{t}{a}\right)$$

$$= \beta(t - t_0)^{\alpha} * \frac{1}{a} \frac{d^{\alpha+1}}{d\left(\frac{t}{a}\right)^{\alpha+1}} \frac{d^{-\alpha-1}}{d\left(\frac{t}{a}\right)^{-\alpha-1}} \frac{d^n}{d\left(\frac{t}{a}\right)^n} \phi\left(\frac{t}{a}\right)$$

$$= \beta \frac{d^{\alpha+1}}{dt^{\alpha+1}}(t-t_0)^{\alpha} * \frac{a^{\alpha+1}}{a} \frac{d^{n-\alpha-1}}{d\left(\frac{t}{a}\right)^{n-\alpha-1}} \phi\left(\frac{t}{a}\right)$$

$$= \beta a^{\alpha} \phi^{(n-\alpha-1)}(t,a) * \Gamma(\alpha+1)\delta(t-t_0)$$

$$= \beta a^{\alpha} \Gamma(\alpha+1) \phi^{(n-\alpha-1)}(t-t_0,a)$$

Assume that $\left|\phi^{(n-\alpha-1)}(t,a)\right|$ have N_l maxima so that:

$$\left\{\phi_{max,\,j};\, j=1,...,N_l\right\} \text{ occurs at times } \left\{t_{max,\,j};\, j=1,...,N_l\right\} \tag{10}$$

Therefore the wavelet transform $|W[\beta(t-t_0)^{\alpha}](t,a)|$ also has N_l maxima at times $\left\{at_{max,\,j}+t_0;\, j=1,...,N_l\right\}$

The maxima of the wavelet transform arrange themselves into N_l lines of maxima for $\left\{t = at_{max,\,j}+t_0;\, j=1,...,N_l\right\}$ which converge to t_0 (the time of the singularity) as $a \to 0$.

If we then define a ridge function, r_j, as the absolute value of the wavelet transform along a given line of maxima:

$$r_j(a) = |W[\beta(t-t_0)^{\alpha}](t,a)|\,(at_{max,\,j}+t_0,\,a) = \Gamma(\alpha+1)\,|\beta|\,a^{\alpha}\phi_{max,\,j} \tag{11}$$

$$\therefore \ln r_j(a) = \alpha \ln a + \ln\Gamma(\alpha+1) + \ln|\beta| + \ln\phi_{max,\,j} \tag{12}$$

Equation (12) shows that when a given ridge function is plotted in a log-log diagram (logarithm of the absolute value of a wavelet transform along a given line of maxima against the logarithm of the dilation parameter), it forms a straight line with slope α.

The analysing wavelet used in this study is the 3^{rd} derivative of the Gaussian and is given in equation (13). This wavelet was chosen as it had sufficient vanishing moments to detect singularities of the expected regularity and adequate time localisation (Alexandrescu et al., 1995).

$$\psi(t) = \frac{d^3}{dt^3} e^{-\frac{t^2}{2}} = t(3-t^2)e^{-\frac{t^2}{2}} \tag{13}$$

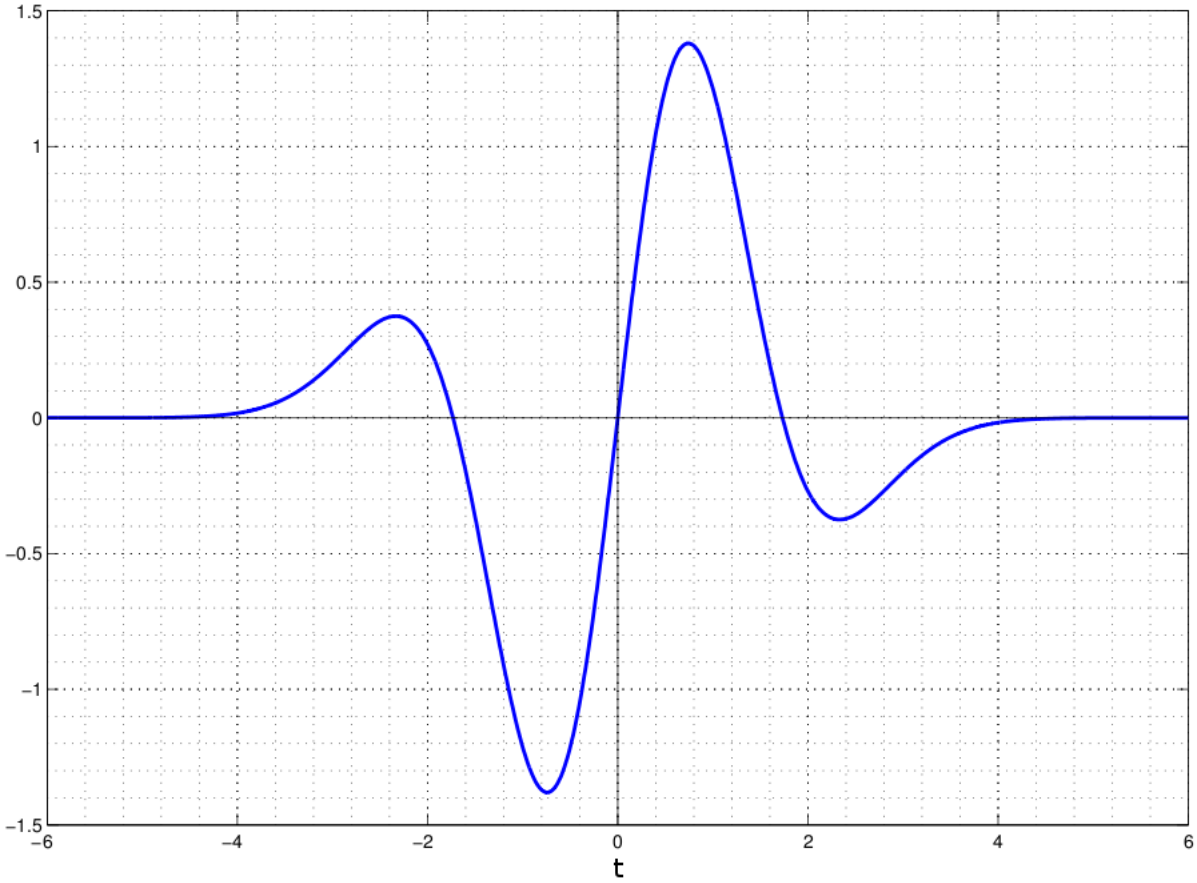

Figure 9: Plot of the analysing wavelet, 3^{rd} derivative of the Gaussian, defined in equation (13), $t \in [-6, 6]$.

1.5 Objectives

Exploring geomagnetic jerks is important to help the understanding of the dynamical processes in the core driving these phenomena. The foremost objective of this study then is to develop a wavelet tool and apply this tool to recently reprocessed extended time series to recognize and analyse recent geomagnetic jerks. Wavelet analysis is first applied to synthetic signals for testing purposes. The wavelet tool then analyses magnetic observatory data to detect and characterise geomagnetic jerks (e.g. Chapter 2). The dates of geomagnetic jerks detected using this wavelet tool are tested against results obtained by Alexandrescu et al. (1995). Furthermore, this study aims to detect geomagnetic jerks that are known to have occurred just before or after the Alexandrescu et al. (1995) study was completed and compares the dates of these geomagnetic jerks to those of other studies (e.g. Mandea et al., 2000; Olsen and Mandea, 2007; Chulliat et al., 2010).

Thereafter, this study aims to further explore the characteristics of geomagnetic jerks: the spatio-temporal behaviour and regularity of geomagnetic jerks. The spatio-temporal behaviour of geomagnetic jerks detected using wavelet analysis is examined and compared to behaviours observed in other studies (Alexandrescu et al., 1996; Olsen and Mandea, 2007) mentioned in subsection 1.3.

The recovered regularities of geomagnetic jerks detected using wavelet analysis are also compared to those obtained in Alexandrescu et al. (1995, 1996), who identified regularities of geomagnetic jerks to be closer to 1.5 than the expected 2.

Finally, the nature of geomagnetic jerks is examined. As outlined in subsection 1.3.2, the origin of geomagnetic jerks is not clearly understood. This study aims to also investigate whether the nature of geomagnetic jerks are the result of:

- An instability starting at the time of the jerk
- Some continuous oscillations
- A process ending at the time of the jerk.

This could help identify the mechanism driving geomagnetic jerks put forward by various studies (e.g. Bloxham et al. 2002; Bellanger et al. 2001; Le Huy et al. 1998).

1.6 Layout

Chapter 2 outlines the development and testing of the wavelet tool used in this analysis. An outline of the analysis technique is provided in subsection 2.1.1 and applied to a synthetic signal. This outline is extended by adding noise and harmonic components to the synthetic signal. Subsection 2.1.2 introduces regularity by applying the wavelet tool to a synthetic signal of singularities of various regularity. The wavelet tool is detailed in subsection 2.3 and then applied in subsection 2.4 to monthly mean magnetic data from Chambon-la-Forêt observatory used in the study Alexandrescu et al. (1995). The results are then compared to those found by the study. Finally, the data used in this study is then highlighted (subsection 3).

In Chapter 4 the results obtained using the wavelet tool applied to monthly mean data from 45 selected observatories around the world are shown and explored. Subsection 4.1 provides an example wavelet transform plot and log-log diagram from Hartland Magnetic Observatory (the remaining figures are given in the appendices). Tables and figures summarising the geomagnetic jerks detected using the wavelet analysis are provided in subsection 4.2. The spatio-temporal behaviour of the geomagnetic jerks detected is explored in subsection 4.3. Finally, in subsection 4.4,

the nature of some of the geomagnetic jerks found is explored by comparing their signatures to synthetic examples. Discussions and final concluding remarks of the results are given in Chapter 5.

Chapter 2

Method: developing a Matlab wavelet tool

A wavelet tool was programmed in Matlab to perform a wavelet transformation of a signal, display the transformed signal appropriately and perform further calculations on the transformed signal. The following chapter outlines the development of this tool, and how it was applied to synthetic signals and magnetic signals in order to troubleshoot the tool and make sense of its results. The Matlab code used to execute the continuous wavelet transform is provided in Appendix A.

Signals analysed in this study are sampled at a 1 month interval - the unit of time adapted for this study. The dilation parameter, a, is chosen to range from 2^1 to 2^7 and is exponentially sampled at 20 points evenly distributed per power of 2. The maximum value of a used is largely determined by the length of the signal used in the analysis, because at higher order dilations the convolutional edge effects increase to a point such that they eclipse the relevant contributions from the signal. It is important to note that when applying wavelet analysis, convolutional edge effects must be considered as they prevent detection of singular events close to the beginning or the end of a time series.

The function file 'transform.m', provided in appendix A.1, is the core function of the wavelet tool. It performs the convolution of the input signal with the analysing wavelet dilated by each value of the dilation parameter, a, returning a matrix of wavelet coefficients. This function calls the functions 'gaussian3.m' (appendix A.2) and 'convolution.m' (appendix A.3) to return the analysing wavelet dilated by the inputed dilation parameter and perform the convolution, respectively.

2.1 Tests with synthetic data

2.1.1 Continuous wavelet transform and lines of maxima

For initial testing, a simple synthetic signal, $f(t)$, containing a jerk-like singularity starting at time $t_0 = 500$ (with a regularity of 1.5) was produced and transformed using the wavelet tool. To emulate the singularity of a real geomagnetic jerk, the singularity was chosen to have a regularity of 1.5 based on the findings of Alexandrescu et al. (1995). The synthetic signal used is defined in equation (14) and displayed in figure 10 below.

$$f(t) = \begin{cases} 1 & \text{for } t < t_0 \\ 1 + 0.001(t - t_0)^{1.5} & \text{for } t \geq t_0 \end{cases} \tag{14}$$

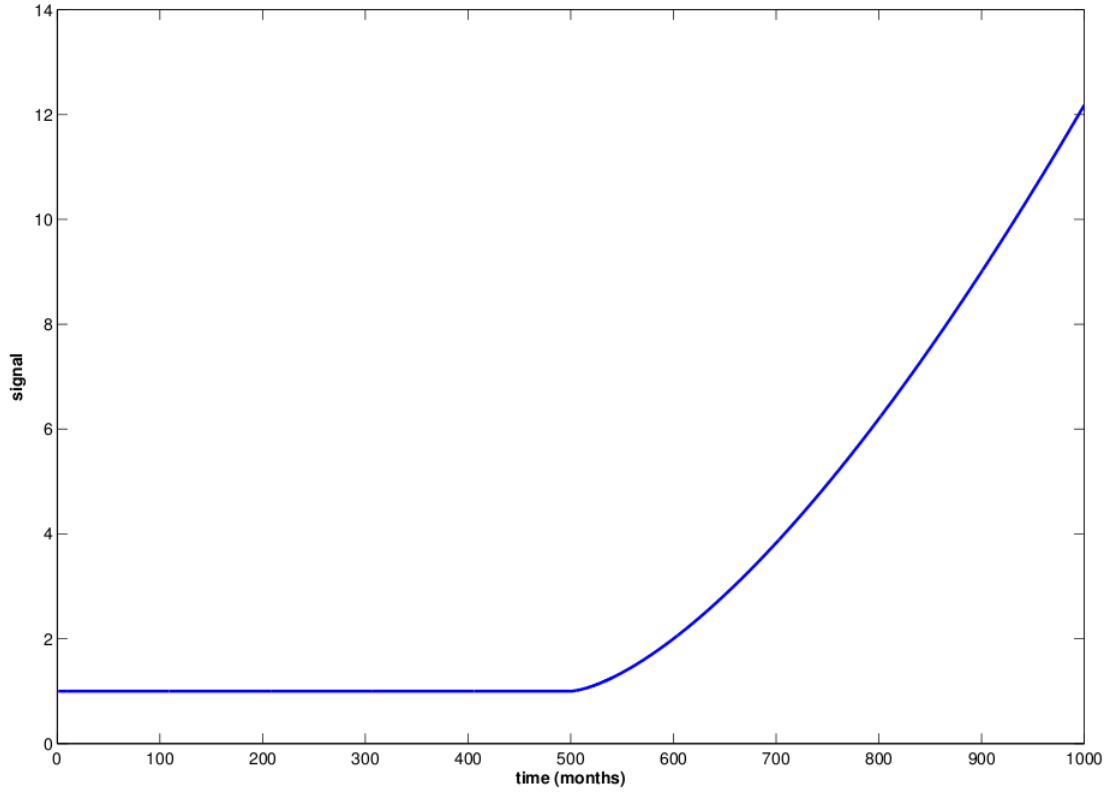

Figure 10: Plot of synthetic signal comprising of a jerk-like singularity (with a regularity of 1.5) at $t_0 = 500$ defined in equation (14). $t \in [0, 1000]$.

The signal, defined in equation (14) and shown in figure 10, above, was then transformed using the wavelet tool. An example of a contour plot of the absolute values of this wavelet transformation, or wavelet coefficients $|W f(t,a)|$,

is shown in figure 11. The logarithm (of base 2) of the dilation axis is taken for an evenly graduated axis - hence the choice of calibration of a.

The contour line graduations of this contour plot vary so as to allow good resolution of wavelet coefficients of small values (in the lower order dilations) and also good resolution of the larger values (in the higher order dilations). The contour lines in figure 11 have the following graduations: $[0.001; 0.002; ...; 0.01; 0.02; ...; 0.1; 0.2; ...; 1]$. The colour scale of the contour plot, as wavelet coefficients increase, range from dark blue, through various shades of blue, cyan, green, yellow and red, and ends with dark red. Wavelet coefficient values falling above the last contour level are coloured black.

The contribution from convolutional edge effects is often coloured in black because of the large values produced by this effect. The convolutional edge effects are clearly seen in figure 11, as they form a typical arch-like shape framing the contour plot. As a increases exponentially, so too does the effect of convolving a wavelet, dilated by a, with the beginning or end of the signal. The beginning and end of a time series can be thought of as singular events themselves - a discontinuity in the data.

As expected from the theory outlined in subsection 1.4, the wavelet transform of a signal containing a singularity arranges into lines of maxima which converge to the time of the singularity (t_0) as a decreases (or $a \to 0$). This process provides a clear method to determine when a singularity, or geomagnetic jerk, occurred; or in other words, determine t_0. These lines of maxima are calculated from the modulus of the wavelet transform using the Matlab function file, 'lom.m' provided in appendix A.4. These lines of maxima are then plotted on top of the contour plot, in white in figure 11, and numbered chronologically. It is important to note that the lines of maxima associated with convolutional edge effects are not relevant in the analysis as they represent the "singular event" of the edge of the time series.

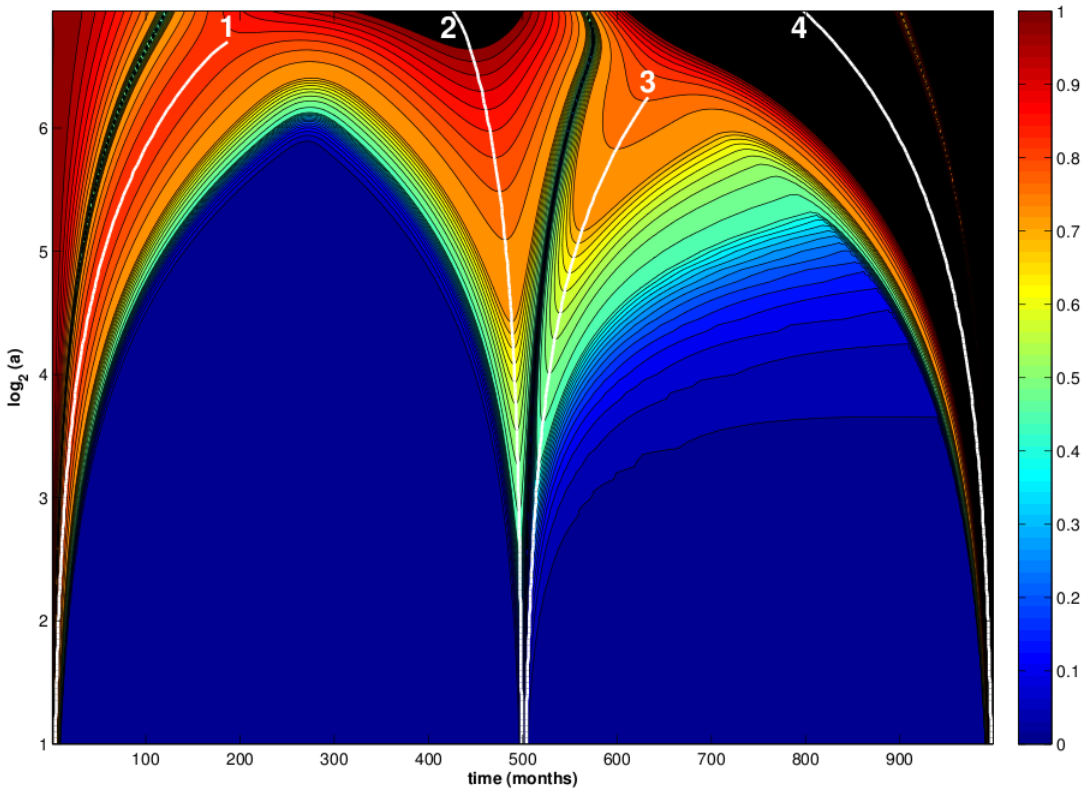

Figure 11: Contour plot of the modulus of the wavelet transform of the synthetic signal defined in equation (14) and shown in figure 10. The lines of maxima of the modulus of the wavelet transform are then plotted in white and numbered chronologically. Wavelet coefficients greater than 1, corresponding to edge effects, are colored black. $t \in [0, 1000]$.

Adding synthetic external contributions

In order to emulate geomagnetic data, the above analysis was repeated after adding synthetic harmonic components, $h(t)$, and noise components, $n(t)$, to the synthetic signal $f(t)$ from equation (14). The modified synthetic signal, $g(t)$, is given in equation (15) below.

$$g(t) = f(t) + h(t) + n(t) \tag{15}$$

The harmonic component, $h(t)$, was chosen to try and emulate harmonic signals that might be present in geomagnetic data. $h(t)$ is made up of the superposition of sinusoidal functions of varying period. The periods selected were $T = [11, 5.5, 3.7, 1]$ years so as to be related to the solar magnetic activity cycle and amplitudes of $A = [0.01, 0.005, 0.005, 0.005]$ of comparable magnitude to external signals found in geomagnetic data (Alexandrescu

et al., 1995).

$$h(t) = \sum_{i=1}^{4} A_i \sin\left(\frac{2\pi t}{12T_i}\right) \tag{16}$$

The noise component was chosen to be a Gaussian distribution with mean, $\mu = 0$, and variance, $\sigma = 10^{-4}$, of the order of noise found in magnetic data (Alexandrescu et al., 1995).

$$n(t) = \frac{1}{\sigma\sqrt{2\pi}} e^{-\frac{1}{2}\left(\frac{t-\mu}{\sigma}\right)^2} \tag{17}$$

The synthetic signal, $g(t)$, defined in equation (15) is shown in figure 12 below. Note the shaky line compared to figure 10.

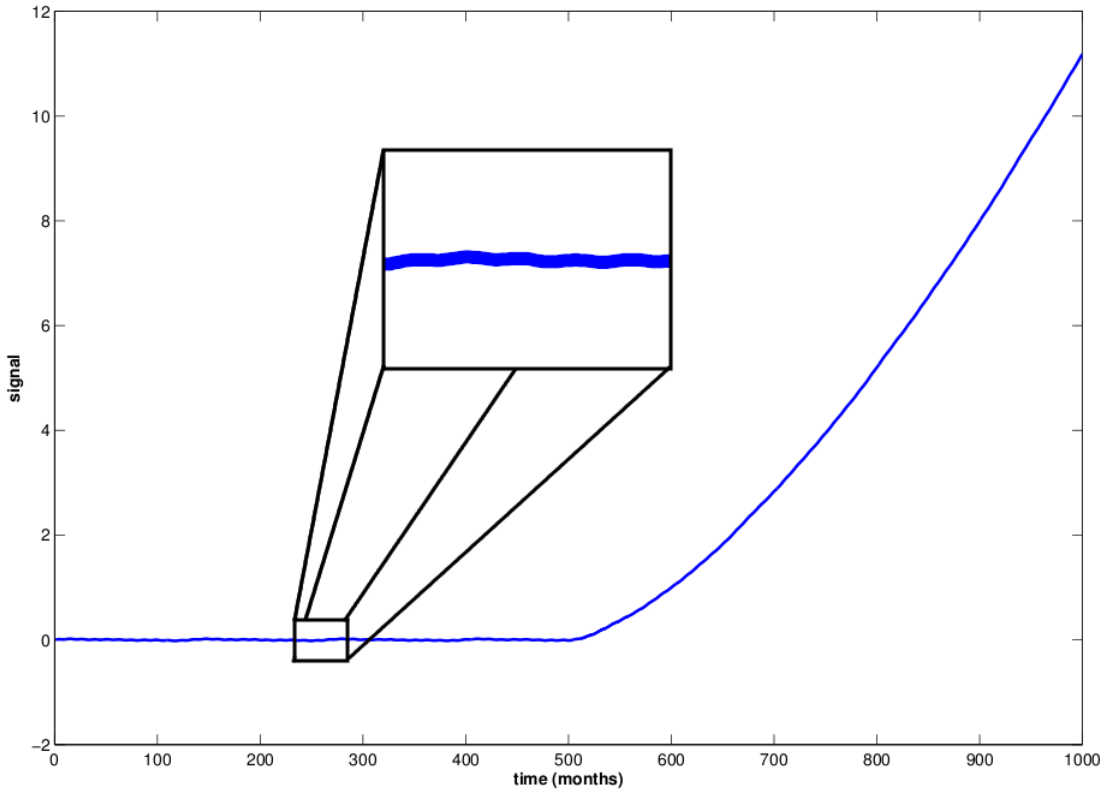

Figure 12: Plot of synthetic signal comprising of a jerk-like singularity (with a regularity of 1.5) at $t_0 = 500$ with noise and harmonic components added as defined in equation (15). An expansion of a part of the plot is included to demonstrate the shakiness. $t \in [0, 1000]$.

Similarly to above, the signal, defined in equation (15) and shown in figure 12 above, was then transformed using

the wavelet tool. A contour plot of the absolute values of this wavelet transformation is shown in figure 13 below. All the lines of maxima are calculated and plotted on top of the contour plot in white in figure 13.

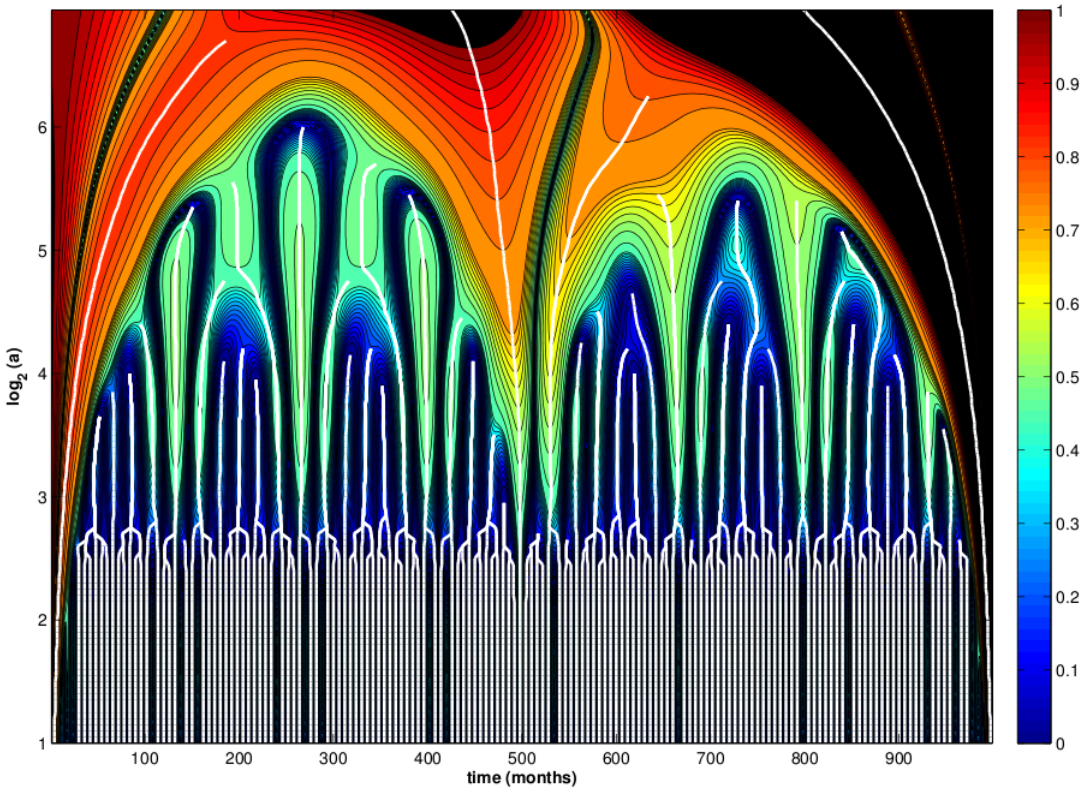

Figure 13: Contour plot of the modulus of the wavelet transform of the synthetic signal defined in equation (15) and shown in figure 12. All the lines of maxima of the modulus of the wavelet transform are plotted in white. $t \in [0, 1000]$.

Again, a contour plot of the absolute values of this wavelet transformation is shown in figure 14, but only the longest lines of maxima are plotted and numbered chronologically. Lines of maxima corresponding to the lower order dilations ($\log_2(a) < 3$) have been omitted so as not to clutter the figure. These lines of maxima are associated with the added noise component and form a clear band across the bottom of the figure.

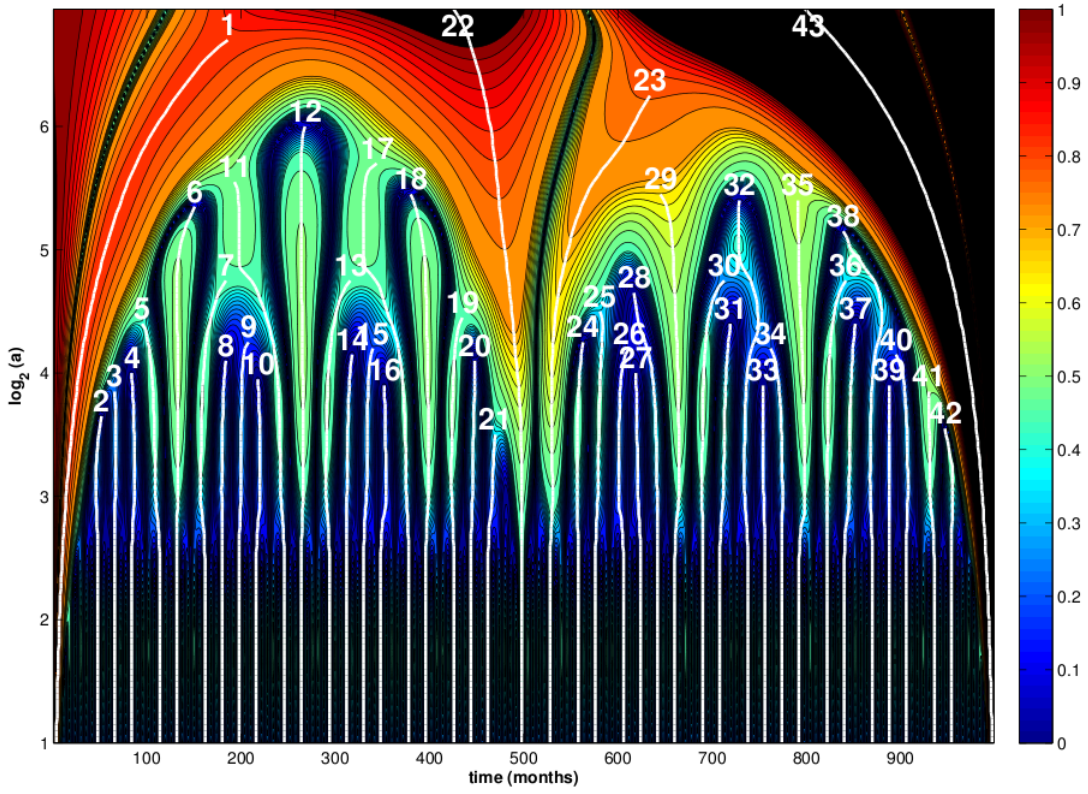

Figure 14: Contour plot of the modulus of the wavelet transform of the synthetic signal defined in equation (15) and shown in figure 12. The lines of maxima of the modulus of the wavelet transform that extend beyond the lower order dilations ($\log_2(a) > 3$) are plotted in white and numbered chronologically. $t \in [0, 1000]$.

Figure 14 shows that added noise and harmonic components introduce further lines of maxima, but that lines of maxima associated with the jerk-like singularity ($j = 22$; $j = 23$) remain clear. Furthermore, ignoring the lines of maxima associated with convolutional edge effects ($j = 1$; $j = 43$), the lines of maxima associated with the singularity can be easily distinguished from those associated with the noise and harmonic components as they extend into the higher order dilations ($\log_2(a) > 6$). Note how the lines of maxima associated with the harmonic components bifurcate as they head into the lower order dilations forming a fork-shape and how the lines of maxima from the noise components form a band in the lower dilations. These are important observations that will later be used to help characterise a line of maxima found when analysing real magnetic data as being associated with geomagnetic jerks or not.

It is also important to note in figure 14, that the introduction of noise and harmonic components has interfered with the lines of maxima associated with the singularity. This is clear if one compares the lines of maxima associated with the singularity in figure 11 with the ones in figure 14. The introduction of noise components into this signal perturbs the right-hand lines of maxima associated with the singularity, but leaves the other "main" line of maxima relatively

unchanged.

In figure 11, as dilation decreases ($a \to 1$), the two lines ($j = 2$; $j = 3$) converge to $t = 499$ and $t = 504$ respectively (average of $t = 501.5$). This provides a reasonable estimate of when the singularity occurred: $t_0 = 500$. Comparatively, in figure 14, lines of maxima associated with the singularity ($j = 22$; $j = 23$), converge to $t = 498$ and $t = 528$ respectively (average of $t = 513$) as dilation decreases. The latter of which ($j = 23$) would suggest that the singularity occurred a staggering 28 months later than it really did. This highlights the effect that addition of noise and harmonic components to a signal might have on accurately determining when a singularity occurred. This is further discussed in the next subsection where experiments on a synthetic signal containing singularities of varying regularity are explored.

2.1.2 Ridge functions and recovering regularity

A further step in the analysis of geomagnetic jerks involves recovering the regularity of singularities detected in a signal. As outlined in section 1.4, equation (12) shows that if one traverses a line of maxima associated with a singularity and plots the logarithm of the absolute value of wavelet transform against the logarithm of the dilation parameter (so-called log-log plots), the slope of this line equals the regularity (α) of the singularity.

To test this, a new synthetic signal, identical to the signal used by Alexandrescu et al. (1995), containing singularities of varying regularity, was analysed using the wavelet analysis tool. The resulting lines of maxima associated with the singularities were traversed. The log-log plots of these traversals are displayed and approximate regularities calculated using function file 'loglog_plot_all.m', provided in appendix A.5.

The synthetic signal used, defined piecewise in equation 18 and shown in figure 15, contains the following singularities with known theoretical regularity: a Dirac function (at $t_1 = 255$ with $\alpha = -1$), a Heaviside step function (at $t_2 = 511$ with $\alpha = 0$), a ramp function (at $t_3 = 767$ with $\alpha = 1$), a singularity of regularity $\alpha = 1.5$ (at $t_4 = 1023$) and a singularity at time $t_5 = 1279$ of regularity $\alpha = 2$ (Alexandrescu et al., 1995).

$$s(t) = \begin{cases} 0.2 & \text{for} t = t_1 \\ 0.1 & \text{for} t \geq t_2 \\ 0.01(t - t_3) & \text{for} t \geq t_3 \\ -0.001(t - t_4)^{1.5} & \text{for} t \geq t_4 \\ 0.0001(t - t_5)^2 & \text{for} t \geq t_5 \end{cases} \tag{18}$$

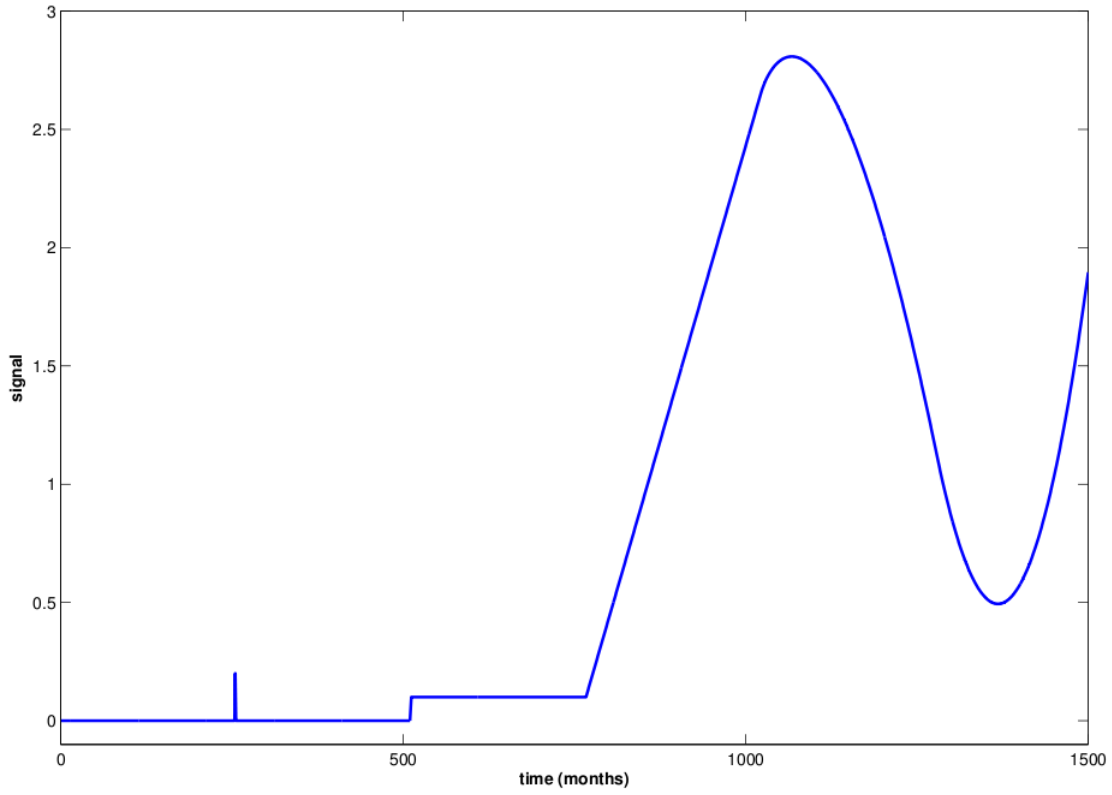

Figure 15: Plot of synthetic signal, $s(t)$, defined in equation (18), made up of various singularities of differing regularity - a Dirac function (at $t_1 = 255$ with $\alpha = -1$), a Heaviside step function (at $t_2 = 511$ with $\alpha = 0$), a ramp function (at $t_3 = 767$ with $\alpha = 1$), a singularity of regularity $\alpha = 1.5$ (at $t_4 = 1023$) and a singularity at time $t_5 = 1279$ of regularity $\alpha = 2$. $t \in [0, 1500]$.

The contour plot of wavelet transform of the signal, $s(t)$, defined piecewise in equation 18 and shown in figure 15, is shown in figure 16 below. Again, the lines of maxima are calculated and superimposed in white on the contour plot in figure 15 and numbered chronologically. Note that the line of maxima numbered 13 in figure 16 below is caused by convolutional edge effects and can be ignored.

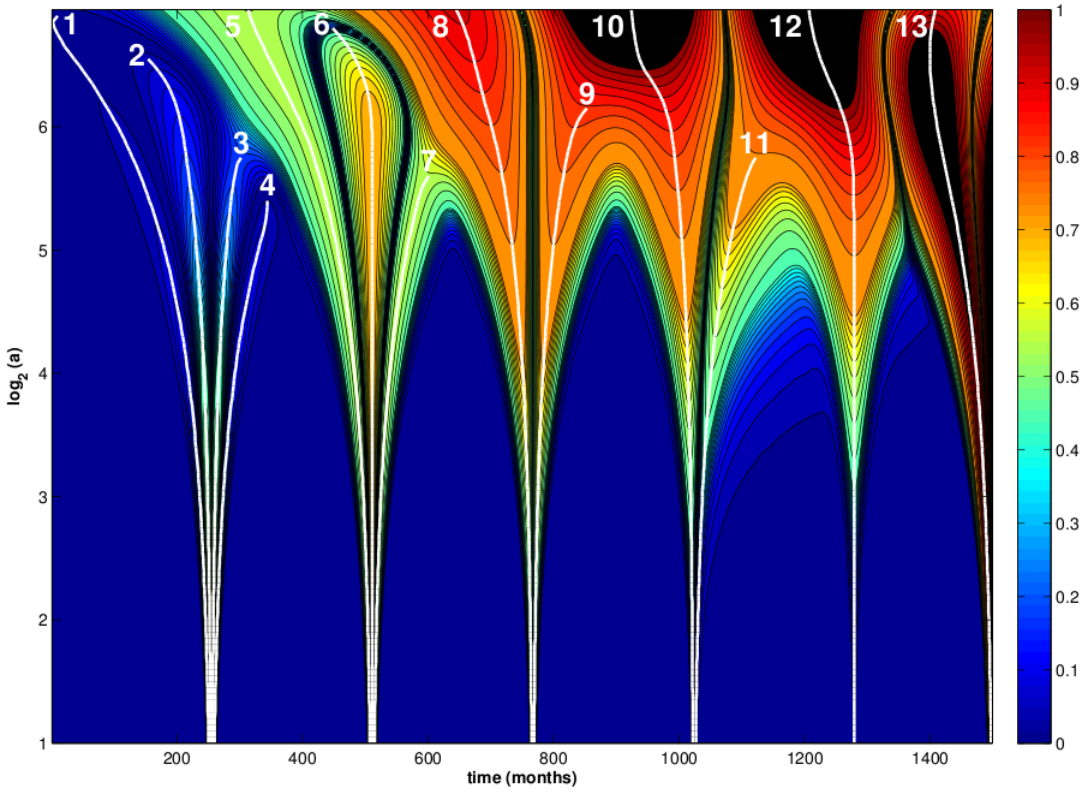

Figure 16: Contour plot of the modulus of the wavelet transform of the synthetic signal defined in equation (18) and shown in figure 15. The lines of maxima of the modulus of the wavelet transform are plotted in white and numbered chronologically. $t \in [0, 1500]$.

What is clear from figure 16 is that the number of lines of maxima (N_j) associated with the different singularities can differ. Alexandrescu et al. (1995) showed that four lines of maxima are expected for a Dirac function, three for a Heaviside step function, two for a ramp function and one for a jerk. They further generalized that the number of lines of maxima associated with singularities of non-integer regularity is the same as that of singularities with non-integer regularity rounded down to the nearest integer. Hence, the singularity of regularity, $\alpha = 1.5$, should have two lines of maxima, the same as the ramp function with regularity, $\alpha = 1$. The expected number of lines of maxima associated with each singularity are corroborated in figure 16.

Furthermore, the associated lines of maxima are symmetrical for singularities of integer regularity and non-symmetrical for singularities of non-integer regularity. This can be seen in figure 16 for dilations $\log_2(a) < 5$, but as one heads into the higher order dilations, the dilated wavelet can overlap two neighbouring singularities, causing interference in the wavelet transform. It is interesting to compare the non-symmetrical shape of the two lines of maxima (lines 10 and 11) associated with the the singularity of regularity 1.5 to the lines of maxima of the ramp function (lines 8 and 9).

Although similar in shape, where the right-hand arm of the former singularity has weakened, it breaks the symmetrical pattern of the latter pair of lines of maxima.

The next step in the analysis is to recover the regularities of the singularities from the wavelet transform. For each of the lines of maxima, the logarithm of the absolute value of wavelet transform is plotted against the logarithm of the dilation parameter along the traversal of that line of maxima. As expected from the theory, the log-log plots corresponding to singularities form straight lines, the slope of which equals the regularity (α) of the singularity. The log-log plots of the lines of maxima shown in figure 16 are given in figure 17, respectively. The approximate slope of each of the log-log plots are labelled alongside.

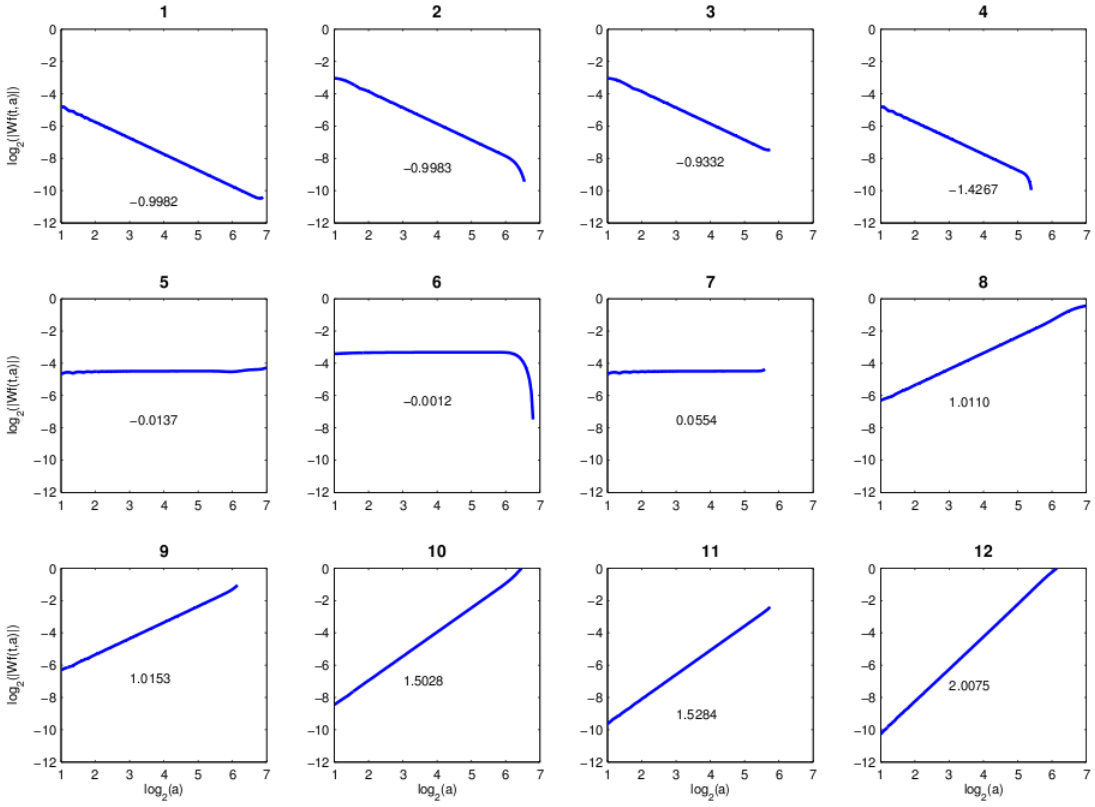

Figure 17: Log-log plot of each of the lines of maxima given and numbered in figure 16. For each of the lines of maxima, the logarithm of the absolute value of wavelet transform is plotted against the logarithm of the dilation parameter along the traversal of that line of maxima. The recovered regularities (the slope of the straight lines) are labelled alongside. $a \in [2^0, 2^7]$.

In figure 17, the recovered regularities can be compared to the known regularities of each of the singularities: lines of maxima numbered 1-4 give a regularity of $\alpha \approx -1$ corresponding to the Dirac function ($\alpha = -1$); lines of

maxima numbered 5-7 have regularities of $\alpha \approx 0$ corresponding to the Heaviside step function ($\alpha = 0$); lines of maxima numbered 8-9 have regularities of $\alpha \approx 1$ corresponding to the ramp function ($\alpha = 1$); lines of maxima numbered 10-11 have regularities of $\alpha \approx 1.5$, closely approximating the singularity of regularity of $\alpha = 1.5$; and lastly, line of maxima 12 approximates a regularity of $\alpha \approx 2$, corresponding to the singularity with $\alpha = 2$. The recovered regularities show an excellent approximation of the known regularities.

Adding synthetic external contributions

In order to explore the effect external components present in geomagnetic data might have on the analysis process of recovering regularities, the above numerical experiment is repeated, as before, after adding harmonic components, $h(t)$, and noise components, $n(t)$, to the synthetic signal $s(t)$ from equation (18). This sum is given in equation (19) and plotted in figure 18 below.

$$m(t) = s(t) + h(t) + n(t) \tag{19}$$

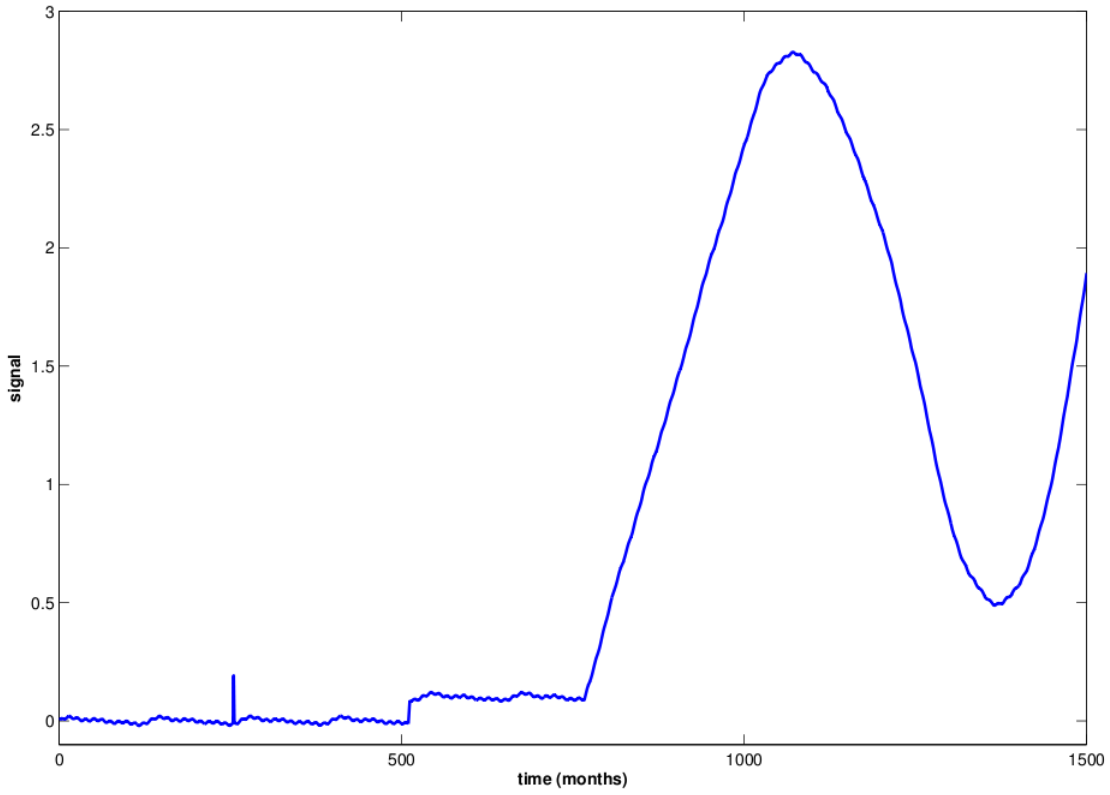

Figure 18: Plot of signal, $m(t)$, defined in equation (19), of the synthetic, $s(t)$ (synthetic signal containing singularities of varying regularity) with added harmonic components, $h(t)$, and noise components, $n(t)$. $t \in [0, 1500]$.

The contour plot of wavelet transform of the signal, $m(t)$, defined in equation (19) and shown in figure 18, is shown in figure below with the longest ($log_2(a) > 5$) lines of maxima superimposed and numbered in white on the contour plot.

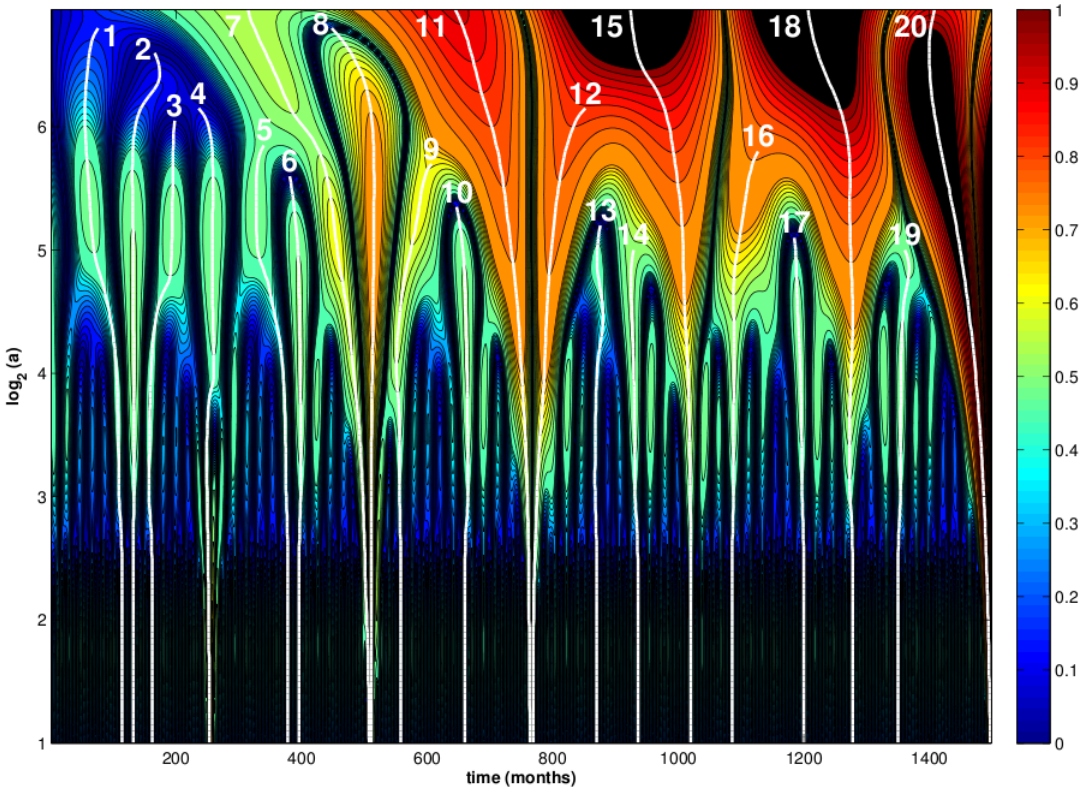

Figure 19: Contour plot of the modulus of the wavelet transform of the synthetic signal defined in equation (19) and shown in figure 18. The longest ($log_2(a) > 5$) lines of maxima of the modulus of the wavelet transform are plotted in white and numbered chronologically. $t \in [0, 1500]$.

It is clear from figure 19 that with the addition of external components, the lines of maxima associated with the Dirac function ($\alpha = -1$) have been interfered with. This is to be expected as singularities with $\alpha < -0.5$ are dominated by noise components in the higher order dilations; only in the lower order dilations is the deterministic signal of the Dirac function evident (Alexandrescu et al., 1995). This means that it will no longer be possible to accurately recover the regularity of the Dirac function from the associated log-log plots. Conversely, for singularities of regularity greater than -0.5, the deterministic signal dominates in the higher order dilations, but noise components disturb the wavelet transform in the lower dilations.

Again note the perturbation of one of the lines of maxima corresponding to the singularity with regularity of 1.5. As mentioned before, the lines of maxima associated with a singularity of this regularity (non-integer) have a non-symmetric shape. The addition of external components have further weakened the right-hand line of maxima. This is important to note, as using this weakened line of maxima to try determine when its associated singularity occurred, would not produce accurate results.

The log-log plots of the lines of maxima shown in figure 19 are given in figure 20 and numbered correspondingly. The approximate slope of each of the log-log plots are labelled alongside.

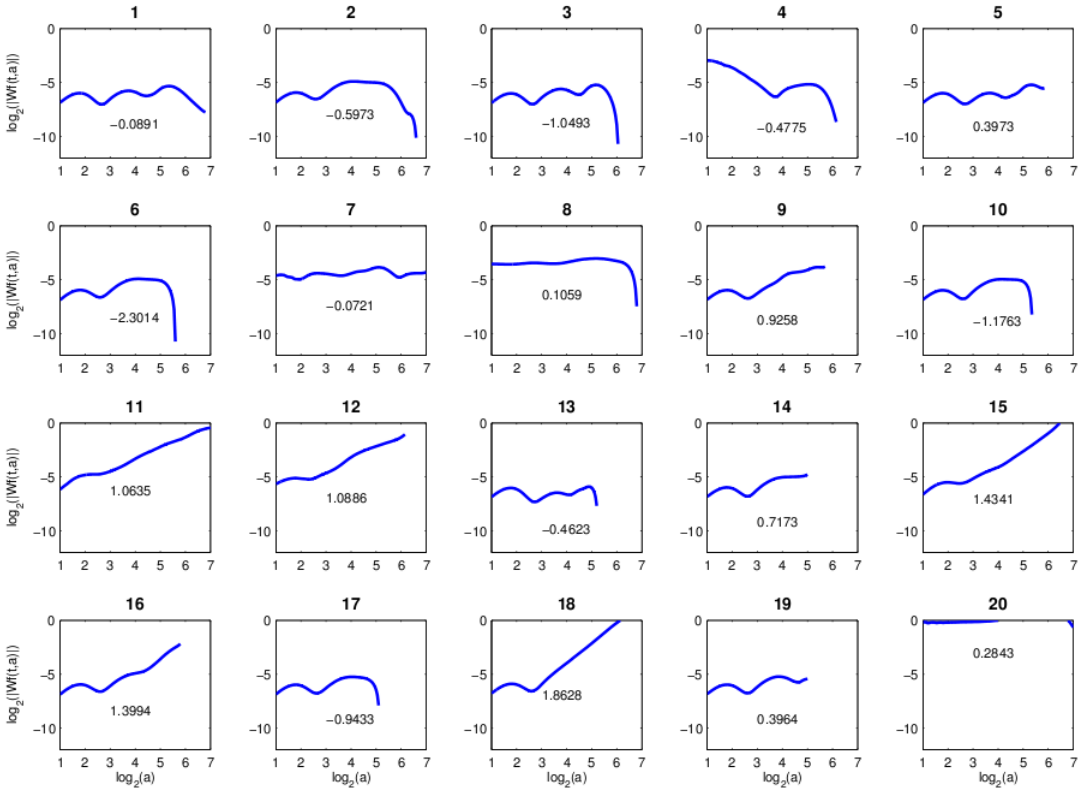

Figure 20: Log-log plot of each of the lines of maxima given and numbered in figure 19. For each of the lines of maxima, the logarithm of the absolute value of wavelet transform is plotted against the logarithm of the dilation parameter along the traversal of that line of maxima. The recovered regularities (the slope of the straight lines) are labelled alongside. $a \in [2^0, 2^7]$.

Figure 20 shows that ridge functions corresponding to the added external components (lines numbered 1-6, 10, 13, 14, 17 and 19) display a "wobbly" shape and usually drop off rapidly in the higher order dilations ($a < 2^5$). This is an important observation as it will form the basis for characterising ridge functions relating to external components.

It is crucial to be able to identify and exclude ridge functions found in geomagnetic data that do not correspond to geomagnetic jerks.

As expected, the ridge functions in figure 20 related to the Dirac function can not be clearly identified as they are dominated by noise components. The calculated slopes are inaccurate approximations of the regularity of the Dirac singularity present in the signal.

Looking at the ridge functions of the other singularities, the linear trends of the underlying singularities are still prominent, but they are now disturbed in the lower dilations by noise ($a < 2^3$). As a result, in order to recover the regularities of the singularities accurately, only the slope of the linear portion of the ridge function is used.

It is also important to note how the line of maxima numbered 9 (Figure 19) corresponding to the Heaviside step function with $\alpha = 0$, suffers from interference with its neighbouring singularity, the ramp function with $\alpha = 1$, and as a result its ridge function (Figure 20) recovers a regularity closer to 1 than 0. This interference is further discussed in Chapter 4.

2.2 Conclusion: characterization of singularities

The above analysis of synthetic signals has helped build a guide for how lines of maxima found in geomagnetic data can be interpreted as corresponding to a singularity (geomagnetic jerk) or caused by external components present in the signal. By looking at the corresponding ridge functions, lines of maxima related to singularities display strong linear trends and also usually extend into the higher dilations. Whereas ridge functions caused by external components present in the signal, display a "wobbly" shape and usually decrease rapidly for dilations $a < 2^5$.

2.3 Description of Matlab tool adapted to analyse geomagnetic data

The Matlab tool used to perform the synthetic experiments above was then adapted for analysis of geomagnetic data and the details of the functions that make up the tool are given here. The Matlab code 'runall.m', given in appendix A.6, is the main algorithm used to perform wavelet analysis, consolidate the results and output related figures on a chosen list of observatory datasets. This program repeats various functions on each observatory dataset interpreted; these are outlined below in the order they would run.

2.3.1 Interpreting observatory data files

The function 'read_observatory.m', given in appendix A.7, reads observatory data files (of a particular format) and interprets basic information about the magnetic observatory from the header (e.g. name, short code, longitude, latitude,

elevation) and then extracts the geomagnetic data entries to be analysed. This algorithm is specifically tailored to the format of the magnetic data used in this study.

2.3.2 Cleaning the data

For various reasons, gaps are sometimes present in magnetic observatory data (e.g. magnetometer failure, equipment maintenance, unreliable data). This poses a serious problem for wavelet analysis as any discontinuities in the time series will eclipse any singularities that might be present in signal. For gaps in the middle of a time series, function 'clean.m', given in appendix A.8, performs linear interpolation to fill the gaps. Data gaps at the beginning and end of a time series are simply deleted and the time series shortened.

2.3.3 The wavelet transform

The continuous wavelet transform is then performed on the processed data as outlined during the synthetic experiments. The function 'transform.m' performs the wavelet transform by performing the convolution (using 'convolution.m') of the inputted signal with the analysing wavelet dilated by each value of the dilation parameter, a, (calling 'gaussian3.m') and returns a matrix of wavelet coefficients.

2.3.4 Displaying the wavelet transform

The wavelet coefficients are then plotted on a contour plot by 'contour_plot.m'. Any lines of maxima present in the wavelet transform are determined by 'lom.m' and are superimposed on the contour plot in white by 'lom_plot.m'. Only the lines of maxima that extend beyond the dilation $a < 2^5$ are displayed.

2.3.5 Plotting ridge functions

As mentioned in the synthetic experiments, each line of maxima output by 'lom.m' is traversed and its ridge function determined. 'log_log_all.m' plots the ridge functions of all the lines of maxima. The slope of the ridge functions for $a < 2^{2.5}$ are calculated and labelled.

2.3.6 Identifying jerks

The lines of maxima identified by 'lom.m' are then examined by the function 'select_jerks.m' to determine which of the lines of maxima might correspond to geomagnetic jerks. Using the behaviour highlighted by the synthetic tests, lines of maxima that extend into the higher order dilations, have corresponding ridge functions with clear linear trends (ridge of constant average gradient and length at least 20 samples), are earmarked as possible geomagnetic jerks. Furthermore,

only linear sections with a slope of greater than 0.8 are chosen so as to eliminate singular events of smaller regularity. The selected lines of maxima are numbered in the contour plots.

All the ridge functions of these selected lines of maxima are then plotted by 'log_log_plot.m' and the clear linear portions of the ridge functions are then identified on the ridge functions and plotted in red. These linear portions are then used to more accurately recover the regularity of the singularity that could otherwise have been misrepresented because of the interference of the ridge function, especially in the lower order dilations, by external field components present in the signal.

2.3.7 Dating of a jerk

Finally, as shown in the synthetic tests, accurately determining when a singularity occurred must be done with care because the interference in the lower order dilations can skew this result. Therefore, for each of the lines of maxima selected as corresponding to possible geomagnetic jerks, 'dating_jerks.m' determines the approximate time at which the geomagnetic jerk occurred, t_0, taken along the line of maxima at a dilation of $a = 2^{2.5}$. It is important at this stage to note that the time, t_0, at which a singularity occurs, represents the time at which it is detected at the surface of the Earth by magnetic observatories. These jerks may originate in the core of the Earth many months before but the signal has taken time to diffuse through the mantle to then be detected.

All the figures plotted in the analysis for each of the observatories are stored as images in pdf files and the results from the wavelet analysis are stored for further investigation and manipulation.

2.4 Validating the wavelet tool

In order to validate that the wavelet tool developed was correctly analysing geomagnetic data, the original time series of magnetic data from the Chambon-la-Forêt Magnetic Observatory in France used by Alexandrescu et al. (1995) was analysed as a test. The results produced by the wavelet tool are then compared with their previous results. The Y-component monthly mean values are plotted in figure 21. The results produced by 'runall.m' on this time series are given: a contour plot wavelet transform with the longest lines of maxima superimposed (Figure 22); the log-log plot of the related ridge functions of the lines of maxima numbered in the contour plot and approximate slopes labelled (Figure 23); a contour plot wavelet transform with only the lines of maxima selected as corresponding to possible geomagnetic jerks numbered (Figure 24); the ridge functions of the selected lines of maxima plotted in a log-log diagram with the linear portions highlighted in red (Figure 25).

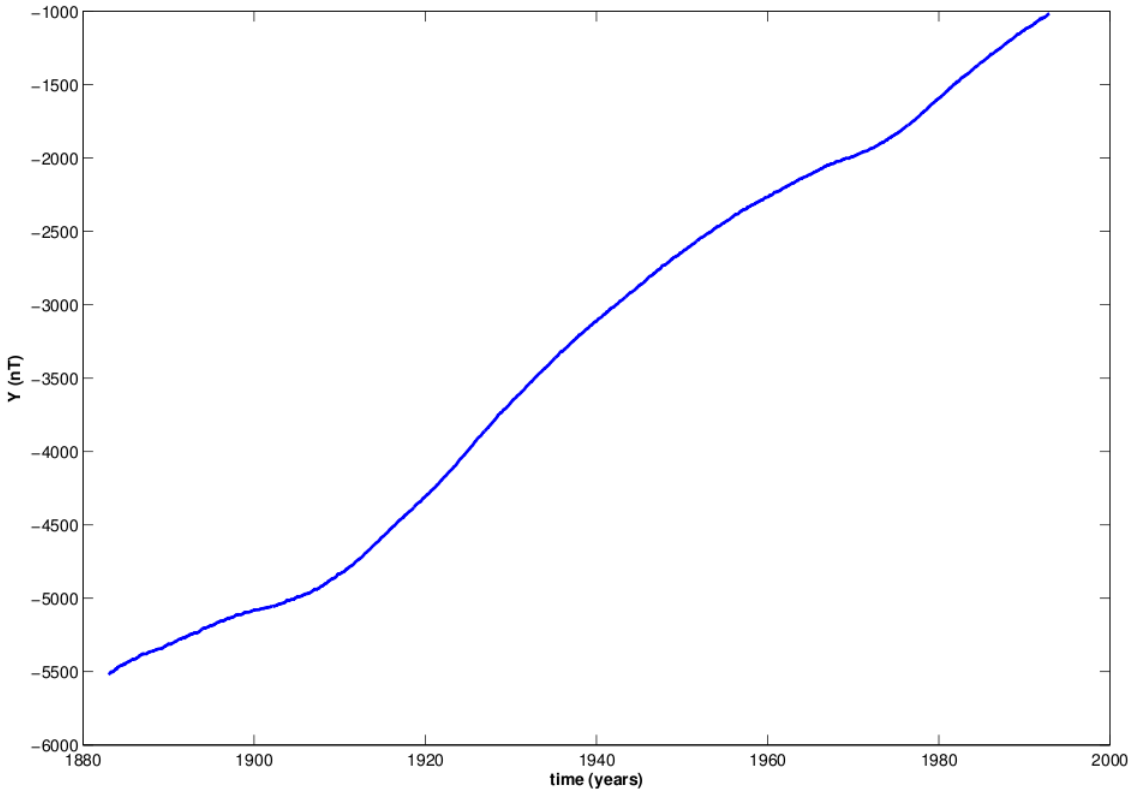

Figure 21: Plot of the Y-component of the monthly mean data from Chambon-la-Forêt magnetic observatory used in the wavelet anaylsis done by Alexandrescu et al. (1995). $t \in [1883, 1992]$.

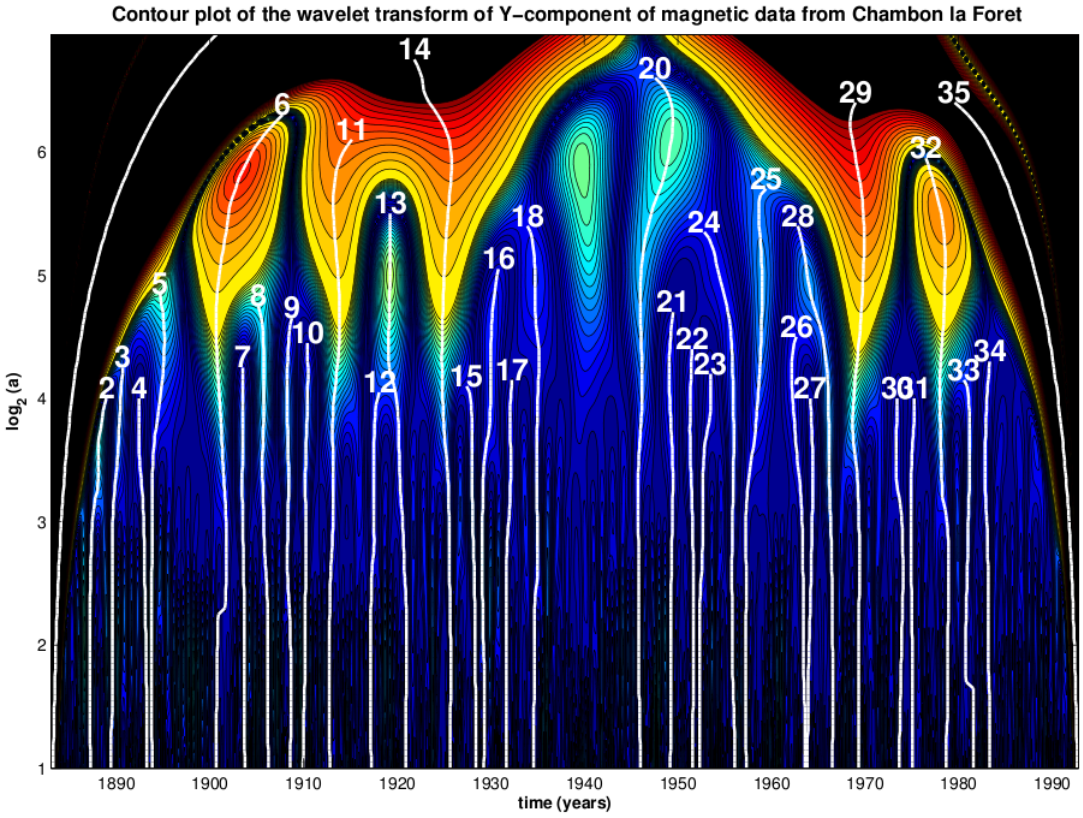

Figure 22: Contour plot of the modulus of the wavelet transform of the Y-component monthly mean data from the Chambon-la-Forêt magnetic observatory in France used by Alexandrescu et al. (1995), shown in figure 21. The longest ($log_2(a) > 4$) lines of maxima of the modulus of the wavelet transform are plotted in white and numbered chronologically. $t \in [1883, 1992]$.

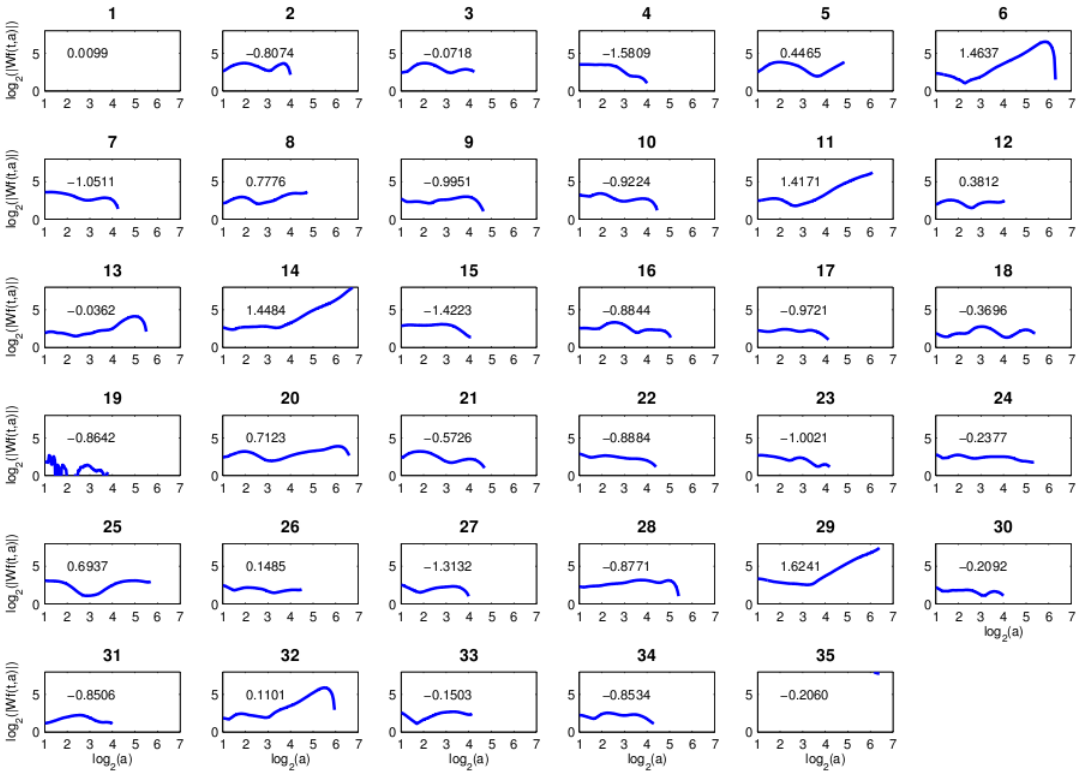

Figure 23: Log-log plot of each of the ridge functions corresponding to the lines of maxima numbered in figure 22. The recovered regularities (the slope of the ridge functions for $a > 2^{2.5}$) are labelled alongside. $a \in [2^0, 2^7]$.

From the wavelet transform shown in figure 22, five lines of maxima (lines numbered 6, 11 14, 29 and 32) emerge as possibly corresponding to geomagnetic jerks. Looking further at the ridge functions plotted in figure 23, these lines of maxima have good positive linear trends that extend into the higher dilations - characteristic of singular events. After analysing all these lines of maxima and their associated ridge functions, the algorithm 'select_jerks.m' highlights these lines of maxima as possible geomagnetic jerks. These lines of maxima and associated ridge functions are singled out in figure 24 and 25 respectively. These lines of maxima correspond to geomagnetic jerks occurring in 1901, 1913, 1925, 1969 and 1978 - as found by Alexandrescu et al. (1995).

Furthermore, if one compares the ridge functions (numbered 1 to 5) associated with the geomagnetic jerks found in this analysis (Figure 25) to those found by Alexandrescu et al. (1995) (numbered 1, 2, 4, 13 and 14 in Figure 26, respectively), a clear correspondence is evident. The recovered regularities of each of the geomagnetic jerks found in this analysis are approximately $\alpha = [1.70; 1.34; 1.67; 1.59; 1.56]$ for the ridge functions numbered 1 to 5, respectively. It is also important to show that these values closely approximate those found by Alexandrescu et al. (1995), $\alpha = [1.61; 1.47; 1.51; 1.65; 1.60]$. The difference in these values can be accounted for by this analysis using a

selected linear portion of the ridge function to calculate the slope, rather than calculating the slope of the entire ridge greater than a chosen dilation (e.g. *a_min* used in Alexandrescu et al., 1995).

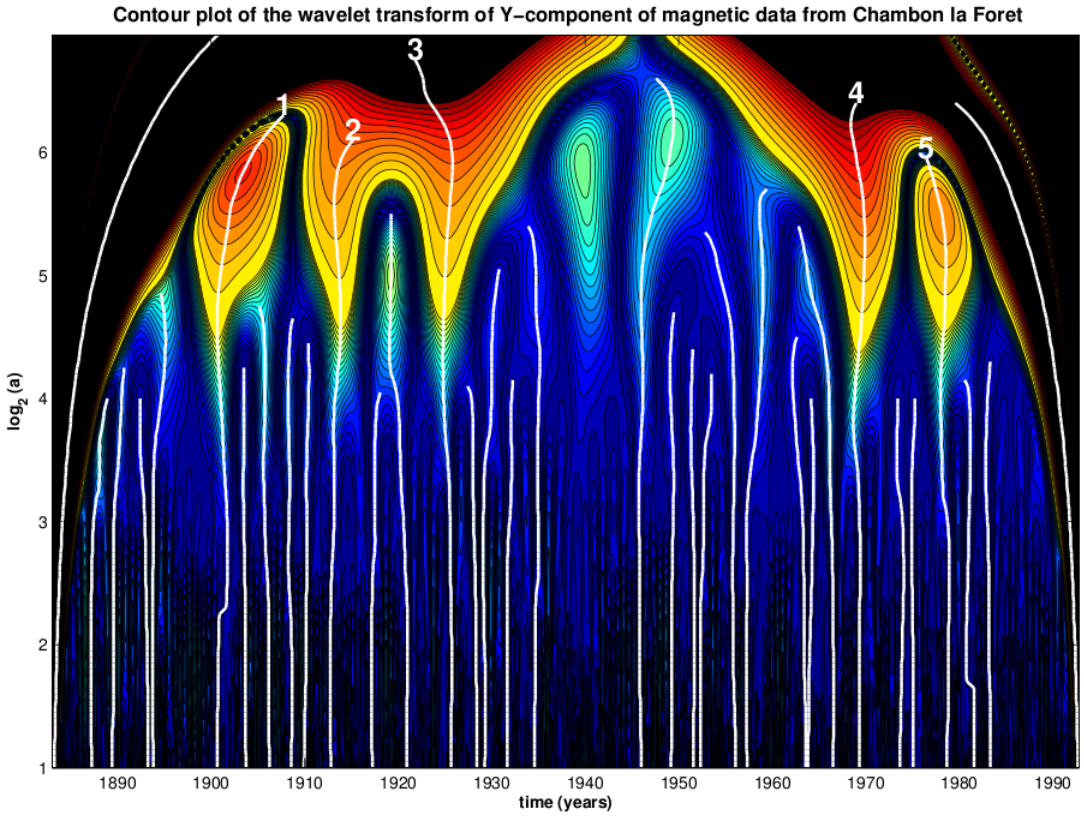

Figure 24: Contour plot of the modulus of the wavelet transform of the Y-component monthly mean data from the Chambon-la-Forêt magnetic observatory in France used by Alexandrescu et al. (1995), shown in figure 21. The longest ($log_2(a) > 4$) lines of maxima of the modulus of the wavelet transform are plotted in white, but only the lines of maxima selected as corresponding to a possible geomagnetic jerk are numbered. $t \in [1883, 1992]$.

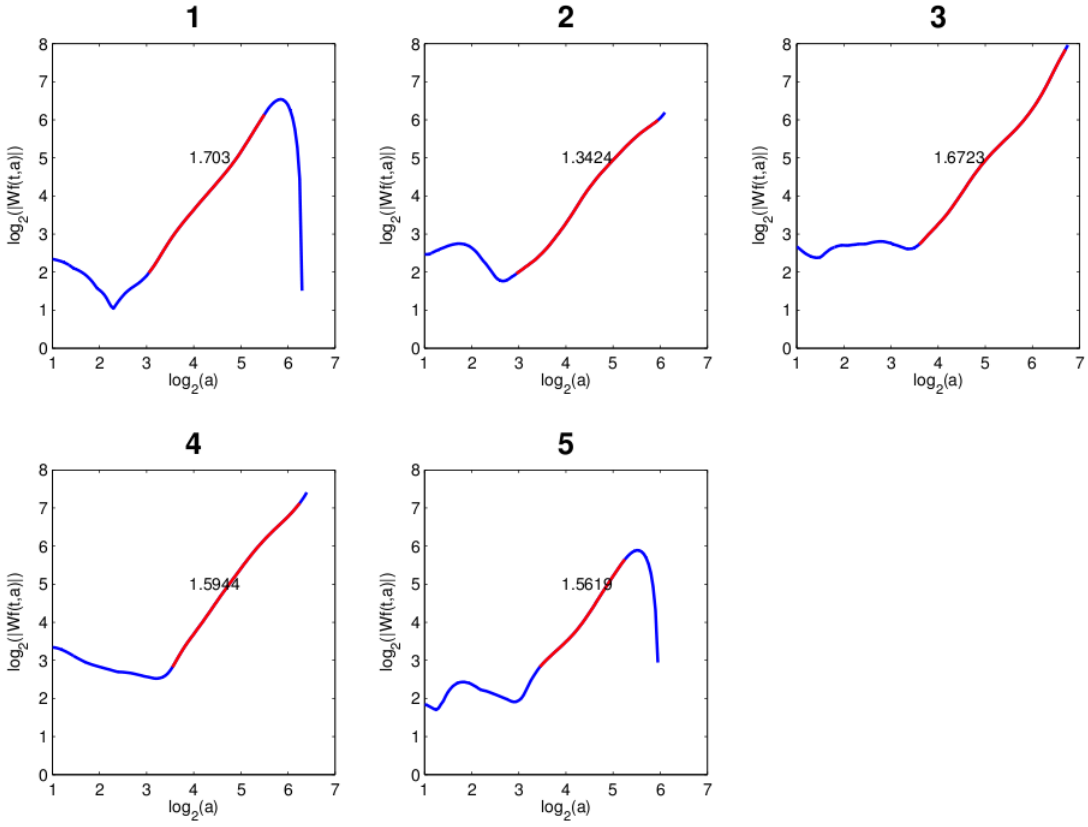

Figure 25: Log-log plot of the ridge functions corresponding to the lines of maxima indentified as possibly indicating a geomagnetic jerk and numbered in figure 24. The recovered regularities calculated from the slope of the linear portions of the ridge functions highlighted in red are labelled. $a \in [2^0, 2^7]$.

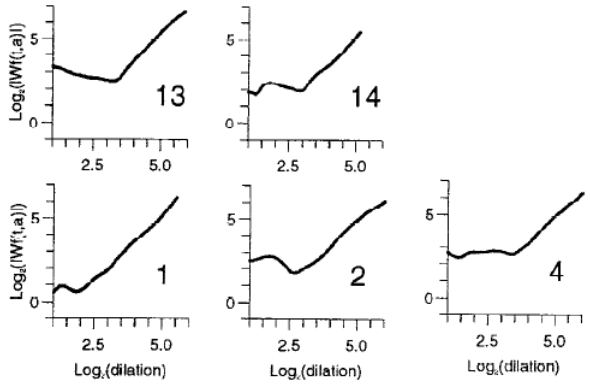

Figure 26: Log-log plot of the ridge functions corresponding to the lines of maxima associated with geomagnetic jerks found using wavelet analysis of signal shown in figure 21 by Alexandrescu et al. (1995).

Chapter 3

Data: World Monthly Means Database project

This study analyses the Y-component of monthly mean data from 45 magnetic observatories around the world. Using monthly averages is a powerful and easy-to-implement way to remove most magnetic variations of external origin, while keeping variations of internal origin (Chulliat and Telali, 2007). The data used in this study was taken from World Monthly Means Database (WMMD) project administered by the Bureau Central de Magnetisme Terrestre, BCMT (`http://www.bcmt.fr/`). WMMD contains monthly means values for all INTERMAGNET observatories calculated from WDC hourly means. The format in which the data is provided is given by Chulliat and Telali (2007) and the 'read_observatory.m' function developed was tailored to specifically interpret data of this formatting.

Not all the observatories in the INTERMAGNET network were analysed in this study. Only magnetic observatories with long time series (greater than 10 years) were chosen for analysis, otherwise convolutional edge effects from the wavelet transform would be too significant and thus eclipse detection of singularities. Furthermore, observatories were selected on the basis of the quality of their dataset. Observatories with gaps in data of more than a 1 year were excluded from the study. At the same time, consideration was also given to choose observatories so as to provide as much coverage of the Earth's surface as possible. Unfortunately, the spatial distribution of magnetic observatories around the world is extremely skewed (Figure 6) with the European region having a high number of magnetic observatories, and the observatories in rest of the world being relatively sparsely distributed. Note that Olsen and Mandea (2007) overcame this uneven distribution of ground-based magnetic observatories by rather using satellite magnetic data to analyse the 2003 geomagnetic jerk. Regardless, a compromise was met and 45 magnetic observatories were selected for the analysis (Table 2). The spatial distribution of the observatories chosen is shown on a world map in figure 27.

Note that this study only analyses the Y-component of the observatory magnetic data compared to the X- and Y-components used in Alexandrescu et al. (1996). This was done to fascillitate the entire wavelet analysis of all the observatories being done by the Matlab tool, hence determining the direction angle of a jerk by observing which angle produced the best quality ridge function would be difficult to code. As a result this could account for differences in results obtained by Alexandrescu et al. (1996) and this study (some geomagnetic jerks detected in Alexandrescu et al. (1996) might not be detected in this study). That having been said, geomagnetic jerks are most readily observed in the Y-component of observatory magnetic data (as this component is the least contaminated by external fields).

Furthermore, jerks detected in this study need not be exactly polarized in the Y-direction, but still detected. As a result, these jerks might not have perfectly formed ridge functions and hence the regularities of these singularities might not represent the true regularities of the singularities.

Table 2: Table of information about the 45 magnetic observatories chosen in this study for analysis. The short codes used to uniquely identify the magnetic observatory are a convention set by the IAGA (International Association of Geomagnetism and Aeronomy). The geodetic longitudes are given in degrees taken postive eastwards from the Greenwich Meridian. Elevation is in meters above mean sea level (AMSL). The time period details the interval of time spanned by the magnetic data from each observatory.

IAGA Code	Station Name	Geodetic Latitude (degrees)	Geodetic Longitude (degrees)	Elevation (m)	Time period
ABK	Abisko	68.358	18.823	380	1951 - 2008
AIA	Argentine Islands	-65.250	295.730	10	1957 - 2008
BLC	Baker Lake	64.318	263.988	30	1951 - 2008
BNG	Bangui	4.333	18.567	395	1955 - 2007
CLF	Chambon La Foret	48.017	2.266	145	1936 - 2008
CMO	College	64.870	212.140	197	1960 - 2008
DRV	Dumont d Urville	-66.665	140.007	30	1957 - 2008
ESK	Eskaldelmuir	55.300	356.800	245	1911 - 2008
FCC	Fort Churchill	58.759	265.912	15	1957 - 2008
FRD	Fredericksburg	38.200	282.630	69	1956 - 2008
FUR	Furstenfeldbruck	48.160	11.280	572	1940 - 2008
GNA	Gnangara	-31.800	116.000	60	1957 - 2008
GUA	Guam	13.580	144.870	140	1957 - 2008
HAD	Hartland	51.000	355.500	95	1957 - 2008
HBK	Hartebeesthoek	-25.822	27.707	1555	1972 - 2007
HER	Hermanus	-34.425	19.225	26	1941 - 2008
HON	Honolulu	21.320	202.000	4	1902 - 2008
HRB	Hurbanovo	47.860	18.190	112	1949 - 2008
HUA	Huancayo	-12.038	284.682	3336	1922 - 2008
KAK	Kakioka	36.230	140.190	36	1913 - 2008
KNY	Kanoya	31.420	130.880	107	1958 - 2008
LER	Lerwick	60.100	358.800	85	1926 - 2008
LOV	Lovoe	59.344	17.824	30	1929 - 2004
MBO	Mbour	14.392	343.042	7	1952 - 2008
MEA	Meanhook	54.616	246.653	700	1917 - 2008
MMB	Memambetsu	43.910	144.190	42	1957 - 2008
NGK	Niemegk	52.070	12.680	78	1932 - 2008
NUR	Nurmijarvi	60.508	24.655	105	1953 - 2008
NVS	Novosibirsk	54.850	83.230	130	1967 - 2008
PAF	Port Aux Fran is	-49.353	70.262	35	1957 - 2008
PPT	Pamatai	-17.567	210.426	357	1968 - 2008
RES	Resolute Bay	74.690	265.105	30	1953 - 2008
RSV	Rude Skov	55.480	12.460	48	1907 - 1980
SBA	Scott Base	-77.850	172.780	10	1964 - 2008
SIT	Sitka	57.060	224.670	24	1902 - 2008
SJG	San Juan	18.110	293.850	424	1926 - 2008
SOD	Sodankyla	67.370	26.630	178	1914 - 2008
THY	Tihany	46.900	17.540	187	1955 - 2008
TOO	Toolangi	-37.533	145.467	0	1924 - 1979
TUC	Tucson	32.170	249.270	946	1909 - 2008
VAL	Valentia	51.933	349.750	14	1957 - 2008
VIC	Victoria	48.520	236.580	197	1957 - 2008
VLJ	Val Joyeux	48.821	2.014	144	1901 - 1936
WAT	Watheroo	-30.318	115.877	0	1919 - 1958
WNG	Wingst	53.743	9.073	50	1939 - 2008

Figure 27: World map showing the spatial distribution of the magnetic observatories chosen for analysis in this study and listed in Table 2.

Chapter 4 now explores the results of the analysis of the Y-component of the monthly mean data from the selected magnetic observatories using the Matlab wavelet tool outlined above.

Chapter 4

Results and Interpretations

The wavelet tool, outlined in subsection 2.3, is applied to the Y-component of monthly mean data from 45 selected magnetic observatories (Table 2), described in section 3, the results of which are explored in this chapter.

After the results of the wavelet analyses were executed on all the observatory data, the lines of maxima (and related ridge functions) selected by the algorithm as possibly corresponding to geomagnetic jerks were visually inspected and erroneous results excluded. The algorithm designated to determining whether lines of maxima correspond to geomagnetic jerks employs a liberal interpretation of the signature of geomagnetic jerks characterised from the synthetic tests - i.e. lines of maxima that extend into the higher dilations and ridge functions that display a linear trend. This characterisation is very loosely defined and aids merely as a guideline to the selection process. For example, lines of maxima with a strong linear ridge function, but that do not extend into the highest dilations because of interference with convolutional edge effects, should not be discounted. The associated energy packets are used in an effort to help this selection process.

4.1 Wavelet transforms and log-log plots

An example of the results obtained from the analysis is given in the subsection below, the remaining results (e.g. figures from all other observatories) are provided in appendix B.

4.1.1 Hartland Magnetic Observatory, United Kingdom

The results of wavelet analysis applied to Hartland Magnetic Observatory were chosen here as an example because the wavelet transform (Figure 28) indicated very little evidence of external contributions. Furthermore, clearly discernible energy packets in the higher order dilations corresponding to geomagnetic jerks can be visually identified.

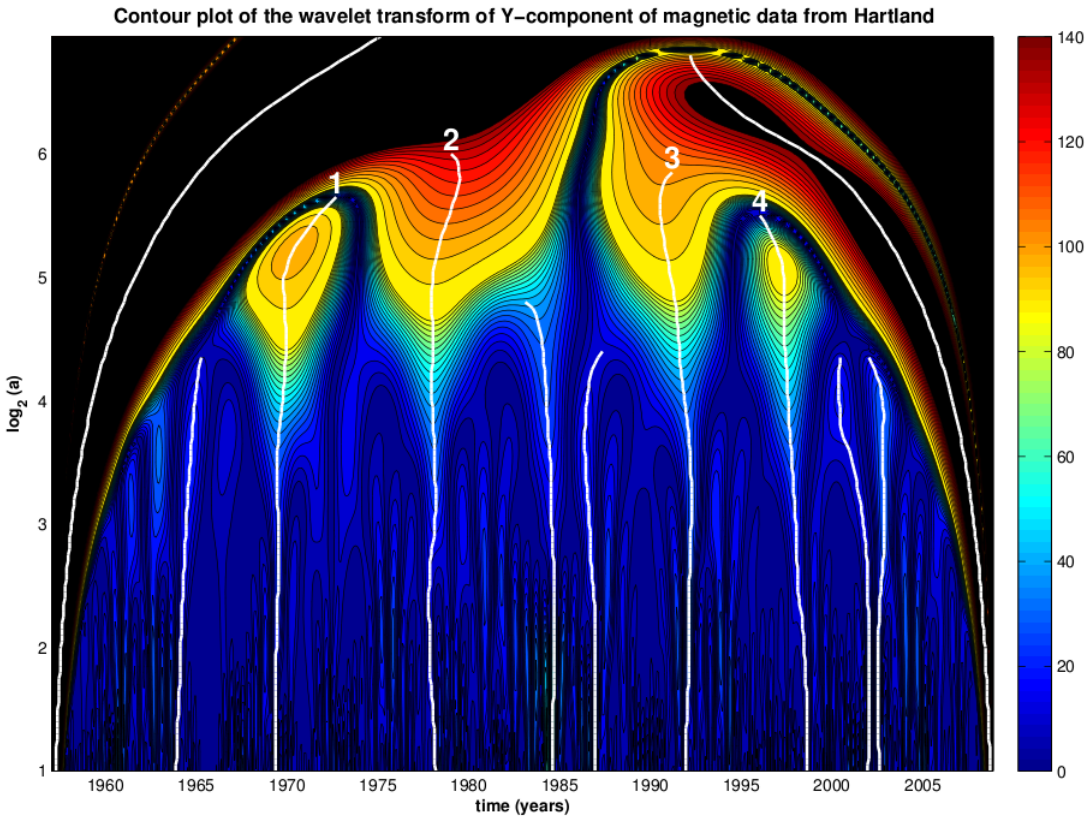

Figure 28: Contour plot of the modulus of the wavelet transform of the Y-component monthly mean data from the Hartland magnetic observatory in the United Kingdom. The longest ($log_2(a) > 4$) lines of maxima of the modulus of the wavelet transform are plotted in white, but only the lines of maxima selected as corresponding to a possible geomagnetic jerk are numbered. $t \in [1956, 2006]$.

Of the lines of maxima indicated on the contour plot of the wavelet transform (Figure 28), four ridge functions display positive linear trends and extend into the higher order dilations, indicative of singular events, or geomagnetic jerks. The corresponding lines of maxima indicate that these jerks occurred in approximately 1969, 1978, 1992 and 1998 - consistent with the findings of other studies (e.g. Alexandrescu et al., 1996; Mandea et al., 2000). Moreover, the recovered regularities of the four jerks selected in the signal are 1.79, 1.75, 1.54 and 1.17 respectively (Figure 29). These results concur with findings by Alexandrescu et al. (1995, 1996) for the recovered regularities of geomagnetic jerks.

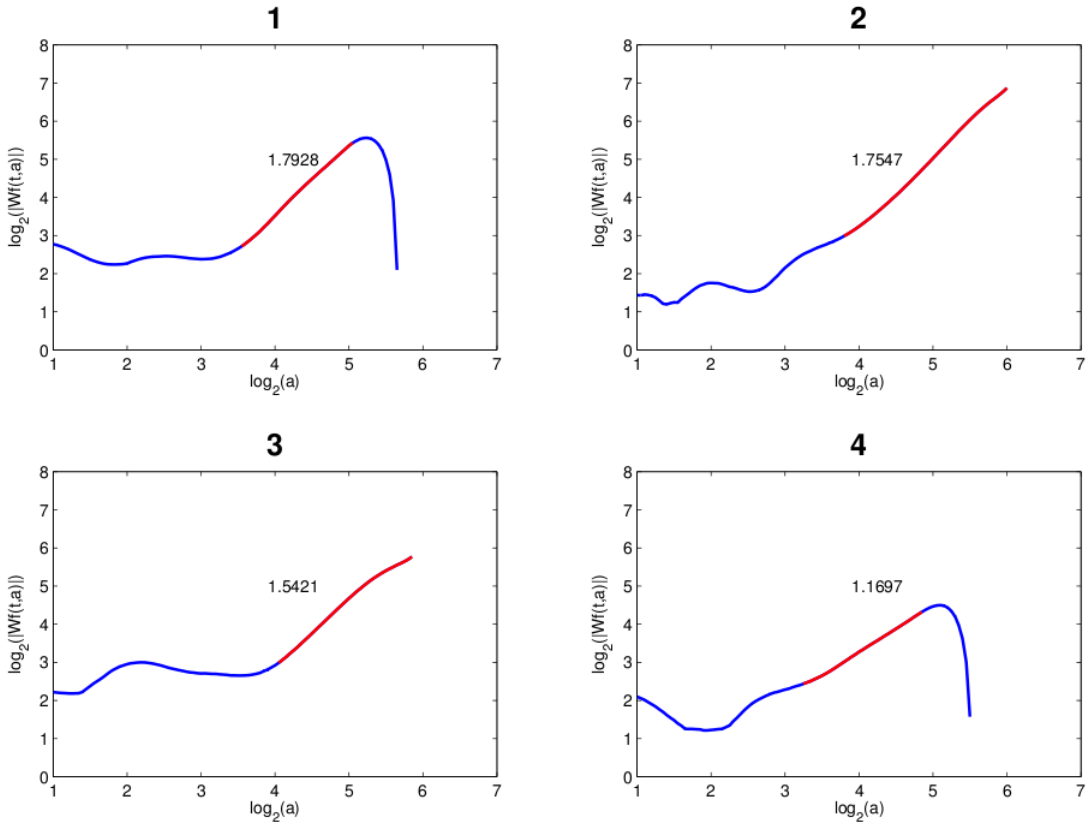

Figure 29: Log-log plot of the ridge functions corresponding to the lines of maxima indentified as possibly indicating a geomagnetic jerk and numbered in figure 28. The recovered regularities calculated from the slope of the linear portions of the ridge functions highlighted in red are labelled. $a \in [2^0, 2^7]$.

4.2 Combined results

Using the results from the wavelet analysis applied to each of the magnetic observatories (Table 2), the distribution of all the geomagnetic jerks detected is plotted in a histogram (Figure 30).

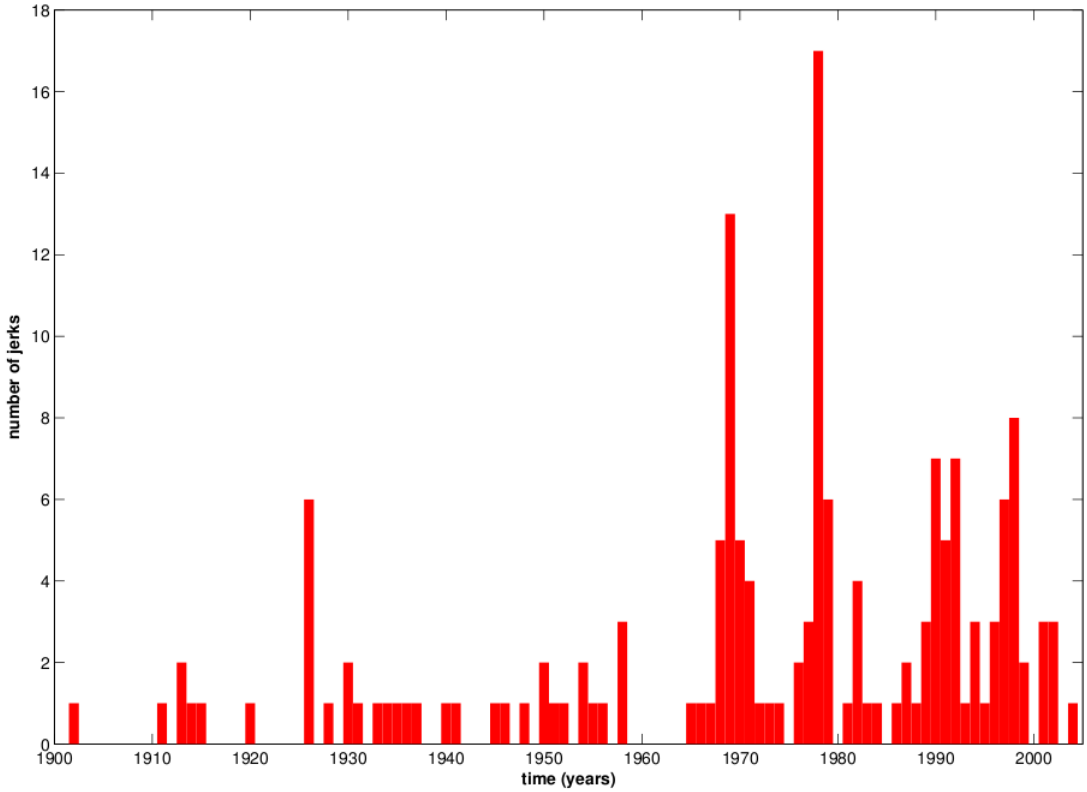

Figure 30: Histogram plot of geomagnetic jerks detected using the wavelet analysis tool on data from all of the magnetic observatories listed in Table 2. The width of each of the columns is 1 year.

From the histogram, clusters of geomagnetic jerks can be observed. These clusters were more clearly identified (Figure 31) using a k-means clustering technique (see Bishop, 1995). The clusters were initialized at the dates of geomagnetic jerks found by other studies (e.g. Alexandrescu et al., 1996; Mandea et al., 2000; Olsen and Mandea, 2007) and then outliers (geomagnetic jerks greater than two standard deviations from the mean of the cluster) were excluded.

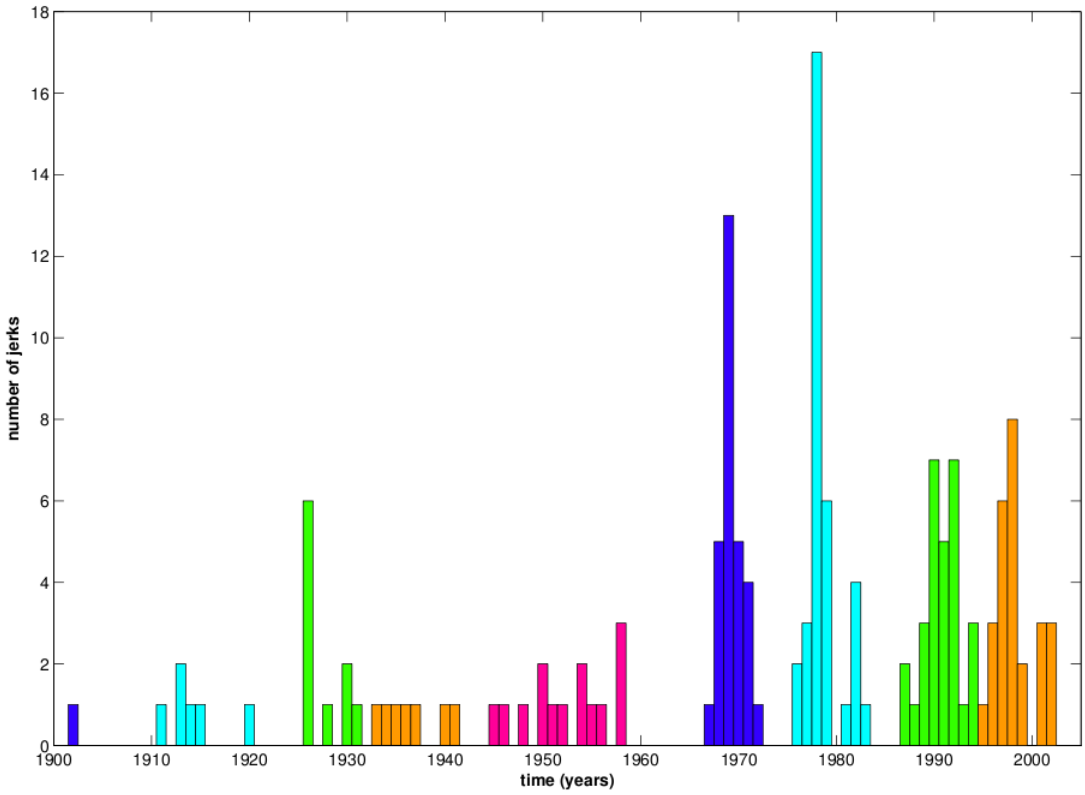

Figure 31: Histogram plot of the clusters of the geomagnetic jerks (from Figure 30) determined using k-means clustering. Clusters are highlighted in different colour for easy visual differentiation. Outliers of each of the clusters were excluded. The width of each of the columns is 1 year.

From this clustering of geomagnetic jerks, the mean date on which jerks, in a given cluster, were detected as occurring was calculated, and their respective standard deviations determined. Furthermore, the mean and standard deviation of the recovered regularities of these clusters of jerks was also calculated (Table 3). The number of magnetic observatories that detected a geomagnetic jerk to have occurred in a particular cluster were also determined with respect to the number of observatories that had magnetic data covering that particular time period.

Table 3: Table outlining details of the clusters of geomagnetic jerks detected. The date of jerk represents the mean date on which jerks, in a given cluster, were detected as occuring. The mean of the recovered regularities of each of jerks in the cluster are provided. Errors are provided at one standard deviation. The number of detections is given as the number of magnetic observatories that detected a geomagnetic jerk to have occured in a particular cluster out of the number of observatories that had magnetic data covering that particular time period; the percentages of which are given.

Date of jerk	Regularity	Number of detections	Percentage detection
1901.7 ± 0	1.60 ± 0	1 out of 1	100%
1914.3 ± 2.9	1.41 ± 0.18	5 out of 8	63%
1927.4 ± 2.2	1.55 ± 0.17	9 out of 14	64%
1936.6 ± 3	1.35 ± 0.16	6 out of 16	38%
1952.5 ± 4.4	1.39 ± 0.27	9 out of 23	39%
1969.4 ± 1	1.55 ± 0.3	29 out of 42	69%
1978.6 ± 1.8	1.43 ± 0.33	34 out of 43	79%
1990.8 ± 1.9	1.35 ± 0.25	29 out of 41	71%
1998.3 ± 2	1.41 ± 0.29	26 out of 41	63%

These clusterings of geomagnetic jerks are consistent with geomagnetic jerks found by Alexandrescu et al. (1996) to have occurred in 1901, 1913, 1925, 1936, 1949, 1969 and 1978; by Macmillan (1996) to have occurred in 1992; and by Mandea et al. (2000) to have occurred in 1999. Furthermore, the errors in date of occurrence of 1969, 1978 and 1990 geomagnetic jerks are also consistent with errors found by Pinheiro et al. (2011). The mean recovered regularity of all the jerks detected in the analysis was calculated as 1.42 ± 0.28.

The following subsections provide the details of each of the clusters of geomagnetic jerks shown in Table 3. Tables detailing each jerk detected in that cluster and plots of the ridge functions associated with each detected jerk are provided for further analysis.

4.2.1 1901

The only geomagnetic jerk detected to have occurred in this cluster was found by the original data from Chambon-la-Forêt Magnetic Observatory used in the Alexandrescu et al. (1995) study. Since this is the only magnetic observatory data used in this study with time data that extends this far back in time, the spatial extent of this jerk cannot be further discussed.

4.2.2 1914

The results of the geomagnetic jerks detected in the cluster around 1914 are provided in Table 4. Plots of the associated ridge functions of each of jerks detected are also provided (Figure 32). Of the 7 magnetic observatories that had data covering this period of time, 5 different observatories detected the occurrence of these geomagnetic jerks.

Table 4: Table detailing each of the geomagnetic jerks detected to have occured around 1914.

Observatory IAGA code	Date of jerk	Regularity
CLF	1912.8	1.33
HON	1919.6	1.55
RSV	1913.8	1.40
SIT	1911.4	1.10
SIT	1915.1	1.55
VLJ	1913.0	1.51

Note that two jerks were detected by Sitka Magnetic Observatory (SIT) during this period. This can rather be interpreted as the detection of two lines of maxima corresponding to the same geomagnetic jerk occurring in the interval between these dates. Remember that dating exactly when a detected geomagnetic jerk has occurred is not always accurate due to external contributions interfering with lines of maxima passing through the lower dilations.

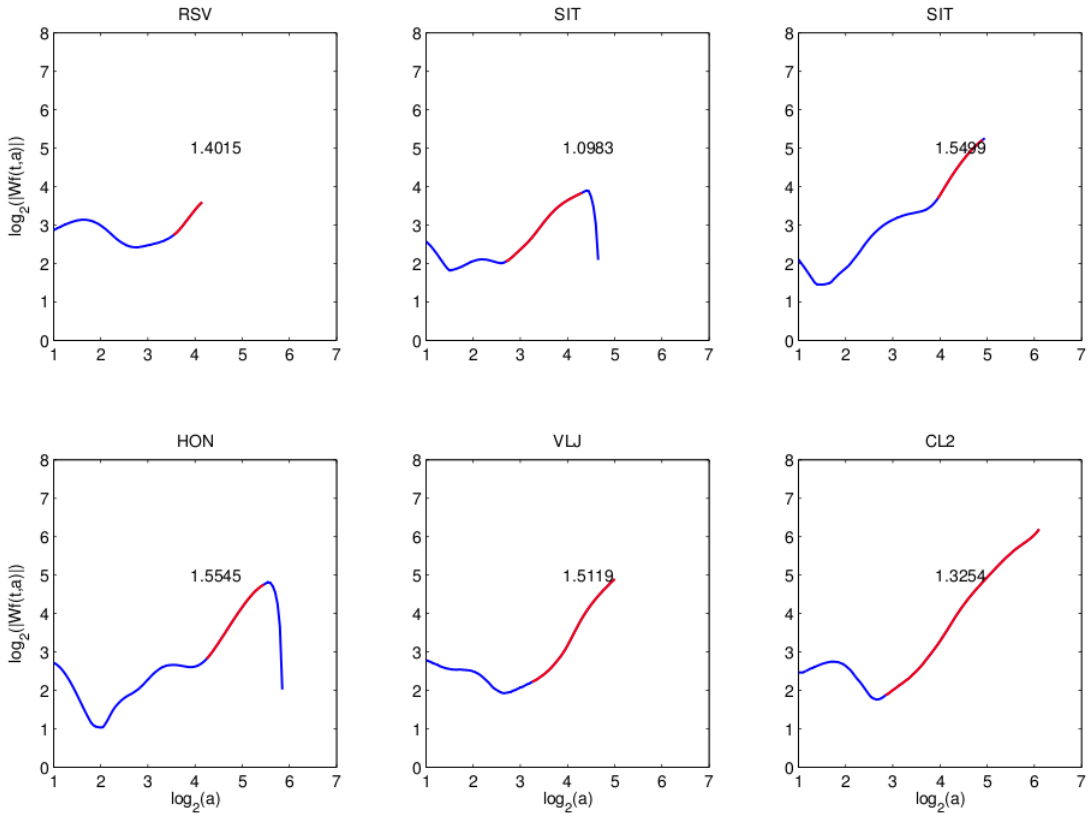

Figure 32: Log-log plot of the ridge functions of each of the geomagnetic jerks to have been detected around 1914 (Table 4). IAGA code of the magnetic observatories that detected each of the jerks is provided in the title of each subplot. The recovered regularities calculated from the slope of the linear portions of the ridge functions highlighted in red are labelled. $a \in [2^0, 2^7]$.

4.2.3 1927

The results of the geomagnetic jerks detected in the cluster around 1927 are provided in Table 5. Plots of the associated ridge functions of each of the jerks detected are also provided (Figure 33). Of the 14 magnetic observatories that had data covering this period of time, 9 different observatories detected the occurrence of these geomagnetic jerks. Again, note that two jerks were detected by Watheroo Magnetic Observatory (WAT) during this period, but it is likely that these are two lines of maxima corresponding to the same jerk.

Table 5: Table detailing each of the geomagnetic jerks detected to have occured around 1927.

Observatory IAGA code	Date of occurrence of jerk	Regularity
CLF	1925.7	1.67
ESK	1925.8	1.35
HON	1930.2	1.46
KAK	1930.8	1.41
RSV	1925.8	1.35
SIT	1925.9	1.37
TUC	1925.6	1.80
VLJ	1925.7	1.67
WAT	1927.9	1.67
WAT	1930.3	1.72

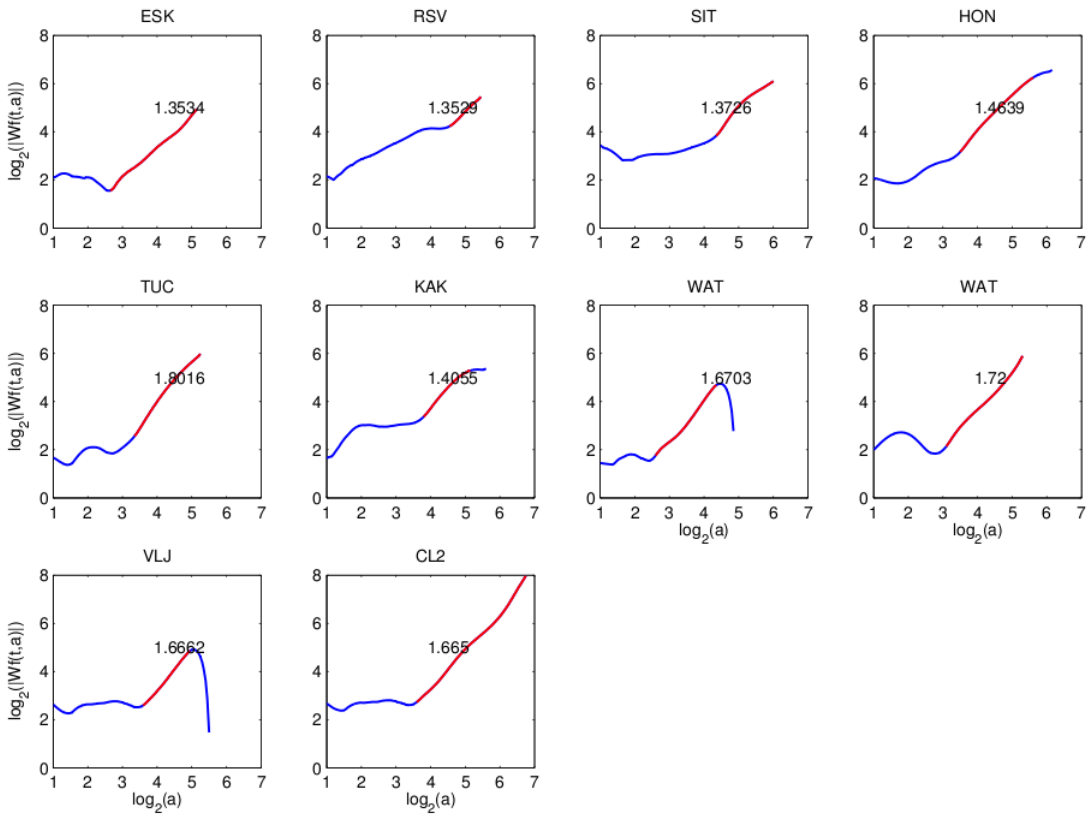

Figure 33: Log-log plot of the ridge functions of each of the geomagnetic jerks to have been detected around 1927 (Table 5). IAGA code of the magnetic observatories that detected each of the jerks is provided in the title of each subplot. The recovered regularities calculated from the slope of the linear portions of the ridge functions highlighted in red are labelled. $a \in [2^0, 2^7]$.

4.2.4 1936

The results of the geomagnetic jerks detected in the cluster around 1936 are provided in Table 6. Plots of the associated ridge functions of each of jerks detected are also provided (Figure 34). Of the 16 magnetic observatories that had data covering this period of time, 6 different observatories detected the occurrence of these geomagnetic jerks.

Table 6: Table detailing each of the geomagnetic jerks detected to have occured around 1936.

Observatory IAGA code	Date of occurrence of jerk	Regularity
ESK	1935.7	1.33
HUA	1941.1	1.25
HUA	1933.4	1.49
KAK	1937.3	1.61
RSV	1934.7	1.25
SOD	1934.0	1.12
WAT	1940.1	1.36

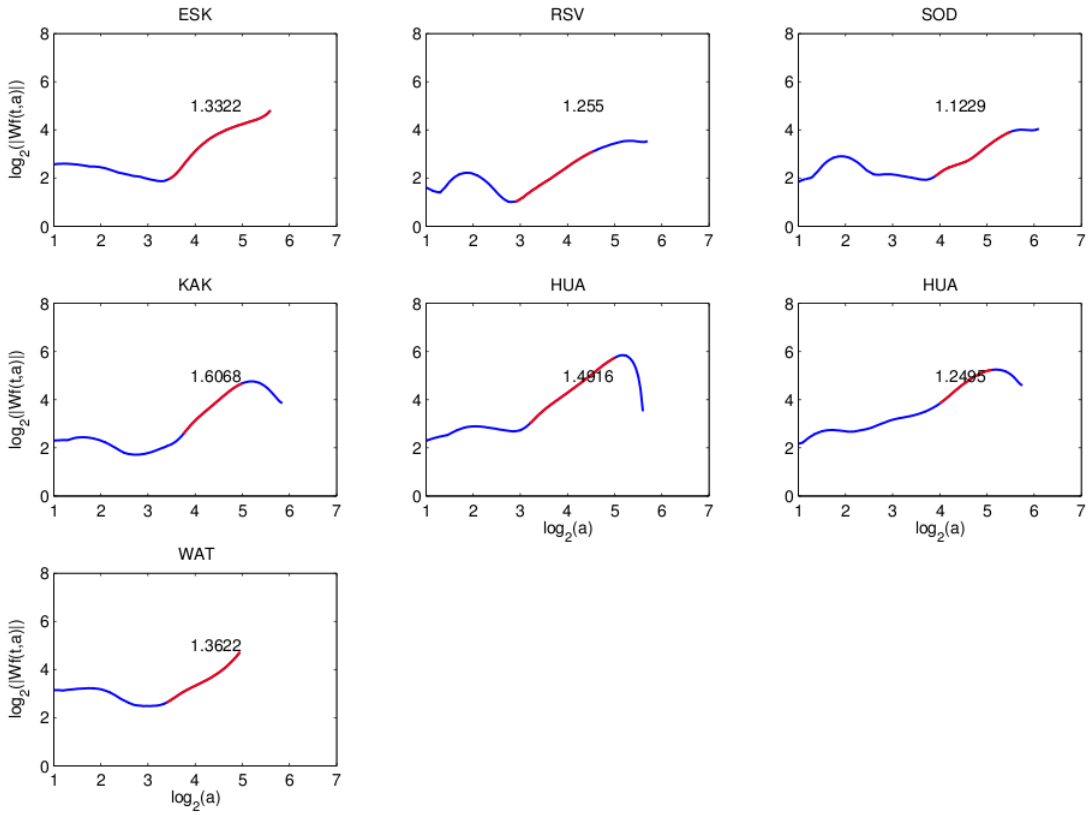

Figure 34: Log-log plot of the ridge functions of each of the geomagnetic jerks to have been detected around 1936 (Table 6). IAGA code of the magnetic observatories that detected each of the jerks is provided in the title of each subplot. The recovered regularities calculated from the slope of the linear portions of the ridge functions highlighted in red are labelled. $a \in [2^0, 2^7]$.

4.2.5 1952

The results of the geomagnetic jerks detected in the cluster around 1952 are provided in Table 7. Plots of the associated ridge functions of each of jerks detected are also provided (Figure 35). Of the 23 magnetic observatories that had data covering this period of time, 9 different observatories detected the occurrence of these geomagnetic jerks.

Table 7: Table detailing each of the geomagnetic jerks detected to have occured around 1952.

Observatory IAGA code	Date of occurrence of jerk	Regularity
HER	1954.3	1.85
HON	1956.0	1.63
KAK	1951.4	1.07
KAK	1954.0	1.20
LOV	1950.0	1.39
SJG	1945.0	1.34
SJG	1957.8	1.54
SOD	1951.7	1.50
TOO	1948.3	0.83
TOO	1955.1	1.46
TOO	1957.9	1.18
TUC	1946.0	1.72
TUC	1958.2	1.29
WAT	1949.7	1.46

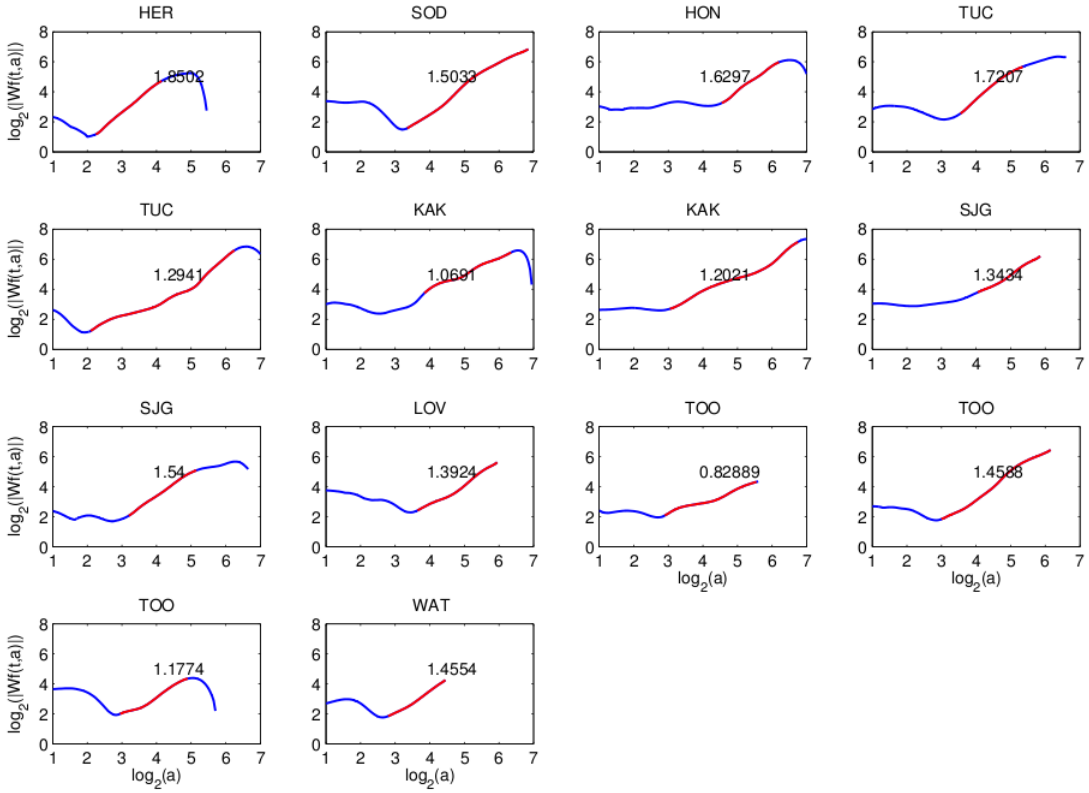

Figure 35: Log-log plot of the ridge functions of each of the geomagnetic jerks to have been detected around 1952 (Table 7). IAGA code of the magnetic observatories that detected each of the jerks is provided in the title of each subplot. The recovered regularities calculated from the slope of the linear portions of the ridge functions highlighted in red are labelled. $a \in [2^0, 2^7]$.

4.2.6 1969

The results of the geomagnetic jerks detected in the cluster around 1969 are provided in Table 8. Plots of the associated ridge functions of each of jerks detected are also provided (Figure 36). Of the 42 magnetic observatories that had data covering this period of time, 29 different observatories detected the occurrence of these geomagnetic jerks.

Table 8: Table detailing each of the geomagnetic jerks detected to have occured around 1969.

Observatory IAGA code	Date of occurrence of jerk	Regularity
ABK	1968.2	1.65
CLF	1968.0	1.29
CMO	1969.5	1.07
DRV	1969.0	1.17
ESK	1968.3	1.58
FCC	1969.5	1.08
FUR	1969.5	1.56
GNA	1970.6	1.67
GUA	1967.2	1.60
HAD	1969.5	1.79
HRB	1968.0	1.93
HUA	1969.5	0.72
KAK	1969.6	1.52
LER	1969.5	1.56
LOV	1969.5	1.54
MBO	1968.0	1.32
MEA	1971.0	1.45
MMB	1971.0	1.69
NGK	1969.5	1.62
NUR	1969.5	1.73
RES	1972.0	1.89
RSV	1969.5	1.87
SIT	1969.4	1.66
SJG	1969.1	1.21
SOD	1969.5	1.46
THY	1970.9	1.52
VAL	1969.5	2.12
WNG	1969.4	1.68

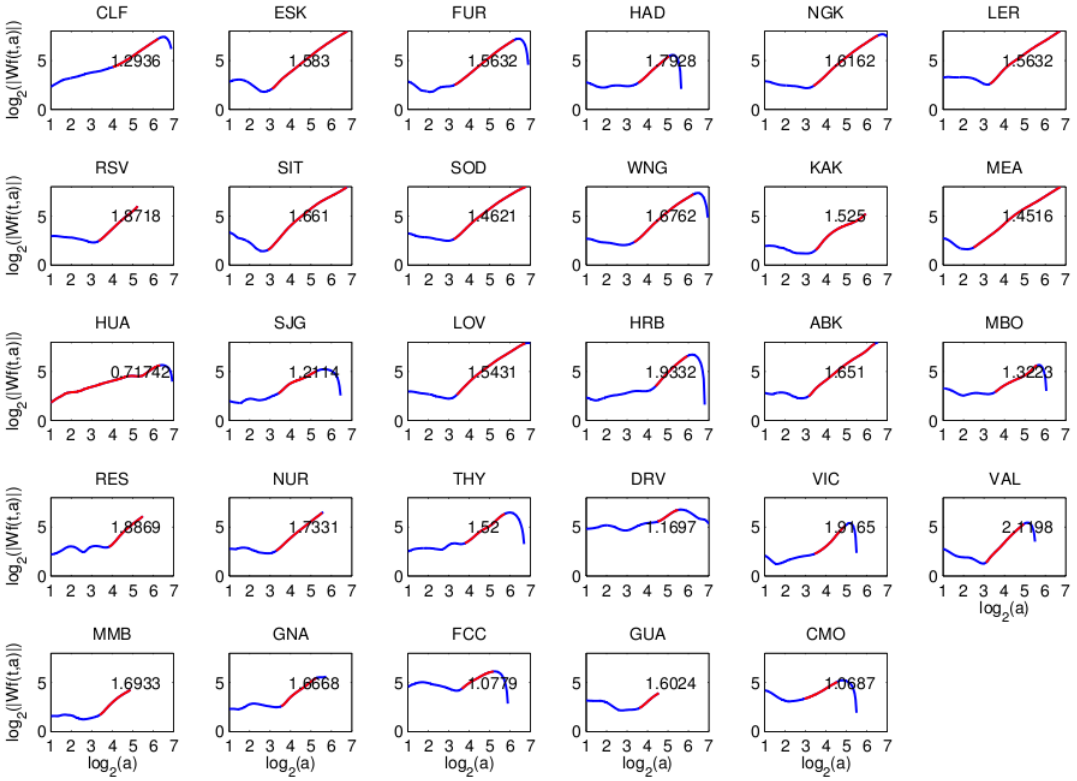

Figure 36: Log-log plot of the ridge functions of each of the geomagnetic jerks to have been detected around 1969 (Table 8). IAGA code of the magnetic observatories that detected each of the jerks is provided in the title of each subplot. The recovered regularities calculated from the slope of the linear portions of the ridge functions highlighted in red are labelled. $a \in [2^0, 2^7]$.

4.2.7 1978

The results of the geomagnetic jerks detected in the cluster around 1978 are provided in Table 9. Plots of the associated ridge functions of each of jerks detected are also provided (Figure 37). Of the 43 magnetic observatories that had data covering this period of time, 34 different observatories detected the occurrence of these geomagnetic jerks.

Table 9: Table detailing each of the geomagnetic jerks detected to have occured around 1978.

Observatory IAGA code	Date of occurrence of jerk	Regularity
CLF	1979.0	1.51
HER	1982.4	1.57
ESK	1977.8	1.41
FUR	1977.8	1.53
HAD	1977.8	1.75
NGK	1978.0	1.31
LER	1977.6	1.79
SIT	1977.9	1.22
SOD	1977.8	1.21
WNG	1977.9	1.47
HON	1976.9	1.71
HON	1982.5	1.13
TUC	1977.8	1.74
KAK	1978.2	1.66
HUA	1982.4	1.31
SJG	1980.6	1.89
LOV	1978.1	1.13
HRB	1978.5	1.36
BLC	1978.0	1.26
ABK	1977.7	1.29
RES	1979.0	0.84
NUR	1977.8	1.49
THY	1977.3	1.39
FRD	1979.0	1.77
PAF	1976.7	0.82
VIC	1975.8	1.55
VAL	1978.8	1.57
GNA	1978.7	1.44
FCC	1978.5	1.39
GUA	1977.6	2.02
AIA	1976.3	0.91
KNY	1978.3	2.06
CMO	1982.6	0.64
HBK	1982.3	1.49

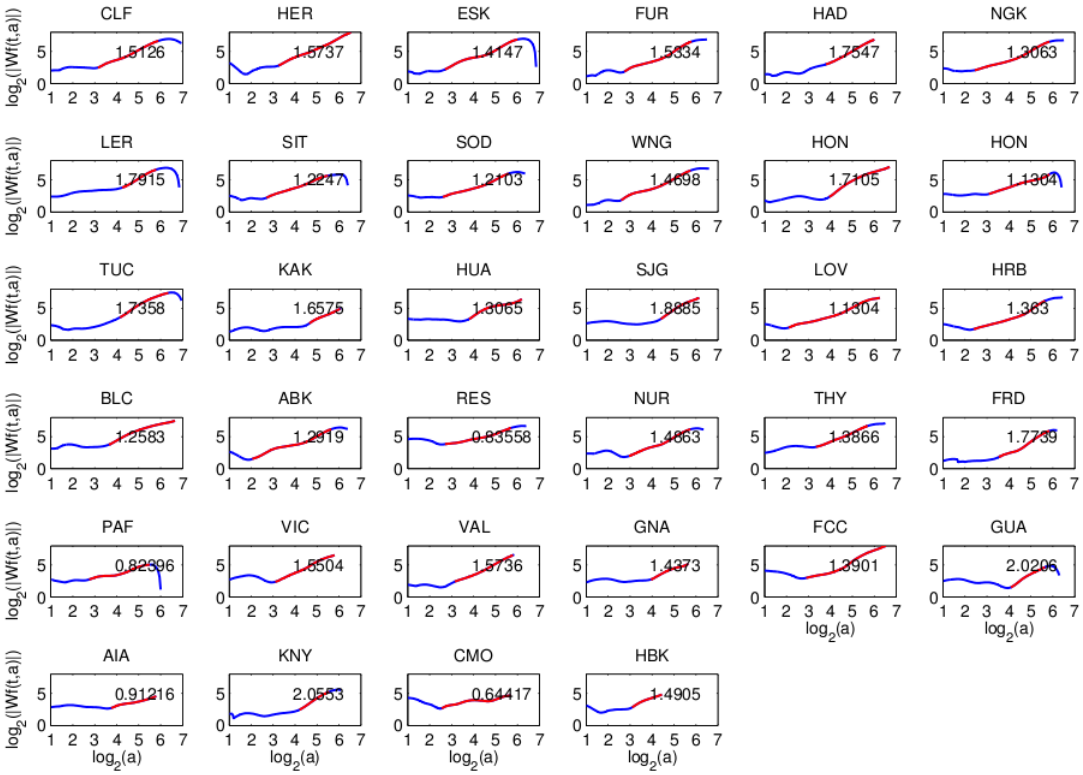

Figure 37: Log-log plot of the ridge functions of each of the geomagnetic jerks to have been detected around 1978 (Table 9). IAGA code of the magnetic observatories that detected each of the jerks is provided in the title of each subplot. The recovered regularities calculated from the slope of the linear portions of the ridge functions highlighted in red are labelled. $a \in [2^0, 2^7]$.

4.2.8 1990

The results of the geomagnetic jerks detected in the cluster around 1990 are provided in Table 10. Plots of the associated ridge functions of each of jerks detected are also provided (Figure 38). Of the 41 magnetic observatories that had data covering this period of time, 29 different observatories detected the occurrence of these geomagnetic jerks. Note that from Hartebeesthoek (HBK) data two geomagnetic jerks were detected to have occurred around 1990, although the later of which could rather correspond to the 1998 geomagnetic jerk.

Table 10: Table detailing each of the geomagnetic jerks detected to have occured around 1990.

Observatory IAGA code	Date of occurrence of jerk	Regularity
ABK	1990.5	1.23
AIA	1991.9	1.25
BNG	1992.9	1.19
CLF	1992.1	1.37
ESK	1989.5	0.82
FRD	1988.8	1.36
FUR	1990.6	1.36
HAD	1992.1	1.54
HBK	1987.0	1.82
HBK	1994.0	1.45
HER	1986.6	1.44
HRB	1990.6	1.71
KNY	1989.2	1.20
LER	1990.5	1.57
LOV	1990.5	1.35
MBO	1994.0	1.24
NGK	1990.5	1.55
NUR	1990.5	1.31
NVS	1994.0	1.14
PAF	1987.9	0.86
PPT	1988.9	1.19
SBA	1990.2	1.13
SIT	1992.0	1.23
SOD	1990.5	1.22
THY	1989.8	1.30
TUC	1992.1	1.94
VAL	1992.1	1.36
VIC	1992.2	1.66
WNG	1990.5	1.44

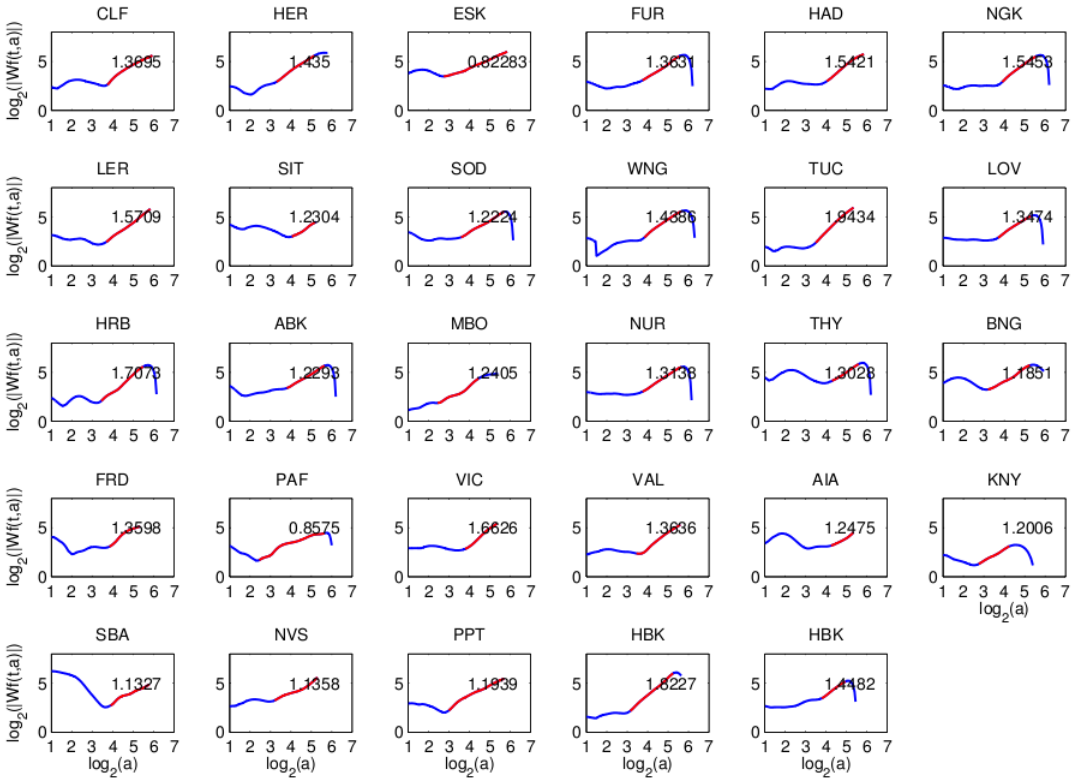

Figure 38: Log-log plot of the ridge functions of each of the geomagnetic jerks to have been detected around 1990 (Table 10). IAGA code of the magnetic observatories that detected each of the jerks is provided in the title of each subplot. The recovered regularities calculated from the slope of the linear portions of the ridge functions highlighted in red are labelled. $a \in [2^0, 2^7]$.

4.2.9 1998

The results of the geomagnetic jerks detected in the cluster around 1998 are provided in Table 11. Plots of the associated ridge functions of each of jerks detected are also provided (Figure 39). Of the 41 magnetic observatories that had data covering this period of time, 26 different observatories detected the occurrence of these geomagnetic jerks.

Table 11: Table detailing each of the geomagnetic jerks detected to have occured around 1998.

Observatory IAGA code	Date of occurrence of jerk	Regularity
ABK	1996.7	1.58
CLF	1998.2	1.32
FCC	1995.0	0.95
FCC	1998.7	1.48
FRD	2000.7	1.35
FUR	1996.6	1.60
GNA	1999.1	1.89
GUA	2002.0	1.19
HAD	1998.1	1.17
HER	1996.0	1.16
HUA	1996.8	0.98
KAK	2001.9	1.81
KNY	2001.8	1.32
LER	1996.9	1.11
LOV	1996.7	1.73
MBO	1998.4	1.22
MEA	1996.1	1.75
MMB	2001.0	1.80
NGK	1998.2	1.21
NUR	1998.3	1.66
NVS	2000.8	1.55
PAF	1995.9	1.74
RES	1998.0	1.25
SOD	1996.7	1.37
VAL	1998.3	0.91
WNG	1998.3	1.53

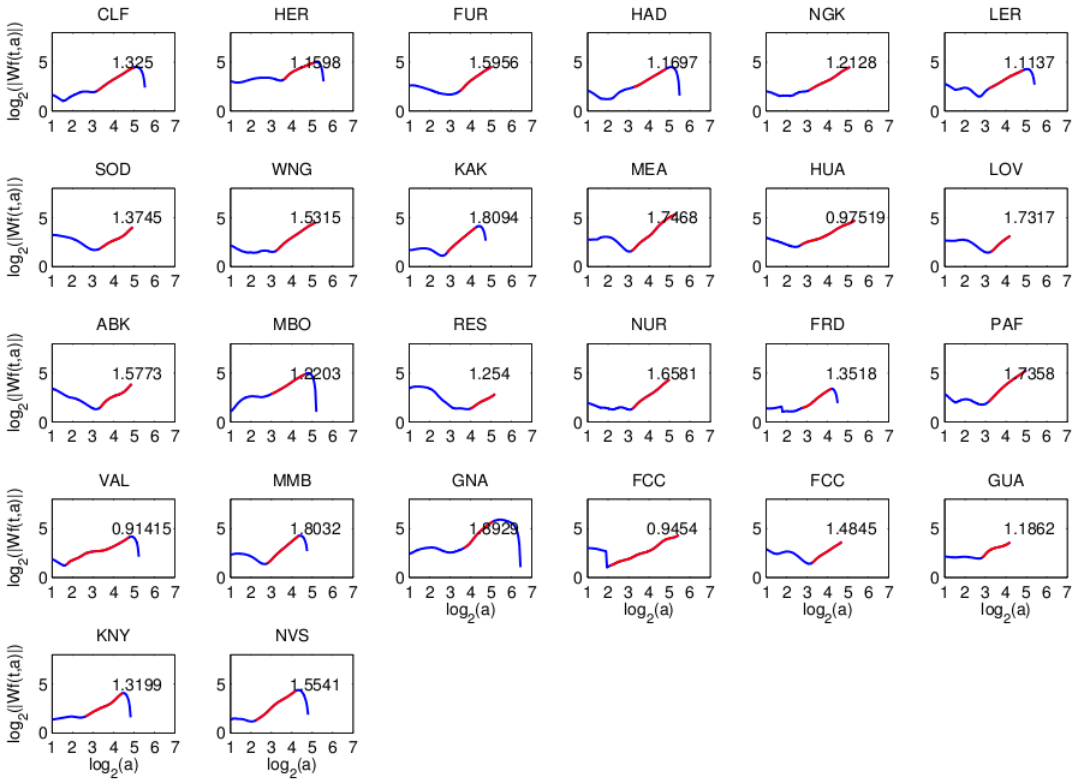

Figure 39: Log-log plot of the ridge functions of each of the geomagnetic jerks to have been detected around 1998 (Table 11). IAGA code of the magnetic observatories that detected each of the jerks is provided in the title of each subplot. The recovered regularities calculated from the slope of the linear portions of the ridge functions highlighted in red are labelled. $a \in [2^0, 2^7]$.

In summary, nine geomagnetic jerks have been found to have occurred in the past century; in 1901, 1914, 1927, 1936, 1952, 1969, 1978, 1990 and 1998. However, these jerks were not detected at every observatory where records covered these periods of time. Looking at the number of magnetic observatories that detected a geomagnetic jerk to have occurred in a particular cluster compared to of the number of observatories that had magnetic data covering that particular time period, the detected jerks do not seem all of the same global coverage. In particular, the jerks detected occurring in 1936 and 1952 have not been detected globally and jerks detected occurring in 1901, 1914 and 1927 are detected by many of the observatories, but given the small number of observatories with long enough records to allow for detection during this period, it is difficult to assess their global extent. On the other hand, the jerks occurring in 1969, 1978, 1990 and 1998 are well documented at many of the magnetic observatories.

It is interesting at this stage to compare the results of the geomagnetic jerks detected here and the phase jumps detected in the Chandler wobble by Bellanger et al. (2002). Figure 40, below, displays the geomagnetic jerks detected

in this study (red dots) alongside the phase jumps detected in the Chandler wobble (black dots). The errors associated with dates on which were jerks detected in this study are included. This remarkable correlation between these two phenomena further highlights the possible genetic relationship between them.

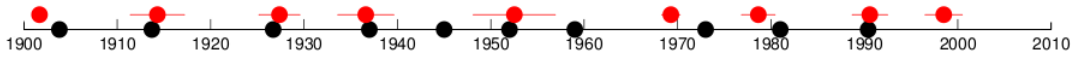

Figure 40: Timeline of the occurance of geomagnetic jerks detected in this study (red dots), with associated error bars (one standard devaition from the mean), and the occurance of phase jumps detected in the Chandler wobble by Bellanger et al., 2002 (black dots).

The spatio-temporal behaviour of these jerks is explored in next subsection.

4.3 Spatio-temporal behaviour

The spatio-temporal behaviour of the 1969, 1978, 1990 and 1998 geomagnetic jerks is explored. For each cluster of jerks, k-means clustering is again applied ($k = 3$). The choice of k was made by inspection of the associated squared error of various choices of k. From a practical point of view, this choice makes sense as k-means clustering is expected to divide the detected jerks associated with a certain cluster into three practical categories: “early arrivals”, “the majority” and “late arrivals”.

For each of the jerk clusters, a histogram plot highlights the results of the k-means clustering applied to that cluster. Each category is coloured differently so that they can be easily distinguished. World maps were drawn including the known locations of the each of the observatories that detected a jerk in that cluster. The size and colour of the marker identifying the observatories is proportional to the regularity of the geomagnetic jerk detected there and corresponds to the cluster identified in its histogram plot, respectively. Demarcations of spatial areas that could possibly correspond to regional areas that show a similar temporal behaviour are draw in by hand.

It is important to note that the dates on which jerks have been calculated to have occurred is not always completely accurate, largely due to interference by external contributions of lines of maxima as they descend into the lower order dilations. Therefore, relative licence needs to be given in the interpretation of the following spatial maps.

4.3.1 1969

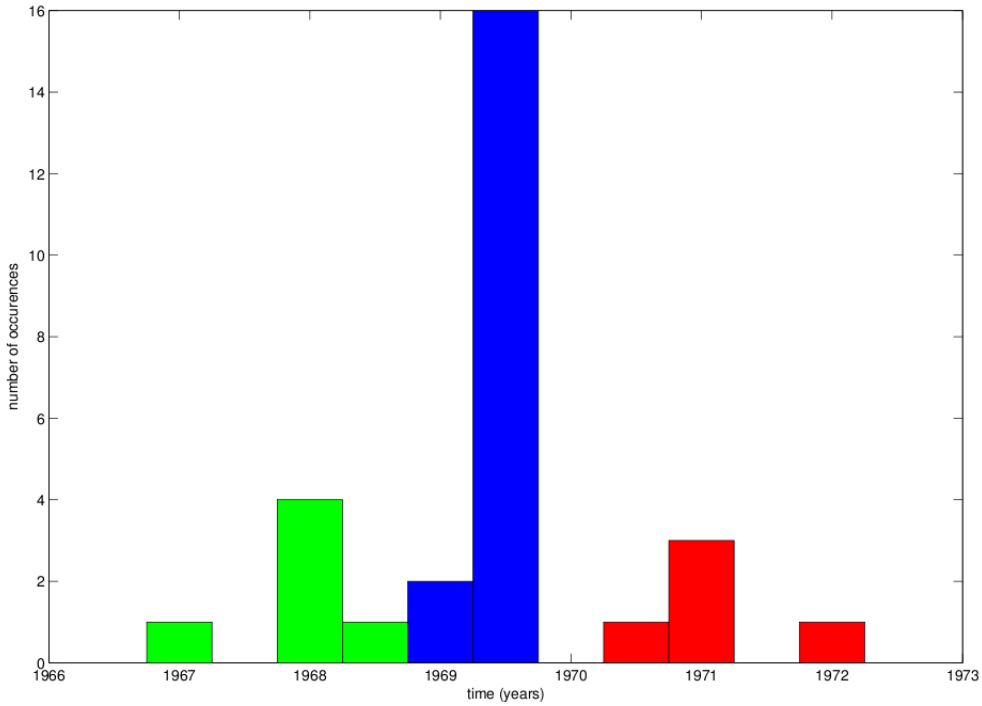

Figure 41: Histogram plot of the geomagnetic jerks associated with the 1969 cluster (Table 8), divided into three further clusters using the k-means clustering technique ($k = 3$). Each cluster is coloured differently so that they can be easily distinguished.

Given the distribution of the clusters associated with the 1969 geomagnetic jerk, spatial features are difficult to elucidate. A possible grouping of the jerks in the central region could be argued.

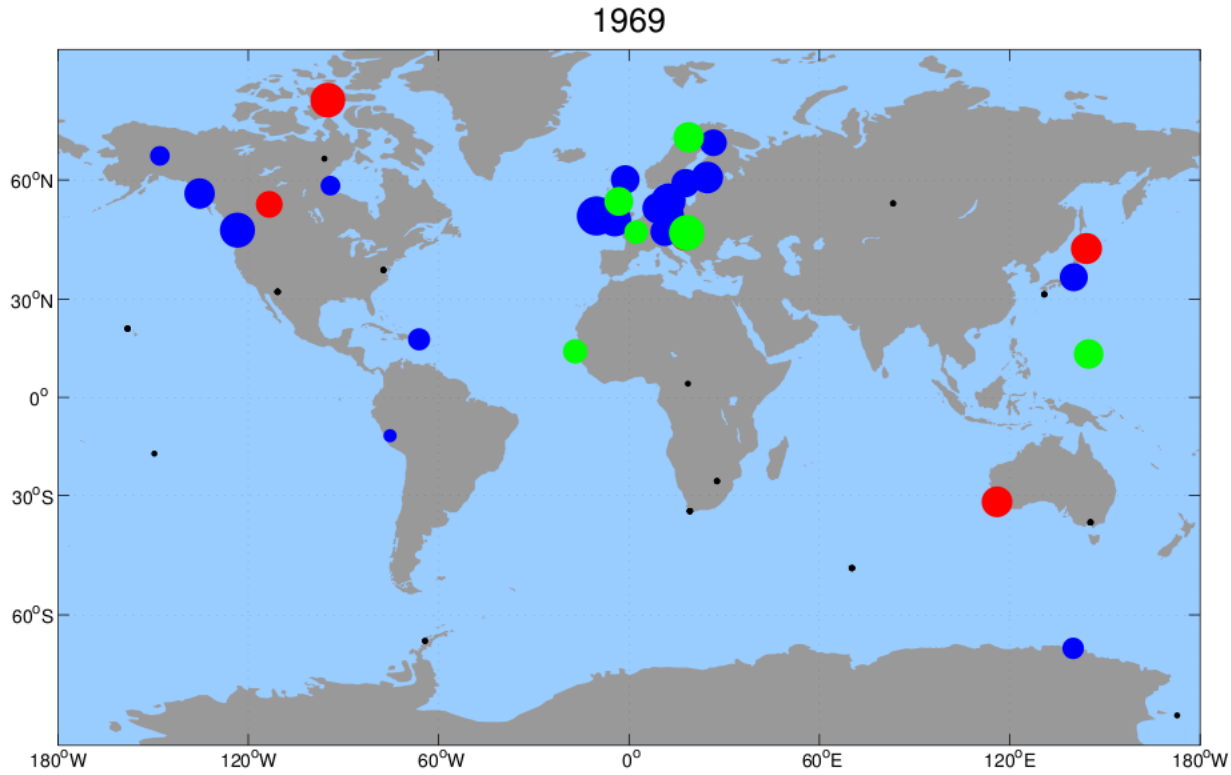

Figure 42: World map including the known locations of the each of the observatories that detected a jerk around 1969. The jerks are divided into three categories using k-means clustering (Figure 41). The size of the markers identifying the observatories is proportional to the regularity of the geomagnetic jerk detected there. The colour of each marker corresponds to the cluster to which that jerk belongs.

4.3.2 1978

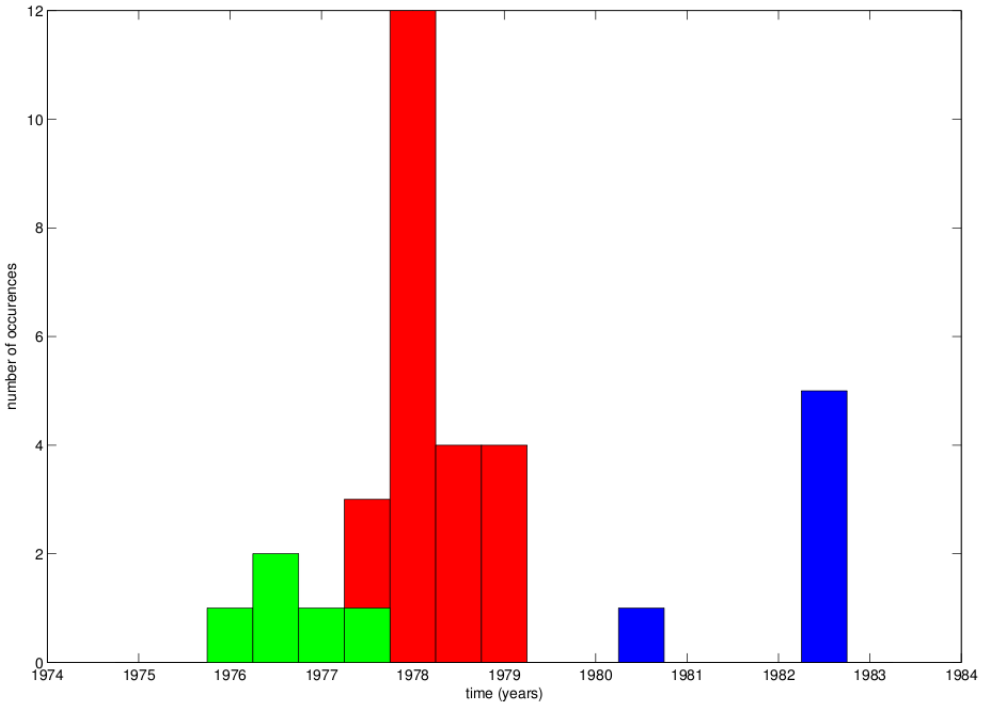

Figure 43: Histogram plot of the geomagnetic jerks associated with the 1978 cluster (Table 9), divided into three further clusters using the k-means clustering technique ($k = 3$). Each cluster is coloured differently so that they can be easily distinguished.

The spatial distribution shown in figure 44 displays a remarkable regional trend. If one considers the green markers as part of the red cluster, a northern-hemisphere, southern-hemisphere trend is apparent. The delay between jerks detected by these two regions is approximately 3 and half years. This result is consistent with findings of Alexandrescu et al. (1996).

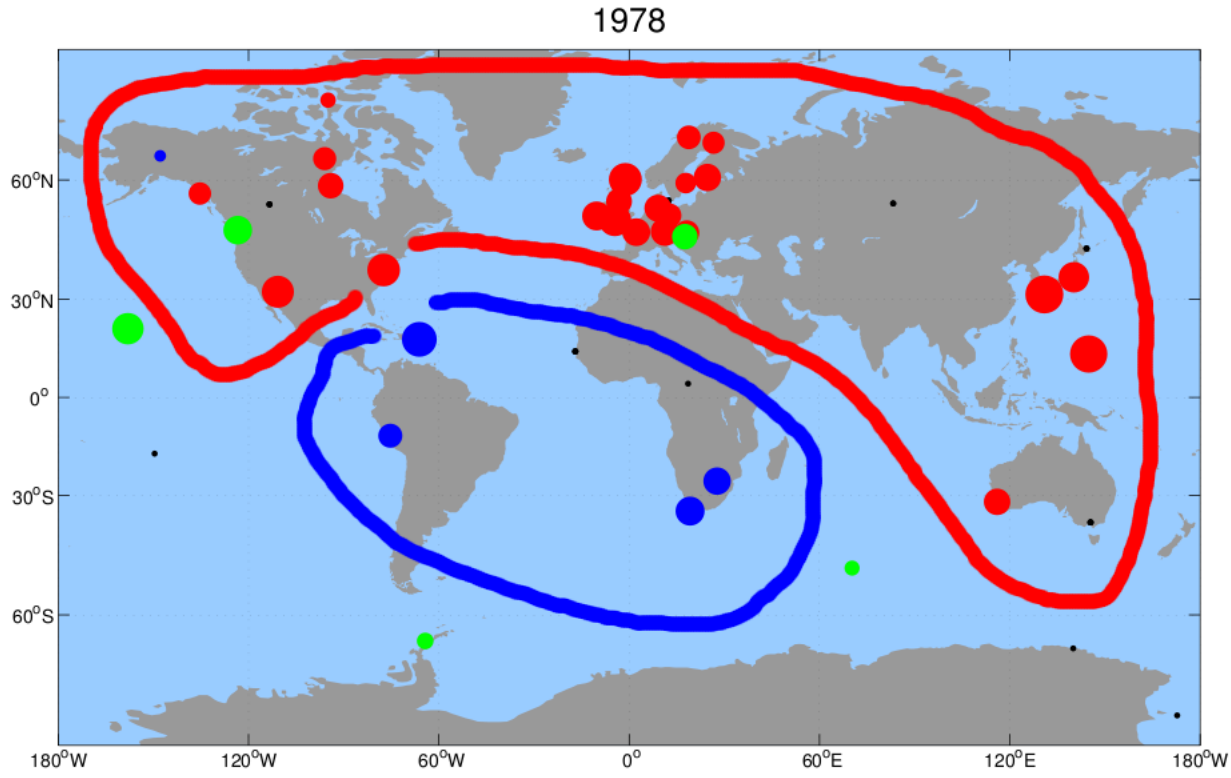

Figure 44: World map including the known locations of the each of the observatories that detected a jerk around 1978. The jerks are divided into three categories using k-means clustering (Figure 43). The size of the markers identifying the observatories is proportional to the regularity of the geomagnetic jerk detected there. The colour of each marker corresponds to the cluster to which that jerk belongs.

4.3.3 1990

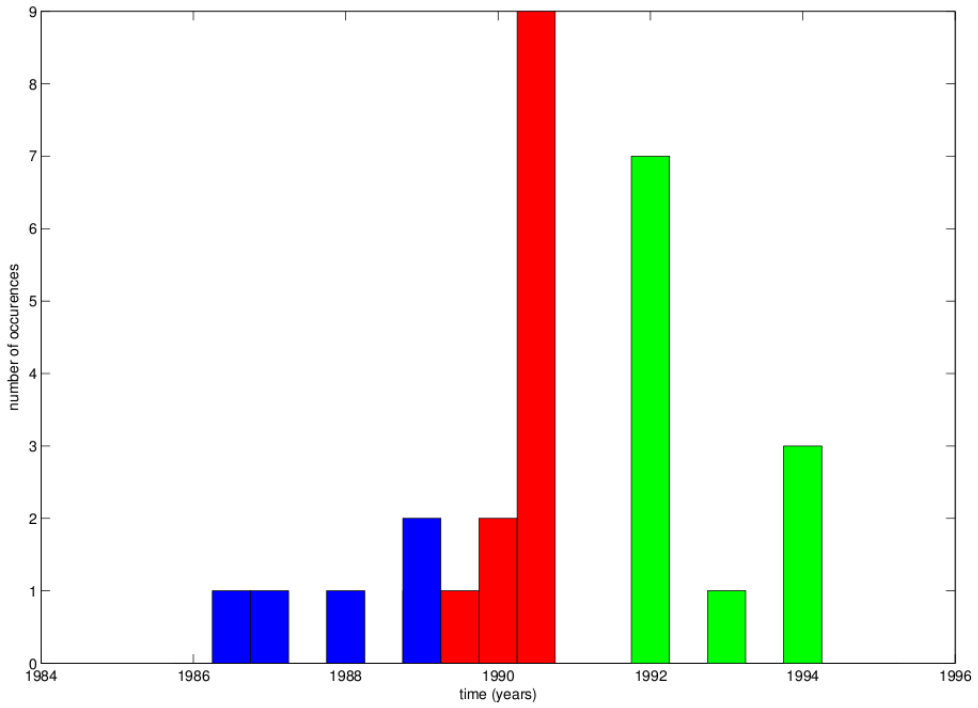

Figure 45: Histogram plot of the geomagnetic jerks associated with the 1990 cluster (Table 10), divided into three further clusters using the k-means clustering technique ($k = 3$). Each cluster is coloured differently so that they can be easily distinguished.

If one considers the blue markers (the "early arrivals") as very late arrivals from the 1990 jerk, an eastern-hemisphere, western-hemisphere trend is apparent (Figure 46). This implies the spatio-temporal trend of geomagnetic jerks to follow an antipodal region relationship.

Furthermore, the distinction of the blue markers as belonging to the 1978 jerk as very late arrivals falls in line with the north-south regional trend shown there.

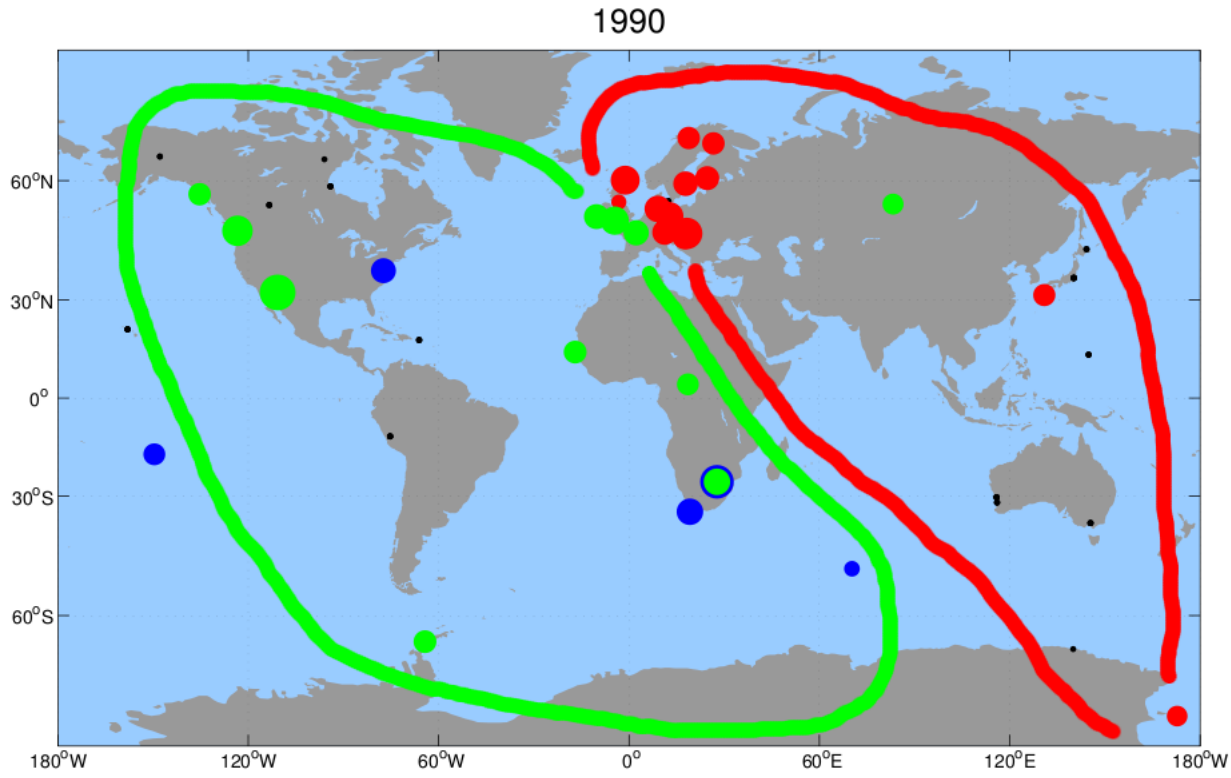

Figure 46: World map including the known locations of the each of the observatories that detected a jerk around 1990. The jerks are divided into three categories using k-means clustering (Figure 45). The size of the markers identifying the observatories is proportional to the regularity of the geomagnetic jerk detected there. The colour of each marker corresponds to the cluster to which that jerk belongs.

4.3.4 1998

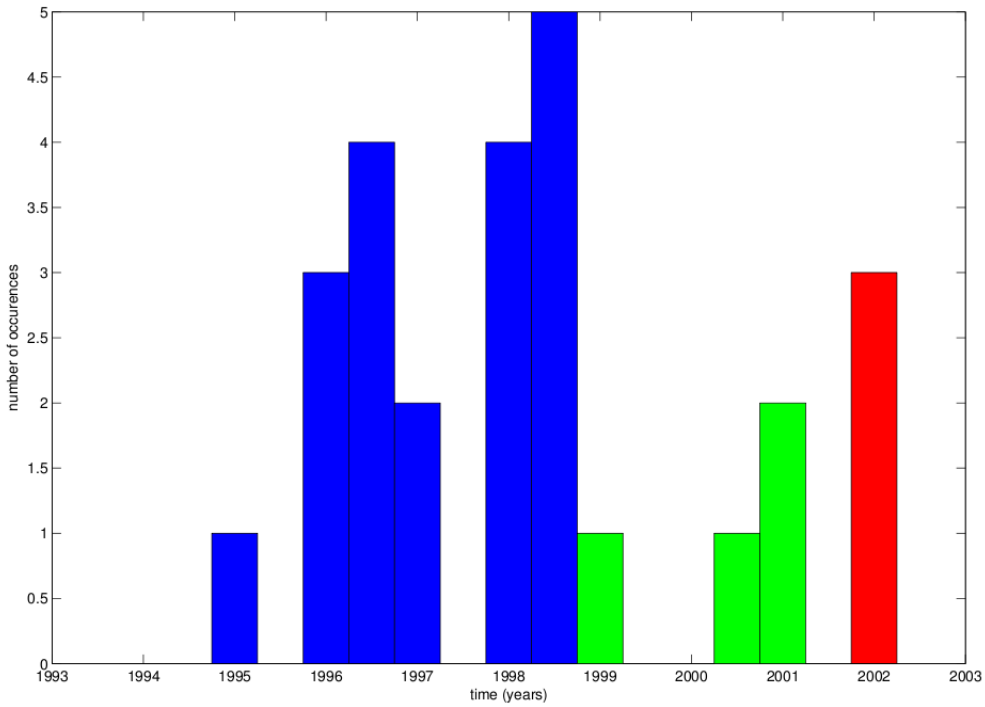

Figure 47: Histogram plot of the geomagnetic jerks associated with the 1998 cluster (Table 11), divided into three further clusters using the k-means clustering technique ($k = 3$). Each cluster is coloured differently so that they can be easily distinguished.

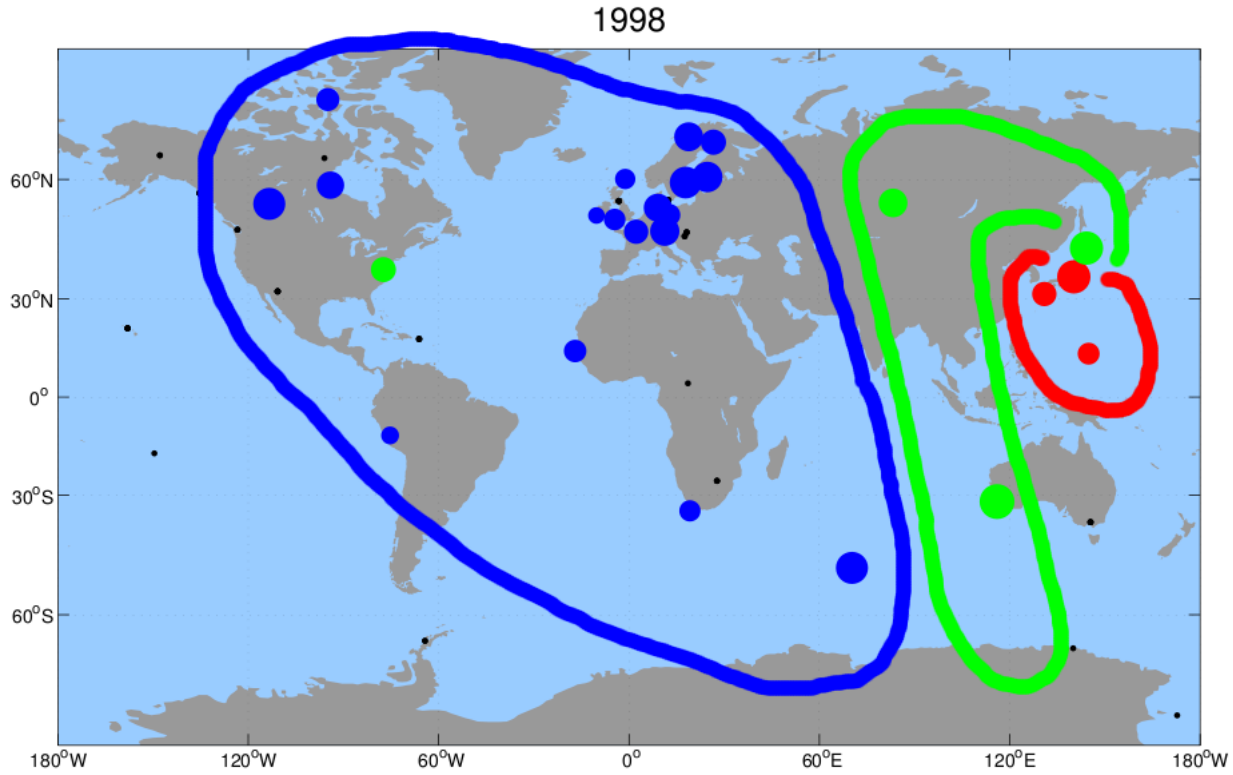

Figure 48: World map including the known locations of the each of the observatories that detected a jerk around 1998. The jerks are divided into three categories using k-means clustering (Figure 47). The size of the markers identifying the observatories is proportional to the regularity of the geomagnetic jerk detected there. The colour of each marker corresponds to the cluster to which that jerk belongs.

Figure 48 shows further surprising regional trends, with geomagnetic jerks first arriving between 1996 and 1998 in the western hemisphere and then arriving sequentially in the eastern hemisphere. The final region (in red) detecting the jerks to have arrived around 2002 (6 years later). Furthermore, after inspection, inspired by the regional trends elucidated, there is a hint of an energy packet in the wavelet transform of Honolulu Magnetic Observatory possibly corresponding to line of maxima around 2001, but this is distorted due to convolutional edge effects. Additions to Figure 48 are given in Figure 49, by means of dashed lines extending the red regions to include Honolulu magnetic observatory. From this addition, it is interesting to note that this region, last to detect the 1998 jerk, corresponds to the central Pacific “hot spots” - regions of up-welling “plumes” in the mantle.

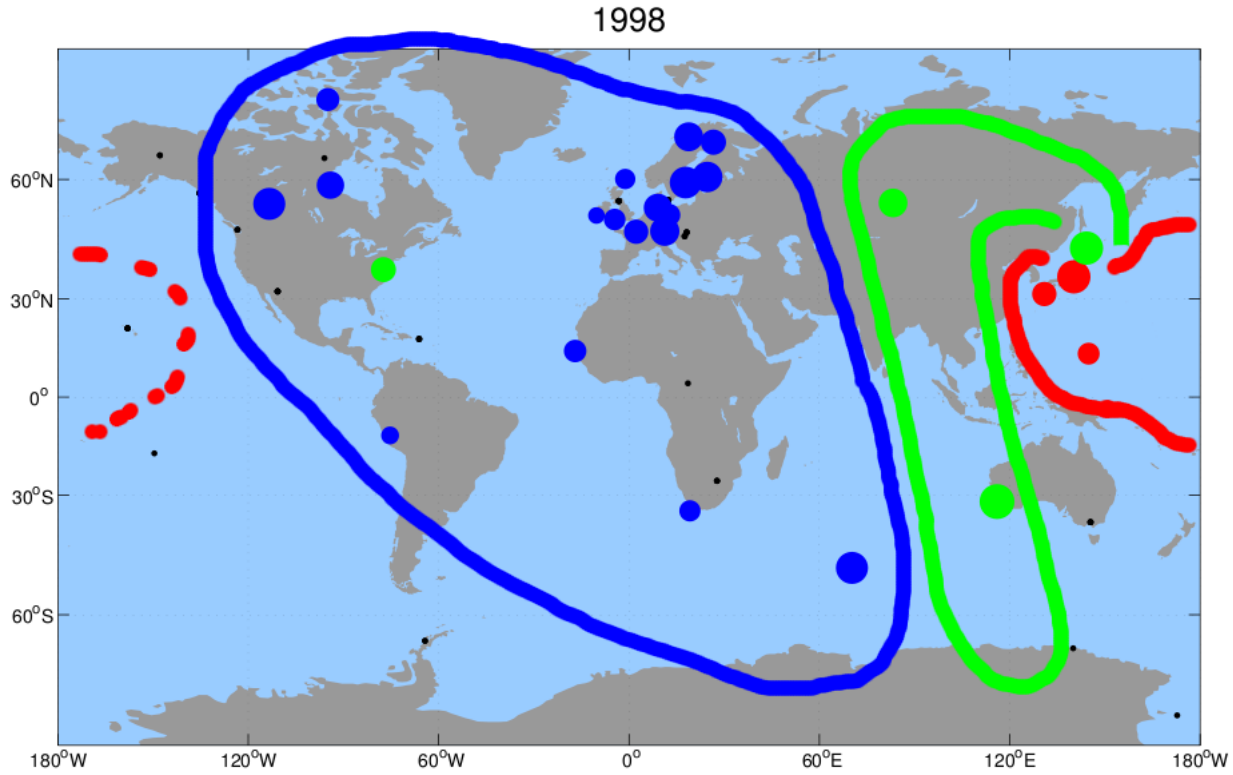

Figure 49: World map including the known locations of the each of the observatories that detected a jerk around 1998. The jerks are divided into three categories using k-means clustering (Figure 47). The size of the markers identifying the observatories is proportional to the regularity of the geomagnetic jerk detected there. The colour of each marker corresponds to the identifies the cluster to which that jerk belongs. The red region has been ammended to include Honolulu Magnetic Observatory. A small energy packet near the edge of the time series, could indicate a jerk centred around 2001.

From this spatio-temporal analysis, a regional trend of the arrival time of a geomagnetic jerk, detected at the surface of the earth, is evident. The relationship between regions has been found to possibly represent regions antipodal to each other (northern-southern or eastern-western hemispherical trends).

4.4 Origin of geomagnetic jerks

This section seeks to explore the origin of geomagnetic jerks using wavelet analysis. Up to this point, this study has only explored singularities starting at the time t_0, but this need not necessarily be the case. As mentioned in subsection 1.5, this study aims to investigate whether the nature of geomagnetic jerks are the result of:

- An instability starting at the time of the jerk ($t > t_0$)

- Some continuous oscillations ($\forall t$)
- A process ending at the time of the jerk ($t < t_0$).

Synthetic examples were first used to gain some insight into the wavelet analysis of singularities belonging to each of the above scenarios (see figure 50). In each case, a synthetic jerk-like singularity (occurring at $t_0 = 500$ with a regularity of 1.5) was analysed using the wavelet tool.

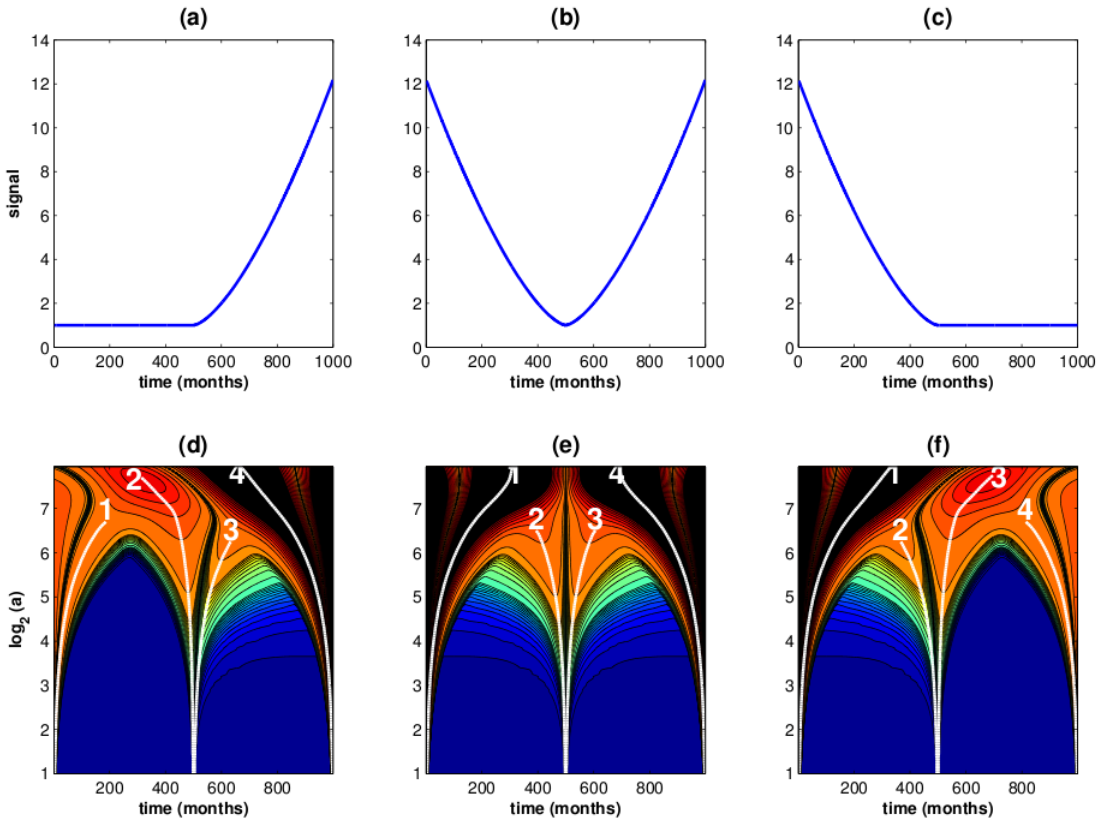

Figure 50: The synthetic signals, (a) to (c), containing a singularity occuring at $t_0 = 500$ with a of regularity 1.5 were analysed using the wavelet tool. The singularities in these synthetic signals each having differing natures: (a) an instability starting at the time of the jerk ($t > t_0$), (b) a continuous oscillation ($\forall t$) and (c) a process ending at the time of the jerk ($t < t_0$). The respective results of the wavelet analysis are given in (d) to (f). $t \in [0, 1000]$.

It is important to note that although the synthetic signals shown in figure 50, sub-plots (a) to (c), look very different and produce very different results from the wavelet tool, sub-plots (d) to (f), they all produce similar ridge functions and all recover the same regularity, namely 1.5 in this case.

It is also interesting to note the symmetry between the lines of maxima 2 and 3 in sub-plot (e) of figure 50. Recall in section 2.1.2, how it was observed that singularities of integer regularity have symmetric lines of maxima and lines

of maxima corresponding to singularities of non-integer regularity have non-symmetrical shape. As it turns out, the synthetic signals used in section 2.1.2 all used singularities starting at the time of the jerk ($t > t_0$), and this is not the case for singularities originating from continuous oscillations ($\forall t$).

From figure 50, it appears that the nature of each singularity carries a signature in the wavelet transform, as one heads into the higher order dilations: for an instability starting at the time of the jerk ($t > t_0$), the dominant line of maxima corresponding to the singularity deviates to the left (line 2 in sub-plot (d) of figure 50); for a continuous oscillations ($\forall t$), the lines of maxima remain symmetrical (lines 2 and 3 in sub-plot (e) of figure 50); and finally for a process ending at the time of the jerk ($t < t_0$), the dominant line of maxima corresponding to the singularity deviates to the right (line 3 in sub-plot (f) of figure 50). Hence, the nature of the singularities are encoded in their wavelet transforms, or more specifically in the way their corresponding lines of maxima deviate into the higher order dilations. This provided a possible guide for determining the nature of the geomagnetic jerks detected, and possibly the nature of the underlining process.

Further synthetic tests revealed that singularities near the edge of a time series were interfered with in the higher order dilations by convolutional edge effects. As a result, the deviations of the lines of maxima of these singularities were not clear.

Furthermore, subsequent tests on synthetic signals containing multiple singularities highlighted another problem with this guide. As mentioned in subsection 2.1.2, as one heads into higher order dilations, neighbouring singularities can interfere with each other masking these underlying deviations.

Various attempts to circumvent this were made, including: isolating individual singularities and analysing only an envelop of magnetic data around those singularities; looking at the phase when using the Hilbert transform of the third derivative of the Gaussian as the analysing wavelet; and using a causal analysing wavelet (Szu et al., 1992).

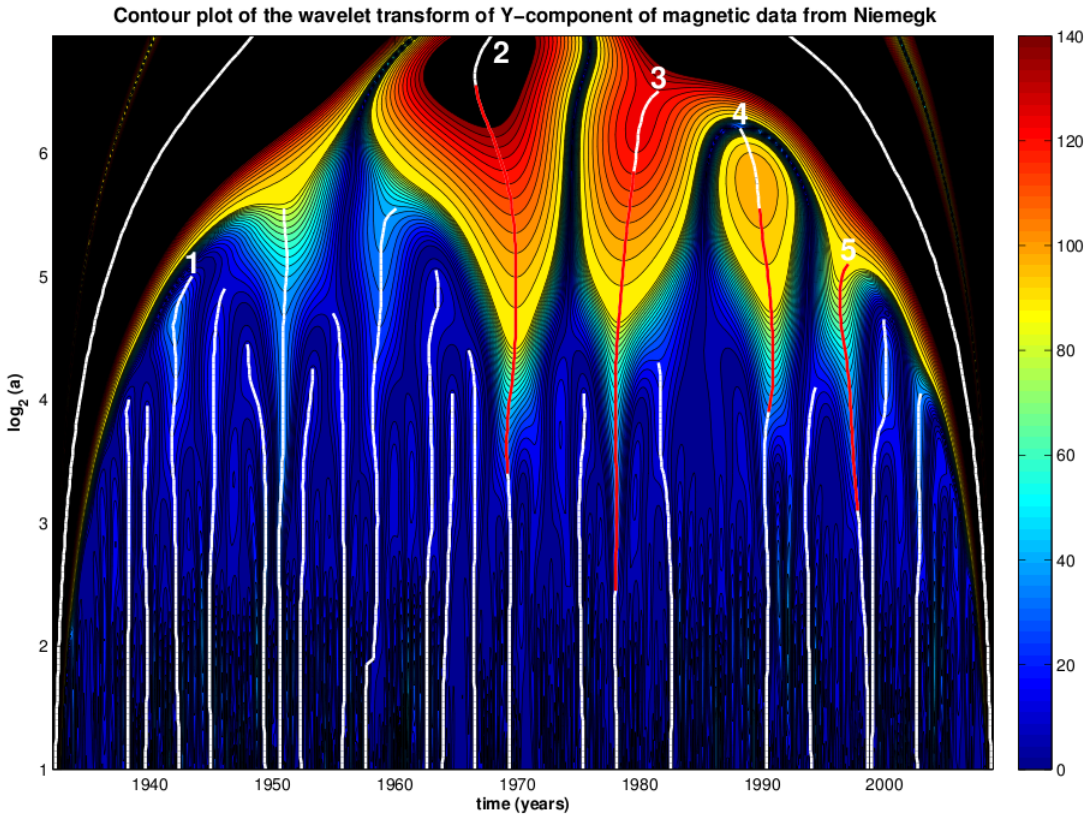

Figure 51: Contour plot of the modulus of the wavelet transform of the Y-component monthly mean data from the Niemegk magnetic observatory in Germany. The longest ($log_2(a) > 5$) lines of maxima of the modulus of the wavelet transform are plotted in white, but only the lines of maxima selected as corresponding to a possible geomagnetic jerk are numbered. The sections of the lines of maxima used to determine the regularities of the jerks are plotted in red. $t \in [1932, 2008]$.

Finally, a straightforward analysis of the way the lines of maxima of the jerks detected in this study deviate, was applied. The sections of the ridges used to determine the regularities of the jerks (e.g. the red lines in figure 51) were examined for deviations as they head into the higher order dilations.

For each observatory, jerk occurrences were plotted on a time-line: blue dots for events detected as starting at the time of the jerk, red dots for events ending at the time of the jerk and black for continuous oscillations (figure 52). In order to remove influence from convolutional edge effects, only lines of maxima that extend into the higher order dilations ($log_2(a) > 5.5$) were included. Figure 53, includes lines drawn to highlight the clusters of jerks with the same corresponding natures.

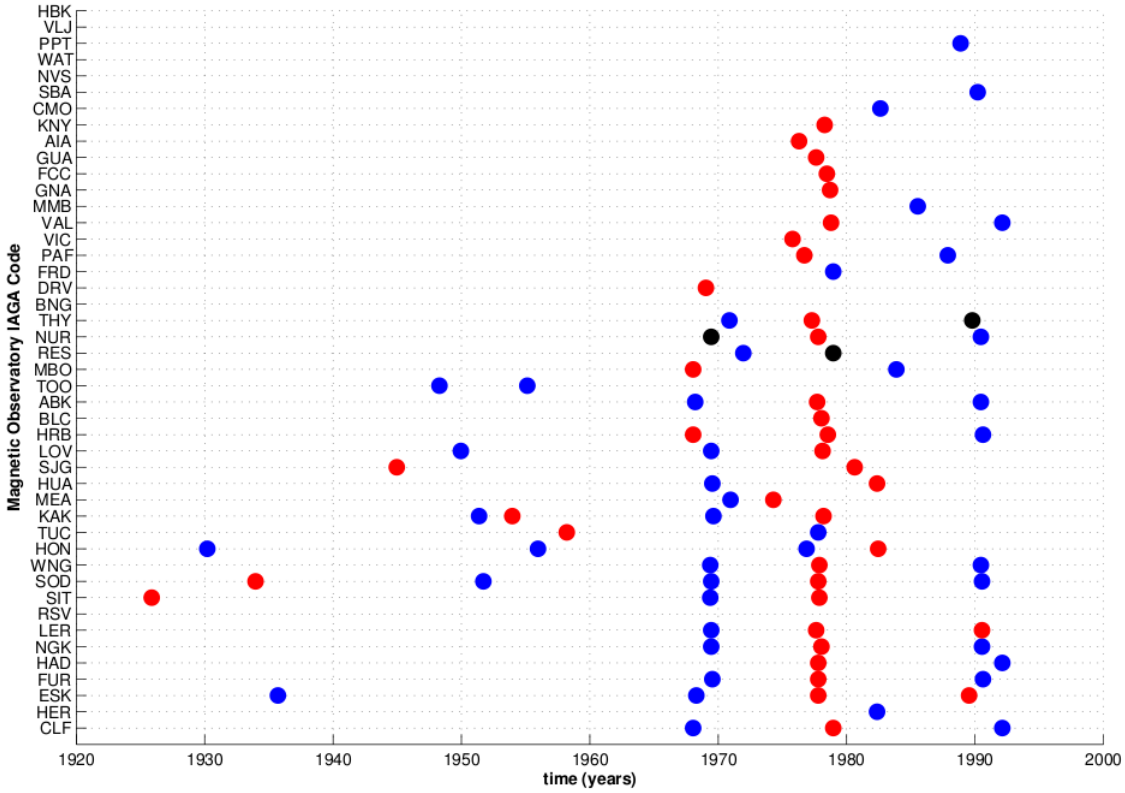

Figure 52: The occurrence of geomagnetic jerks detected in this study plotted on a time-line for each of the observatories analysed. Only jerks with corresponding lines of maxima that extend into the higher order dilations are plotted ($log_2(a) > 5.5$). The observatories are labelled according to their IAGI codes. Blue dots for events starting at the time of the jerk, red dots for events ending at the time of the jerk and black for continuous oscillations. $t \in [1920, 2000]$.

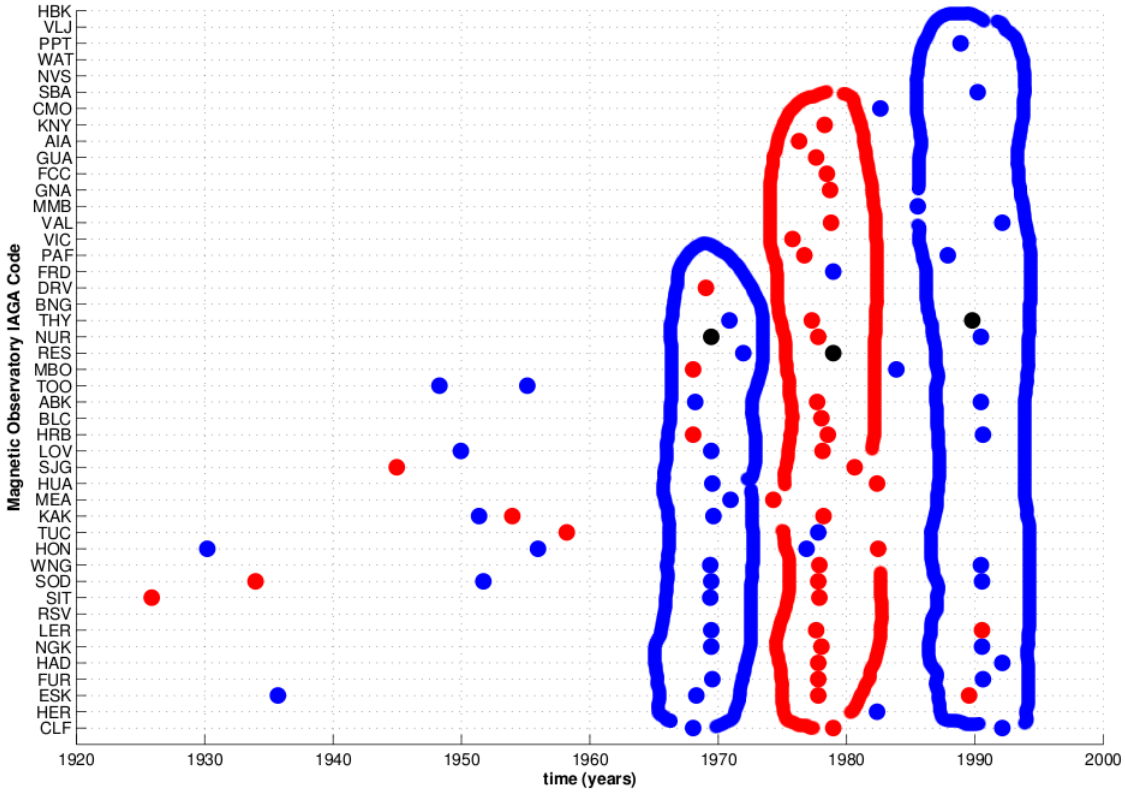

Figure 53: The occurrence of jerks detected in this study plotted on a time-line for each of the observatories analysed. Only jerks with corresponding lines of maxima that extend into the higher order dilations are plotted ($log_2(a) > 5.5$). The observatories are labelled according to their IAGI codes. Blue dots for events starting at the time of the jerk, red dots for events ending at the time of the jerk and black for continuous oscillations. Lines are drawn in to highlight the clusters of jerks with the same corresponding natures. $t \in [1920, 2000]$.

A startling pattern emerges that suggests that the 1969 jerk corresponded to a event starting at that time, the 1978 jerk corresponding to an event ending then, and lastly another event starting in 1990. This implies that the 1969 and 1978 jerks might be the result of a common phenomenon starting in 1969 and ending almost a decade later in 1978. This ties in nicely with the results obtained by Chulliat et al. (2010) of a common pulse between the 2003 and 2007 geomagnetic jerks. Could geomagnetic jerks a decade apart be coupled by a common cause? This is further discussed in the following chapter.

Chapter 5

Conclusions and Recommendations

One of the most remarkable features of this study is the treasure trove of information that can be explored in innocuous looking magnetic time series. Geomagnetic jerks have been detected to have occurred around the world in 1969, 1978, 1991 and 1999. Furthermore, geomagnetic jerks are also thought to have also occurred in 1901, 1913 and 1925, but due to the small number of observatories with long enough records to allow for detection during this period, their spatial extent, globally, is unclear. Two further geomagnetic jerks were found to have occurred around 1937 and 1952, but due to these events not being detected by all the observatories with records covering this period, these events might not be of the same global extent. The results of the geomagnetic jerks detected here and the phase jumps detected in the Chandler wobble are compared in subsection 4.2 and the remarkable coincidence highlighted.

Interestingly, the regularities recovered from the geomagnetic jerks detected are closer to 1.5 than 2. This matches the findings made by Alexandrescu et al. (1995, 1996) and again brings to light the question of whether geomagnetic jerks might be more singular than previously thought; but it is interesting to note that some results did recover regularities of approximately 2. Geomagnetic jerks are classically thought of as jumps in the second time derivative of a magnetic signal (i.e. $\alpha = 2$), but the results here indicate that they might result from jumps in the non-integer 1.5^{th} derivative of the signal.

That having been said, the process of recovering regularities is not perfect, given possible interference from external contributions, and therefore might not accurately represent the true regularities of geomagnetic jerks produced in the top of the core. Furthermore, generally only one line of maxima has been found associated with geomagnetic jerks detected in this study, compared to the two expected of singularities of regularity 1.5 found in synthetic experiments. It is important to further note that this study focuses its analysis on the Y-component of magnetic data, assuming jerks are polarized in this direction. This assumption might account for the lower than expected regularities, so future work of expanding the analysis to include the X and Z components could be extremely valuable and might shed some light

in this regard.

Alexandrescu et al. (1999) showed, using wavelet analysis, how singularities, like geomagnetic jerks, might distort as they diffuse through the conducting mantle. Could distortion through the conducting mantle account for the lower than expected regularities? Although, from those findings the distortion should increase the values of the recovered regularities of the singularities detected at the surface.

From the analysis using k-means clustering in subsection 4.3, an antipodal relationship between regions detecting geomagnetic jerks is evident. Both northern-southern and eastern-western hemispherical trends were found. Pinheiro and Jackson (2008) showed that these regional trends could be explained by the Earth's mantle acting as a conductor causing the gjerk time delays. Could these regional trends bring to light something about the origin of geomagnetic jerks? As mentioned in section 1, seismological waves have revealed a remarkable inner core anisotropy; significant differences between the west and east hemispheres of the Earth's inner core (e.g. Buffett, 2010; Bergman, 2010). And given the link postulated between inner core growth and mantle convection (e.g. Lister, 2008; Aubert et al., 2008), could this hemispherical asymmetry be linked to the regional trends displayed in the delayed detection of geomagnetic jerks at the Earth's surface?

Could these north-south and east-west regional trends be explained by geomagnetic jerks occurring in pairs? Chulliat et al. (2010) described how the 2003 and 2007 geomagnetic jerks detected in secular variation models using satellite data could be linked by a common acceleration pulse in the core. Furthermore, Olsen and Mandea (2007) discuss a "complete different pattern of the secular variation in different regions".

The results, outlined in subsection 4.4, suggest that the 1969 geomagnetic jerk originates from an event starting at that time and the 1978 jerk corresponding to an event ending at this time. This implies that these jerks were possibly linked by a common pulse and that jerks might occur in pairs: the first event indicating the start of the phenomena and the subsequent event indicating its end.

For future developments of this study, one of the most important components would be to include more observatory magnetic data. This would aid in detecting geomagnetic jerks near the end of the time series that get distorted due to convolutional edge effects. Note that the observatory magnetic data used in this study only extended to 2008, updating this to include up-to-date data would go a long way to better understanding geomagnetic jerks. Furthermore, better understanding of the nature of geomagnetic jerks would require more geomagnetic jerks with corresponding long lines of maxima which would only come about with longer time series (that extended way past recent jerks). Alternatively, using satellite virtual observatory data, as used by Olsen and Mandea, 2007, could go a long way to exploring the spatio-temporal behaviour because it provides much better global coverage of the Earth's magnetic field. Although studying geomagnetic jerks using satellite magnetic data provides much better global coverage (overcoming a major shortcoming using observatory magnetic data), observatory magnetic data plays an integral role as their long-term time

series enables the study of this geomagnetic data using wavelet analysis.

This study was restricted by only analysing the Y-component of observatory magnetic data and future work would need to adapt the Matlab wavelet tool outlined here and incorporate the X-component (as done by Alexandrescu et al., 1996) and possibly even the Z-component (as Olsen and Mandea, 2007 showed that the 2003 jerk was strongest in this direction).

Finally, to better explore the nature of geomagnetic jerks, further analysis techniques need to be explored. These methods need to account for both convolutional edge effects and possible interference effects between subsequent jerks.

Acknowledgements

I'd like to express my sincere gratitude to my supervisors Peter Kotze (South African National Space Agency); Gauthier Hulot and Dominique Gibert (Institut de Physique du Globe de Paris), for all the guidance and support received from them for the duration of this research.

!khure Africa project (www.!khure.org) is thanked for supplying funding for this thesis. !khure Africa is a South African–French flagship scientific cooperation programme in the geosciences. !khure Africa is also coordinated from the South African side through AEON (http://www.aeon.org.za) and, from the French side, through the IPGP (http://www.ipgp.fr) and University of Paris Diderot. !khure Africa is funded from the South African side through the National Research Foundation, NRF (http://www.nrf.ac.za/) and the Department of Science and Technology (http://www.dst.gov.za/).

The results presented in this thesis rely on data collected at magnetic observatories. We thank the national institutes that support them and INTERMAGNET for promoting high standards of magnetic observatory practice (www.intermagnet.org). A further thanks is made to the Bureau Central de Magnetisme Terrestre, BCMT (http://www.bcmt.fr/) for from use of data from the World Monthly Means Database (WMMD) project. This robustly processed monthly mean data was integral to this thesis.

References

Alexandrescu, M., Gibert, D., Hulot, G., Le Mouël, J.-L., and Saracco, G. (1995). Detection of geomagnetic jerks using wavelet analysis. *Journal of Geophysical Research*, 100:12557–12572.

Alexandrescu, M., Gibert, D., Hulot, G., Le Mouël, J.-L., and Saracco, G. (1996). Worldwide wavelet analysis of geomagnetic jerks. *Journal of Geophysical Research*, 101:21975–21994.

Alexandrescu, M. M., Gibert, D., Hulot, G., Le Mouël, J.-L., and Saracco, G. (1999). An estimate of average lower mantle conductivity by wavelet analysis of geomagnetic jerks. *Journal of Geophysical Research*, 104:17735–17745.

Alldredge, L. R. (1984). A discussion of impulses and jerks in the geomagnetic field. *Journal of Geophysical Research*, 89:4403–4412.

Anderson, D. L. and Hanks, T. C. (1972). Formation of the earth's core. *Nature*, 237:387–388.

Appell, D. (2012). A pressing matter. *Physics World*, 25/03:37–41.

Aubert, J., Amit, H., Hulot, G., and Olson, P. (2008). Thermochemical flows couple the earth's inner core growth to mantle heterogeneity. *Nature*, 454:758–760.

Backus, G. E. (1983). Application of mantle filter theory to the magnetic jerk of 1969. *Geophysical Journal of the Royal Astronomical Society*, 74:713–746.

Bellanger, E., Gibert, D., and le Mouël, J.-L. (2002). A geomagnetic triggering of chandler wobble phase jumps? *Geophysical Research Letters*, 29:1–4.

Bellanger, E., le Mouël, J.-L., Mandea, M., and Labrosse, S. (2001). Chandler wobble and geomagnetic jerks. *Physics of the Earth and Planetary Interiors*, 124:95–103.

Bergman, M. I. (2010). An inner core slip-sliding away. *Nature*, 466:697–698.

Biggin, A. J., Steinberger, B., Aubert, J., Suttie, N., Holme, R., Torsvik, T. H., van der Meer, D., and van Hinsbergen, D. J. J. (2012). Possible links between long-term geomagnetic variations and whole-mantle convection processes. *Nature Geoscience*, 5:526–531.

Biggin, A. J., Strik, G. H. M. A., and Langereis, C. G. (2008). Evidence for a very-long term trend in geomagnetic secular variation. *Nature Geoscience*, 1:395–398.

Bishop, C. M. (1995). *Neural Networks for Pattern Recognition.* Oxford University Press, Oxford, England.

Bloxham, J. and Jackson, A. (1991). Fluid flow near the surface of the earth's outer core. *Reviews of Geophysics*, 29:97–120.

Bloxham, J., Zatman, S., and Dumberry, M. (2002). The origin of geomagnetic jerks. *Nature*, 420:65–68.

Buffett, B. A. (2010). The enigmatic inner core. *Science*, 328:982–983.

Chambodut, A. and Mandea, M. (2005). Evidence for geomagnetic jerks in comprehensive models. *Earth Planets Space*, 57:139–149.

Chulliat, A. and Telali, K. (2007). World monthly means database project. *Publications of the Institute of Geophysics, Polish Academy of Sciences*, 398:268–274.

Chulliat, A., Thébault, E., and Hulot, G. (2010). Core field acceleration pulse as a common cause of the 2003 and 2007 geomagnetic jerks. *Geophysical Research Letters*, 37:1–5.

Courtillot, V., Ducruix, J., and le Mouël, J.-L. (1978). Sur une accélération récente de la variation séculaire du champ magnétique terrestre. *Comptes rendus des séances de l' Académie des Sciences*, 287:1095–1098.

Courtillot, V., Gallet, Y., le Mouël, J.-L., Fluteau, F., and Genevey, A. (2007). Are there connections between the earth's magnetic field and climate. *Earth and Planetary Science Letters*, 253:328–339.

Courtillot, V., Hulot, G., Alexandrescu, M., le Mouël, J.-L., and Kirschvink, J. L. (1997). Sensitivity and evolution of sea-turtle magnetoreception: observations, modelling and constraints from geomagnetic secular variation. *Terra Nova*, 9:203–207.

Courtillot, V. and le Mouël, J.-L. (1984). Geomagnetic secular variation impulses. *Nature*, 311:709–716.

Davies, G. F. (1999). *Dynamic Earth*. Cambridge University Press.

Fournier, A., Hulot, G., Jault, D., Kuang, W., Tangborn, A., Gillet, N., Canet, E., Aubert, J., and Lhuillier, F. (2010). An introduction to data assimilation and predictability in geomagnetism. *Space Science Reviews*, 155:247–291.

Gao, R. X. and Yan, R. (2011). *Wavelets*. Springer.

Gibert, D., Holschneider, M., and le Mouël, J.-L. (1998). Wavelet analysis of the chandler wobble. *Journal of Geophysical Research*, 103:27069–27089.

Gibert, D. and le Mouël, J.-L. (2008). Inversion of polar motion data: Chandler wobble, phase jumps, and geomagnetic jerks. *Journal of Geophysical Research*, 113:10405. doi:http://dx.doi.org/10.1029/2008JB005700.

Gire, C. and le Mouël, J.-L. (1986). Flow in the fluid core and earth's rotation. *In Earth rotation: Solved and unsolved problems*, A88:241–258.

Glatzmaier, G. A., Coe, R. S., Hongre, L., and Roberts, P. H. (1999). The role of the earth's mantle in controlling the frequency of geomagnetic reversals. *Nature*, 401:885–890.

Gubbins, D. (2008). Geomagnetic reversals. *Nature*, 452:165–167.

Helffrich, G. and Satoshima (2010). Out corecompositional stratification from observed core wave speed profiles. *Nature*, 468:807–810.

Holme, R. and de Viron, O. (2005). Geomagnetic jerks and a high-resolution length-of-day profile for core studies. *Geophysical Journal International*, 160:435–439.

Hulot, G., Finlay, C. C., Constable, C. G., Olsen, N., and Mandea, M. (2010). The magnetic field of planet earth. *Space Science Reviews*, 152:159–222.

INTERMAGNET (2010). Magnetic observatories (map). URL: http://www.intermagnet.org/Imomap_e.php.

Le Huy, M., Alexandrescu, M., Hulot, G., and le Mouël, J.-L. (1998). On the characteristics of successive geomagnetic jerks. *Earth Planets Space*, 50:723–732.

Lehmann, I. (1936). P'. *Publications du Bureau Central SÃ©ismologique International*, 14:87–115.

Lehmann, I. (1987). Seismology in the days of old. *Eos, Transactions, American Geophysical Union*, 68:33.

Lister, J. (2008). Structuring the inner core. *Nature*, 454:701–702.

Lohmann, K. J., Putman, N. F., and Lohmann, C. M. F. (2008). Geomagnetic imprinting: A unifying hypothesis of long-distance natal homing in salmon and sea turtles. *Proceedings of the National Academy of Sciences*, 105:19096–19101.

Love, J. (2008). Magnetic monitoring of earth and space. *Physics Today*, 61:31–37. doi:http://dx.doi.org/10.1063/1.2883907.

Macmillan, S. (1996). A geomagnetic jerk for the early 1990's. *Earth and Planetary Science Letters*, 137:189–192.

Malin, S. R. C. and Hodder, B. M. (1982). Was the 1970 geomagnetic jerk of internal or external origin? *Nature*, 296:726–728.

Mallat, S. (2009). *A wavelet tour of signal processing: The sparse way*. Elsevier.

Mallat, S. and Hwang, W. L. (1992). Singularity detection and processing with wavelets. *IEEE Transactions on Information Theory*, 38:617–643.

Mandea, M., Bellanger, E., and le Mouël, J.-L. (2000). A geomagnetic jerk for the end of the 20th century? *Earth and Planetary Science Letters*, 183:369–373.

Mandea, M., Holme, R., Pais, A., Pinheiro, K., Jackson, A., and Verbanac, G. (2010). Geomagnetic jerks: Rapid core field variations and core dynamics. *Space Science Review*, 155:147–175.

Olsen, N., Hulot, G., and Sabaka, T. J. (2007). *The Present Field*, volume 5 of *Treatise on Geophysics*. Elsevier.

Olsen, N. and Mandea, M. (2007). Investigation of a secular variation impulse using satellite data: The 2003 geomagnetic jerk. *Earth and Planetary Science Letters*, 255:94–105.

Olson, P. (2007). *Treatise on Geophysics: Core Dynamics*, volume 8. Elsevier, Amsterdam.

Pinheiro, K. and Jackson, A. (2008). Can a 1-d mantle electrical conductivity model generate magnetic jerk differential time delays? *Geophysical Journal International*, 173:781–792.

Pinheiro, K., Jackson, A., and Finlay, C. C. (2011). Measurements and uncertainties of the occurrence time of the 1969, 1978, 1991, and 1999 geomagnetic jerks. *G3*, 12:1–32.

Pozzo, M., Davies, C., Gubbins, D., and Alfé, D. (2012). Thermal and electrical conductivity of iron at earth's core conditions. *Nature*, 485:355–358.

Riewe, F. (1997). Machanics with fractional derivatives. *Physical Review*, 55:3581–3592.

Rotanova, N. M., Bondar, T. N., and Kovalevskaya, E. V. (2003). Wavelet analysis of secular geomagnetic variations. *Russian Journal of Earth Sciences*, 5:375–383.

Schiermeier, Q. (2005). Solar wind hammers the ozone layer. Nature News. doi:`http://dx.doi.org/10.1038/news050228-12`.

Shankland, T. J., Peyronneau, J., and Poirier, J.-P. (1993). Electrical conductivity of the earth's lower mantle. *Nature*, 366:453–455.

Silva, L. and Hulot, G. (2012). Investigating the 2003 geomagnetic jerk by simultaneous inversion of the secular variation and acceleration for both the core flow and its acceleration. *Physics of The Earth and Planetary Interiors*, 198:28–50.

Song, X. and Richards, P. G. (1996). Seismological evidence for differential rotation of the earth's inner core. *Nature*, 382:221–224.

Szu, H. H., Telfer, B. A., and Lohmann, A. W. (1992). Causal analytical wavelet transform. *Optical Engineering*, 31:1825–1829.

Tanaka, A., Okubo, Y., and Matsubayashi, O. (1999). Curie point depth based on spectrum analysis of the magnetic anomaly data in east and southeast asia. *Tectonophysics*, 306:461–470. doi:http://dx.doi.org/10.1016/S0040-1951(99)00072-4.

Tarduno, J. A., Cottrell, R. D., and Smirnov, A. V. (2006). The paleomagnetism of single silicate crystals: Recording geomagnetic field strength during mixed polarity intervals, superchrons, and inner core growth. *Reviews of Geophysics*, 44:31.

Tarduno, J. A., Cottrell, R. D., Watkeys, M. K., Hofmann, A., Doubrovine, P. V., Mamajek, E. E., Liu, D., Sibeck, D. G., Neukirch, L. P., and Usui, Y. (2010). Geodynamo, solar wind, and magnetopause 3.4 to 3.45 billion years ago. *Science*, 327:1238–1240.

Wahr, J. M. (1988). The earth's rotation. *Annual Review of Earth and Planetary Sciences*, 16:231–249.

Wardinski, I., Holme, R., Asaria, S., and Mandea, M. (2008). The 2003 geomagnetic jerk and its relation to the core surface flows. *Earth and Planetary Science Letters*, 267:468–481.

Wookey, J. and Helffrich, G. (2008). Inner-core shear wave anisotropy and texture from an observation of pkjkp waves. *Nature*, 454:873–876.

Zatman, S. and Bloxham, J. (1997). Torsional oscillations and the magnetic field within the earth's core. *Nature*, 388:760–763.

Appendices

Appendix A

Matlab Code (*.m denotes a matlab file)

A.1 transform.m

```
function output = transform (input_signal, starting_dilation, dilation_orders, dilation_resolution)

signal_length = length (input_signal);
num_convolutions = dilation_orders*dilation_resolution;
dilations = starting_dilation*(2.^((0:num_convolutions)./dilation_resolution));
output = zeros (num_convolutions, signal_length);

for i = 0:num_convolutions,
    wavelet = gaussian3 (dilations(i+1));
    output (i+1,:) = abs(convolution (input_signal, wavelet));
end
```

A.2 gaussian3.m

```
function output = gaussian3 (dilation)
length = round(4.77*dilation);
a = (-length:length)/dilation;
argument = -a.*a/2.;
output = -a.*(a.*a-3).*exp(argument)/dilation;
```

A.3 convolution.m

```
function output = convolution (signal, wavelet)
output = conv (signal, wavelet, 'same');
```

A.4 lom.m

```
function [peaks_per_dilation, num_lines, lines, lines_of_maxima] = lom (output)

% ---- Setting global variables ----
global signal_length;
global num_convolutions;
global trimX;

for i = 1:num_convolutions+1,
    [~, time] = findpeaks (output(i, trimX:signal_length-trimX),'MINPEAKHEIGHT', 5e-4);
    peaks_per_dilation (i) = {time+trimX-1}; %#ok<AGROW>
end
starting_dilation = 80;
num_lines = numel(cell2mat(peaks_per_dilation (starting_dilation)));
starting_peaks = cell2mat(peaks_per_dilation (starting_dilation));
lines = cell (1,num_lines);
for i = 1:num_lines,
    the_line = zeros (1,starting_dilation);
    current_time = starting_peaks (i);
    the_line (starting_dilation) = current_time;
    for j = starting_dilation-(1:(starting_dilation-1)),
        next_dilation_row = cell2mat(peaks_per_dilation (j));
        [distance closest] = min(abs(next_dilation_row - current_time));
        if distance < 10
            the_line (j) = next_dilation_row(closest);
            %plot ([date(current_time) date(next_dilation_row(closest))], [log2(dilations(j+1)) log2(dilations(j))], 'w-')
            current_time = next_dilation_row(closest);
        else
            break;
        end
    end
    current_time = starting_peaks (i);
    for k = starting_dilation:(num_convolutions+1),
        next_dilation_row = cell2mat(peaks_per_dilation (k));
        [distance closest] = min(abs(next_dilation_row - current_time));
        if distance < 10
            the_line (k) = next_dilation_row(closest);
            %plot ([date(current_time) date(next_dilation_row(closest))], [log2(dilations(k-1)) log2(dilations(k))], 'w-')
            current_time = next_dilation_row(closest);
        else
            break;
        end
    end
    lines (i) = {the_line};
end
lines_of_maxima = zeros(num_convolutions+1, num_lines);
for m = 1:num_lines,
    l = numel (cell2mat (lines (m)));
    lines_of_maxima (1:l,m) = cell2mat (lines (m));
end
```

A.5 loglog_plot_all.m

```
function loglog_plot_all (output, dilations, num_lines, lines_of_maxima)
format short;
for i = 1:num_lines,
    line = lines_of_maxima (:,i);
    line = line (line~=0);
    line_length = length(line);
    subplot (round(sqrt(num_lines)),ceil(sqrt(num_lines)),i);
    log2W = zeros (line_length, 1);
    for j = 1:line_length,
        log2W (j) = log2(output (j,line(j)));
    end
    plot (log2(dilations(1:line_length)),log2W,  'LineWidth', 1.4);
    set(gca,'FontSize',8)
    axis ([1 7 0 8]);
    set(gca,'XTick', 1:7)
    if line_length > 101
        grad = mean (gradient (log2W(51:100), 0.05));
    else
        grad = mean (gradient (log2W(41:end), 0.05));
    end
    format short g
    text(2, 5, num2str(grad), 'FontSize', 8);
    title(num2str(i),'FontWeight','Bold','FontSize',10)
end
```

A.6 runall.m

```
% !!!!!!!!!!   Wavelet Analysis Tool - Tjaart de Wit   !!!!!!!!!!!

% ---- Setting global variables ----
global signal_length;
global num_convolutions;
global trimX;
global trimY;
trimX=1;
trimY=0;
starting_dilation = 2;
dilation_orders = 6;
dilation_resolution = 20;
min_data = 120;
num_convolutions = dilation_orders*dilation_resolution;
dilations = starting_dilation*(2.^((0:num_convolutions)./dilation_resolution));

% code = ['CLF'; 'NGK'; 'SOD'; 'ESK'; 'WNG'; 'RSV'; 'FUR'; 'LER'; 'HAD'; 'SIT'];
% code = ['AAA';'AAE';'ABG';'ABK';'ABN';'AIA';'AMS';'API';'AQU';'ASC';'ASP';'BDV';'BEL';'BFE';'BLC';'BMT';'BNG';'BOU';'BOX';'BRW';'BSL';'CBB';'CLF';
%         'CMO';'CNB';'CTA';'CZT';'DLR';'DOB';'DOU';'DRV';'EBR';'ESK';'EYR';'FCC';'FRD';'FRN';'FUR';'GCK';'GDH';'GNA';'GUA';'GUI';'GWC';'GZH';'HAD';
%         'HBK';'HER';'HLP';'HON';'HRB';'HRN';'HUA';'IQA';'IRT';'KAK';'KDU';'KNY';'KOU';'LER';'LOV';'LRM';'LVV';'LZH';'MAB';'MAW';'MBO';'MCQ';'MEA';
%         'MMB';'NAQ';'NCK';'NEW';'NGK';'NUR';'NVS';'OTT';'PAF';'PBQ';'PHU';'PPT';'PSM';'PST';'QSB';'RES';'RSV';'SBA';'SFS';'SHU';'SIT';'SJG';'SOD';
%         'SPT';'STJ';'SUA';'TAM';'TAN';'TEN';'TEO';'THL';'THY';'TOO';'TRO';'TRW';'TSU';'TUC';'UPS';'VAL';'VIC';'VLJ';'VSS';'WAT';'WNG';'YKC'];

code = ['CLF';'HER';'ESK';'FUR';'HAD';'NGK';'LER';'RSV';'SIT';'SOD';'WNG';'HON';'TUC';'KAK';'MEA';'HUA';'SJG';'LOV';'RSV';'HRB';
 'BLC';'ABK';'TOO';'MBO';'RES';'NUR';'THY';'BNG';'DRV';'FRD';'PAF';'VIC';'VAL';'MMB';'GNA';'FCC';'GUA';'AIA';'KNY';'CMO';
 'SBA';'NVS';'WAT';'PPT';'VLJ';'HBK'];

for obsloop = 1:numel(code(:,1))

    % ---- Loading BCMT Monthly Mean Data ----
    [date X Y Z L station] = read_observatory (code(obsloop,:));
    stations {obsloop} = station; %#ok<SAGROW>

    if length(Y) > min_data

        % ---- Cleaning data ----
        [Y L date] = clean (Y, L, date);           % Only cleaning the Y and L data variables - if need to use X or Z, add here
        signal_length = length(Y);

        % ---- Setting signal ----
        input_signal = Y;

        % ---- Performing Continuous Wavelet Transform ----
        output = transform (input_signal, starting_dilation, dilation_orders, dilation_resolution);

        % ---- Surface plot ----
        % surface_plot (output, date, dilations);   %For visualization purposes

        % ---- Contour plot with colours ----
        contour_plot (output, date, dilations, [0:1:19 20:10:140], station.name);

        % ---- Determining the lines of maxima ----
        [peaks_per_dilation, num_lines, lines, lines_of_maxima] = lom (output);

        % ---- Selecting lines of maxima ----
        [line_select, regularity, line_segment] = select_jerks (output, num_lines, lines);

        if line_select ~= 0
            % ---- Plotting lines of maxima on figure ----
            lom_plot (num_lines, lines_of_maxima, date, dilations, line_select);
        end

        % ---- Saving plot to pdf file ----
        set(gcf,'PaperOrientation','landscape');
        set(gcf,'PaperPosition', [1 1 28 19]);
        print(gcf, '-dpdf', ['plots/', station.code, ' - countourlines.pdf']);

        if line_select ~= 0
            % ---- Log-log plots of selected ridge functions displaying jerk trend ----
            clf;
            loglog_plot (output, dilations, lines_of_maxima, line_select, regularity, line_segment)

            % ---- Print the current figure ----
            set(gcf,'PaperOrientation','landscape');
            set(gcf,'PaperPosition', [1 1 28 19]);
            print(gcf, '-dpdf', ['plots/', station.code, ' - loglog.pdf']);
            clf;
        end

        % ---- Log-log plots of all the ridge functions ----
        loglog_plot_all (output, dilations, num_lines, lines_of_maxima)

        % ---- Print the current figure ----
        set(gcf,'PaperOrientation','landscape');
        set(gcf,'PaperPosition', [1 1 28 19]);
        print(gcf, '-dpdf', ['plots/', station.code, ' - loglogall.pdf']);
        clf;

        if line_select ~= 0
            % ---- Determining jerk date
            jerk_date = dating_jerks (lines_of_maxima, line_select, date);
        end

        % ---- Store results for observatory in structure ----
        data {obsloop} = struct ('output', output, 'date', date, 'linesofmaxima', lines_of_maxima, 'lineselect', line_select, 'regularity', regularity, '
            jerkdate', jerk_date, 'linesegment', line_segment); %#ok<SAGROW>
    end
end
```

A.7 read_observatory.m

```
function [date, X, Y, Z, L, station] = read_observatory (code)
num_headers = 1;
header = 1;
station = struct ('name', '', 'code', 'Null', 'latitude', 0, 'longitude', 0, 'elavation', 0);
file = fopen(['bcmt/', code, '_mm.dat'],'r');
while header == 1
    temp = fgetl(file);
    if ~isempty (strfind (temp, 'TIME'))
        header = 0;
    end
    switch num_headers,
        case 1,
            textline = regexp (temp, '\w*', 'match');
            temp = [];
            for i = 3:(numel(textline))
                temp = [temp cell2mat(textline(i)) ' ']; %#ok<AGROW>
            end
            station.name = temp(1:(end-1));
        case 2,
           textline = regexp (temp, '\w*', 'match');
           station.code = cell2mat(textline (3));
       case 3,
           textline = regexp (temp, '\s*', 'split');
           station.latitude = str2double(textline (5));
       case 4,
           textline = regexp (temp, '\s*', 'split');
           station.longitude = str2double(textline (5));
       case 5,
           textline = regexp (temp, '\s*', 'split');
           station.elevation = str2double(textline (4));
   end
   num_headers = num_headers + 1;
end
fclose(file);
[date X Y Z L , ~, ~] = textread(['bcmt/', code, '_mm.dat'],'%8.3f %d %d %d %d %d %d','headerlines', (num_headers-1));
```

A.8 clean.m

```
function [clean_signal clean_L clean_date] = clean (signal, L, date)
preadjustments = signal;
presignal_length = length(preadjustments);
adjustment = 0;
for i = 1:presignal_length,
    if L(i) == 9 && date(i) == round(date(i))
        adjustment = adjustment + preadjustments (i);
    end
    if preadjustments(i) ~= 999999
        preadjustments(i) = preadjustments(i) + adjustment;
    end
end
postadjustments = preadjustments;
postL = L;
postdate = date;
thecounter = 0;
for i = 1:presignal_length,
    if L(i) == 9 && date(i) == round(date(i))
        postadjustments = [postadjustments(1:i-1-thecounter); postadjustments(i+1-thecounter:end)];
        postL = [postL(1:i-1-thecounter); postL(i+1-thecounter:end)];
        postdate = [postdate(1:i-1-thecounter); postdate(i+1-thecounter:end)];
        thecounter = thecounter + 1;
    end
end
errors = postadjustments;
signal_length = length(postadjustments);
L = postL;
date = postdate;
deleted = 0;
delete_end = 0;
for i = 1:signal_length,
    if errors(i)==999999 || L (i) == 9
        if i ~= 1 && i~= signal_length
            still_error = 1;
            counter = 1;
            errors (i) = NaN;
            L(i) = 2;
            while still_error && (i+counter)~=signal_length
                if errors (i + counter) == 999999 || L (i+counter) == 9
                    errors (i + counter) = NaN;
                    L(i+counter) = 2;
                    counter = counter + 1;
                else
                    %t = i-1:i+counter;
                    l = counter+2;
                    f = [];
                    if (errors(i-1) ~= errors (i+counter))
                        f = errors(i-1):((errors(i+counter)-errors(i-1))/(l-1)):errors(i+counter);
                    else
                        for k = 1:l
                            f(k) = errors (i-1); %#ok<AGROW>
                        end
                    end
                    errors (i-1:i+counter) = round(f+[0, randi(10,1,l-2)-5, 0]);
                    break;
                end
            end
            if (i+counter)==signal_length
                delete_end = 1;
                clean_signal = errors(1+deleted:i-1);
                clean_L = L(1+deleted:i-1);
                clean_date = date (1+deleted:i-1);
            end
        end
        if i == 1
            still_error = 1;
            counter = 1;
            deleted = 1;
            while still_error
                if errors (i + counter) == 999999 || L (i+counter) == 9
                    counter = counter + 1;
                    deleted = counter;
                else
                    i = deleted; %#ok<FXSET>
                    break;
                end
            end
        end
    end
end
if ~delete_end
    clean_signal = errors(1+deleted:end);
    clean_L = L(1+deleted:end);
    clean_date = date (1+deleted:end);
end
```

A.9 lom_plot.m

```
function lom_plot (num_lines, lines_of_maxima, date, dilations, line_select)
% ---- Setting global variables ----
global num_convolutions;
line_num = 1;
for i = 1:num_lines,
    for j = 1:num_convolutions,
        if lines_of_maxima (j+1,i) ~= 0
            plot ([date(lines_of_maxima(j,i)) date(lines_of_maxima(j+1,i))], [log2(dilations(j)) log2(dilations(j+1))], 'w-', 'LineWidth', 1.8)
            hold on;
            if j == num_convolutions && ~isempty(find(i == line_select, 1))
                text(date(lines_of_maxima(j,i)+8),log2(dilations(j-2))-0.03,num2str(line_num),'FontWeight','Bold','FontSize',18, 'Color', [1 1 1], '
                    HorizontalAlignment', 'right');
                line_num = line_num+1;
            end
        else
            if ~isempty(find(i == line_select, 1))
                text(date(lines_of_maxima(j,i)+0),log2(dilations(j-2))+0.1,num2str(line_num),'FontWeight','Bold','FontSize',18, 'Color', [1 1 1], '
                    VerticalAlignment', 'baseline', 'HorizontalAlignment', 'center');
                line_num = line_num+1;
            end
            break;
        end
    end
end
```

A.10 select_jerks.m

```
function [line_select, regularity, line_segment] = select_jerks (output, num_lines, lines)
gradient_threshold = 0.19;
breaking_from_average_threshold = 0.9;
upper_bound = 2;
lower_bound = 0.79;
minimum_segment = 20;
num_jerks = 0;
line_select = 0;
line_segment = [];
regularity = 0;
for i = 1:num_lines,
    line_length = numel(cell2mat(lines(i)));
    line = cell2mat(lines (i));
    log2W = zeros (line_length, 1);
    for j = 1:line_length,
        if line (j) == 0
            break;
        end
        log2W (j) = log2(output (j,line(j)));
    end
    grad = gradient (log2W, 0.05);
    counter = 1;
    grad_line_segment = 0;
    has_started = 0;
    start = line_length;
    breaking_from_average = 0;
    for j = line_length-(1:(line_length-1)),
        if abs(grad (j) - grad (j+1)) < gradient_threshold && ~breaking_from_average
            grad_line_segment (counter) = grad (j+1); %#ok<AGROW>
            average_so_far = mean(grad_line_segment);
            if abs(grad (j+1) - average_so_far) > breaking_from_average_threshold && counter > 10
                breaking_from_average = 1;
            end
            if ~has_started
                has_started = 1;
                start = j;
            end
            counter = counter + 1;
        else
            if counter > minimum_segment
                grad = grad_line_segment;
                break;
            end
            counter = 1;
            grad_line_segment = 0;
            breaking_from_average = 0;
            has_started = 0;
        end
    end
    if numel(grad_line_segment) < minimum_segment
        if line_length > 101
            for j = line_length-(1:(line_length-90)),
                if grad(j)<0
                    neg = j+1;
                else
                    neg = j;
                    break;
                end
            end
            grad = gradient (log2W(61:neg), 0.05);
            start = neg;
            counter = neg - 61;
        elseif line_length > 40
            grad = gradient (log2W(41:end), 0.05);
            start = length(log2W);
            counter = length(log2W)-41;
        else
            grad = gradient (log2W, 0.05);
        end
    end
    regs (i) = mean(grad); %#ok<AGROW>
    if regs (i) >= lower_bound && regs (i) <= upper_bound
        num_jerks = num_jerks + 1;
        line_segment(num_jerks,:) = [start-counter+2 start]; %#ok<AGROW>
        regularity (num_jerks) = regs(i); %#ok<AGROW>
        line_select (num_jerks) = i; %#ok<AGROW>
    end
end
```

A.11 loglog_plot.m

```
function loglog_plot (output, dilations, lines_of_maxima, line_select, regularity, line_segment)
num_selected_lines = numel(line_select);
format short;
for i = 1:num_selected_lines,
    line = lines_of_maxima (:,line_select(i));
    line = line (line~=0);
    line_length = length(line);
    subplot (round(sqrt(num_selected_lines)),ceil(sqrt(num_selected_lines)),i);
    log2W = zeros (line_length, 1);
    for j = 1:line_length,
        log2W (j) = log2(output (j,line(j)));
    end
    plot (log2(dilations(1:line_length)),log2W, 'b', 'LineWidth', 1.8);
    hold on;
    plot (log2(dilations(line_segment(i,1):line_segment(i,2))),log2W(line_segment(i,1):line_segment(i,2)), 'r',  'LineWidth', 1.8);
    axis ([1 7 0 8]);
    xlabel('log_2(a)');
    ylabel('log_2(|Wf(t,a)|)');
    set(gca,'XTick', 1:7)
    set(gca,'FontSize',10)
    text(3.9, 5, num2str(regularity(i)));
    title(num2str(i),'FontWeight','Bold', 'FontSize',18)
end
```

A.12 dating_jerks.m

```
function [jerk_date] = dating_jerks (lines_of_maxima, line_select, date)
dating_dilation = 30;
num_selected_lines = numel(line_select);
for i = 1:num_selected_lines,
    the_jerk_line = lines_of_maxima(:,line_select(i));
    jerk_date (i) = date(the_jerk_line(dating_dilation)); %#ok<AGROW>
end
```

Appendix B

Wavelet analysis results

The following appendix includes the remaining results of the wavelet analysis from the magnetic observatories. For each observatory, a contour plot of the modulus of the wavelet transform of the Y-component monthly mean data from the respective observatory is given. The longest ($log_2(a) > 5$) lines of maxima of the modulus of the wavelet transform are plotted in white, but only the lines of maxima selected as corresponding to a possible geomagnetic jerk are numbered.

A further plot is given displaying the log-log plots of the ridge functions corresponding to the lines of maxima indentified as possibly indicating a geomagnetic jerk and numbered in the previous figure. The recovered regularities calculated from the gradient of the linear portions of the ridge functions highlighted in red are labelled. $a\varepsilon[2^0, 2^7]$

B.1 Abisko (ABK)

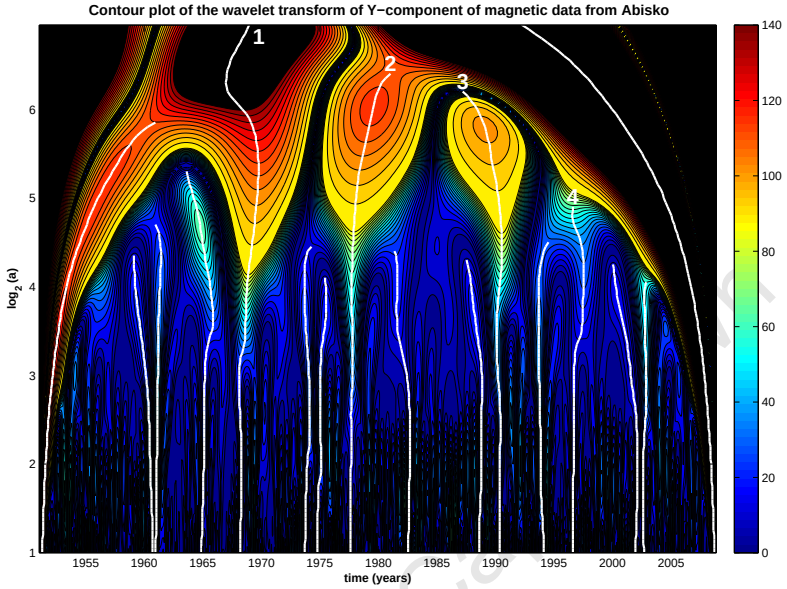

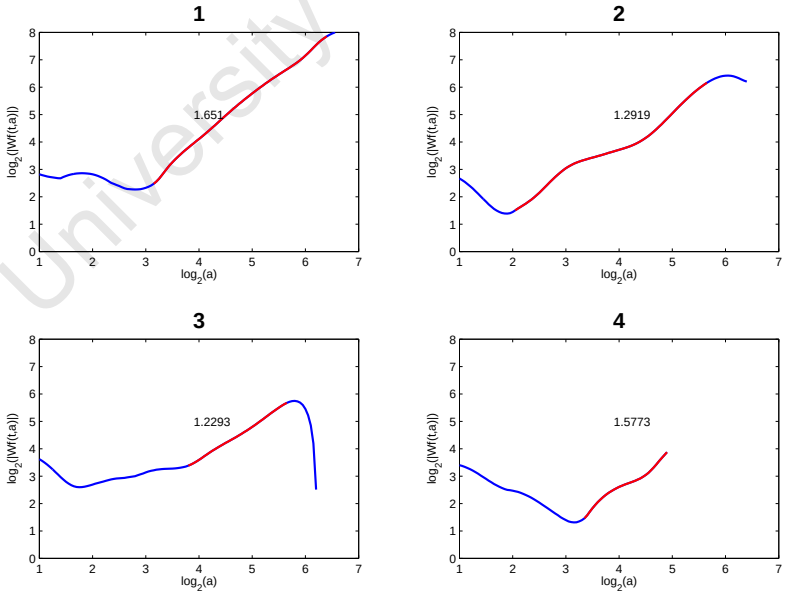

B.2 Argentine Islands (AIA)

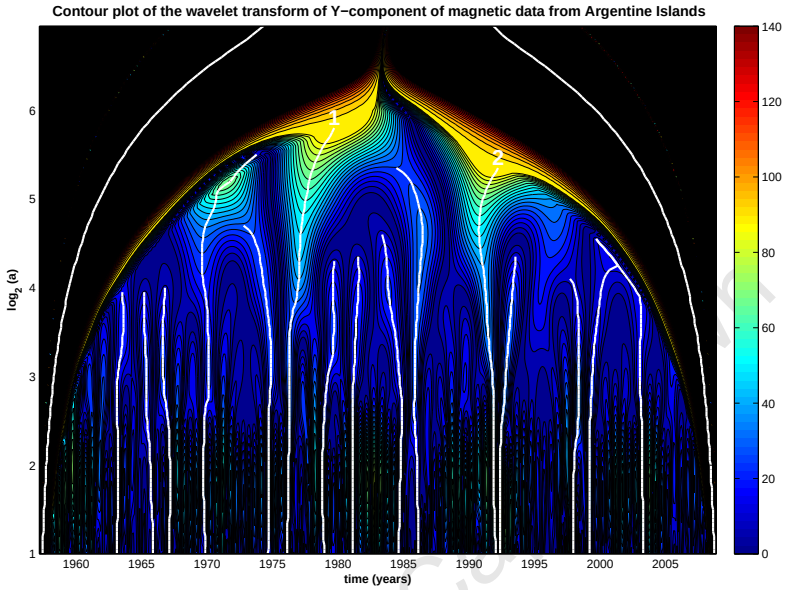

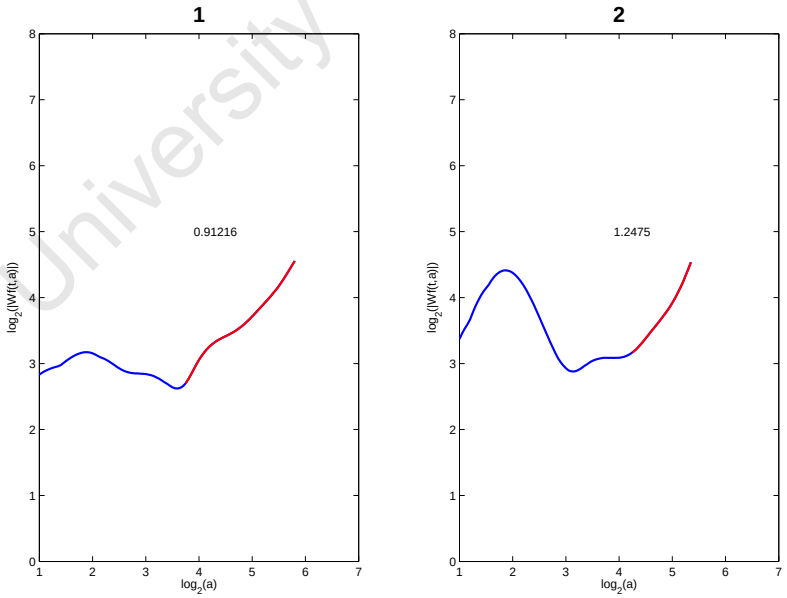

B.3 Baker Lake (BLC)

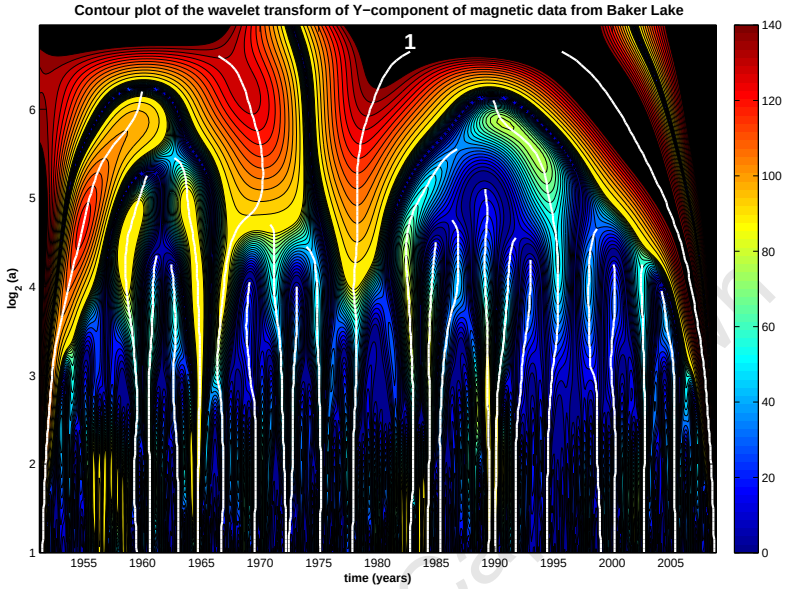

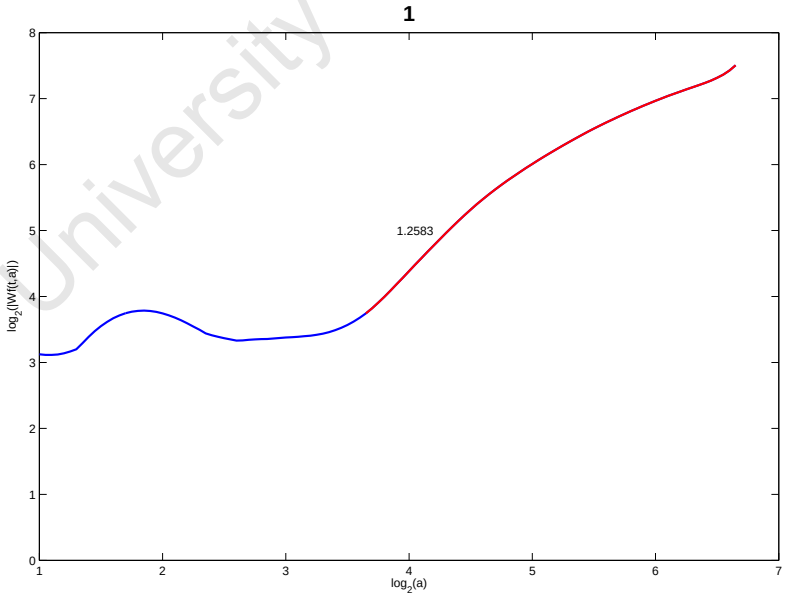

B.4 Bangui (BNG)

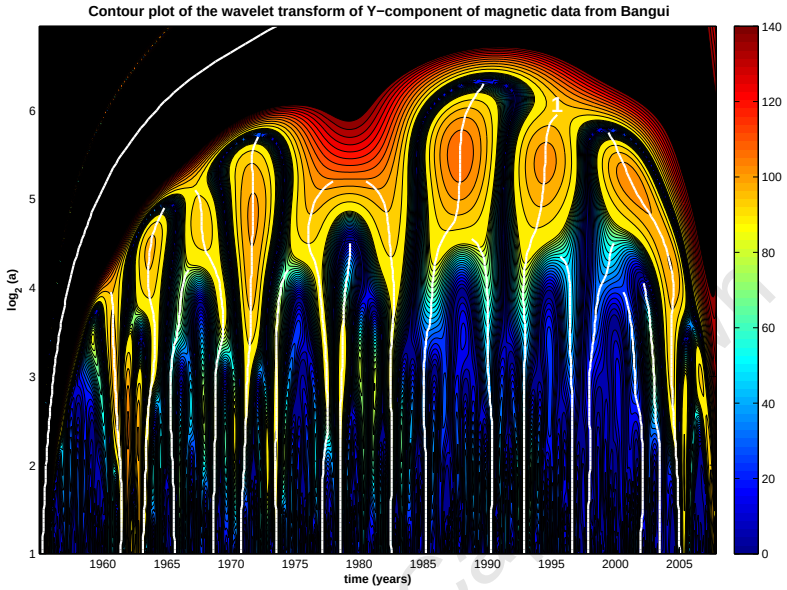

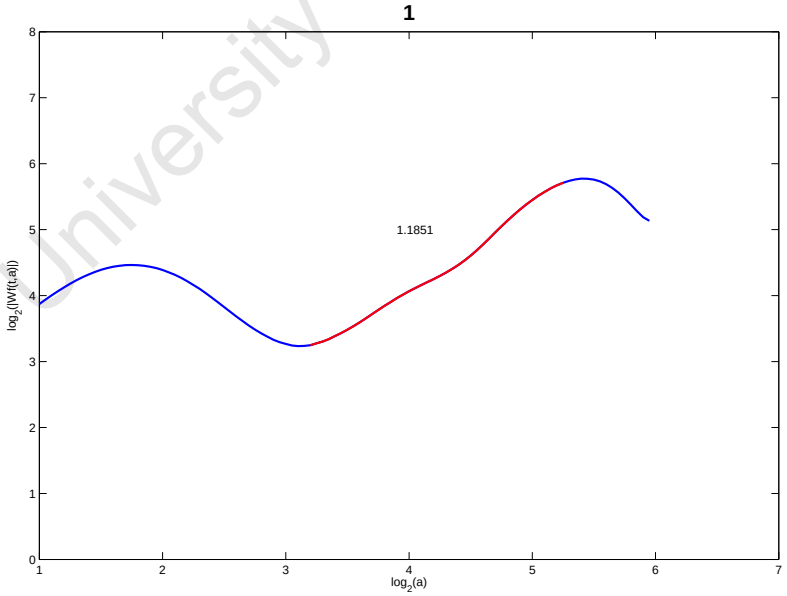

B.5 Chambon-la-Forêt

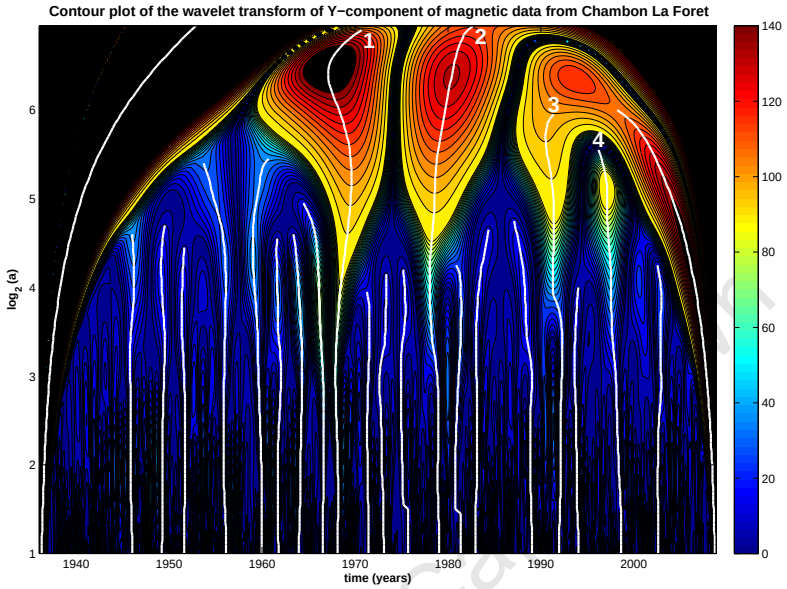

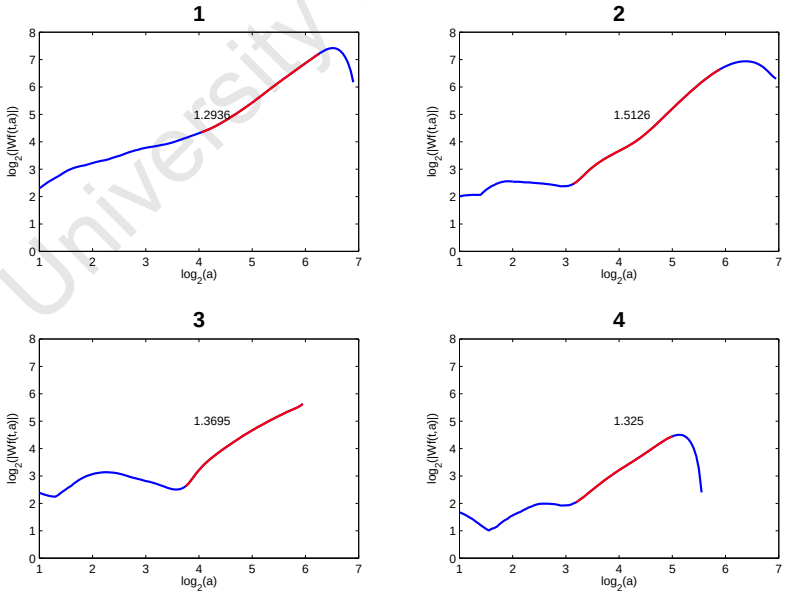

B.6 College (CMO)

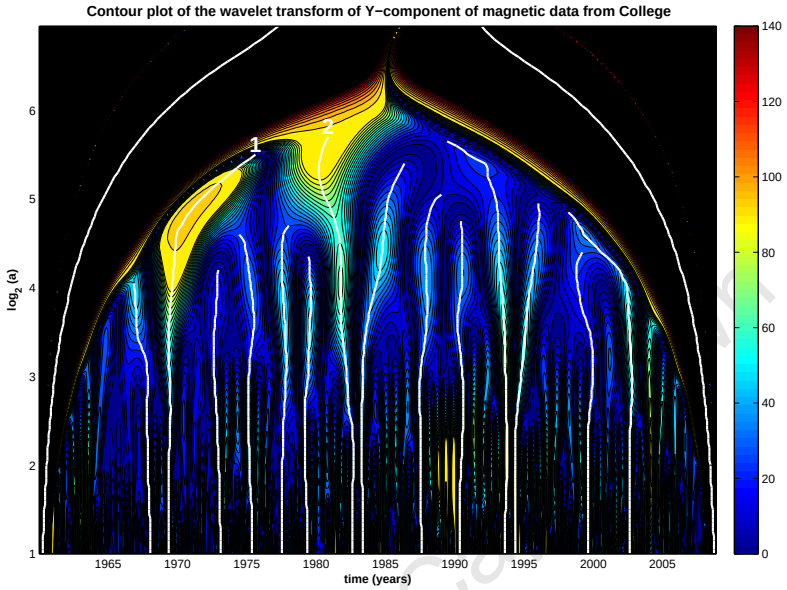

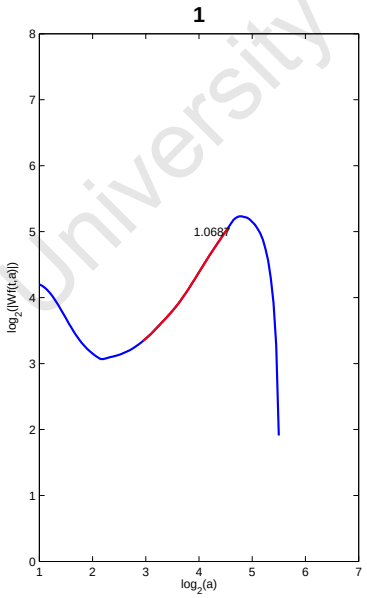

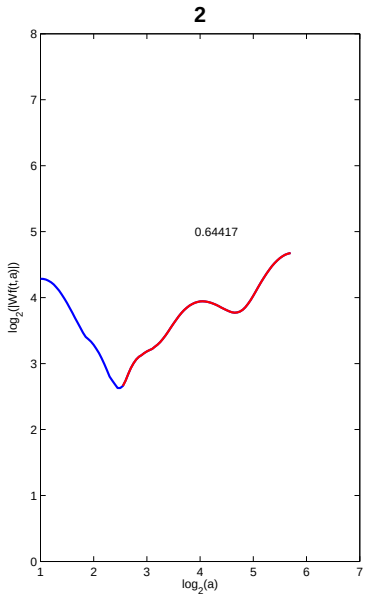

B.7 Dumont d'Urville (DRV)

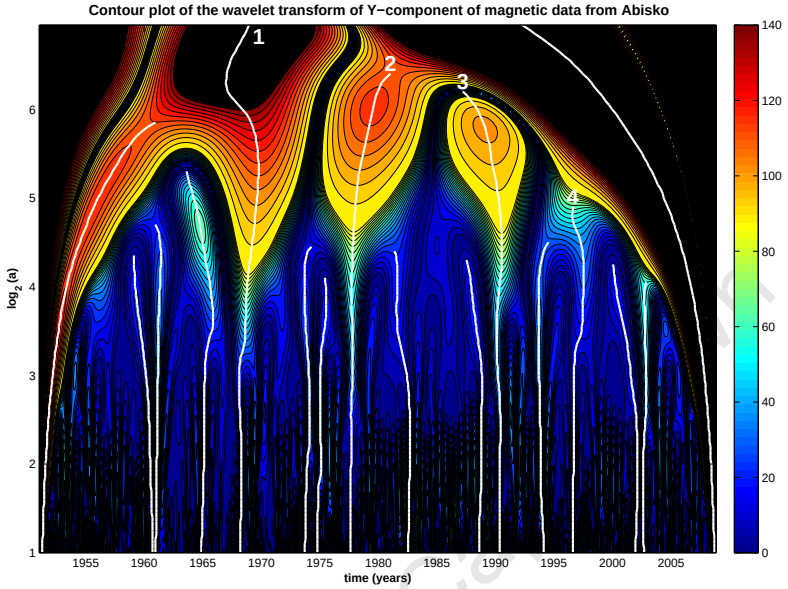

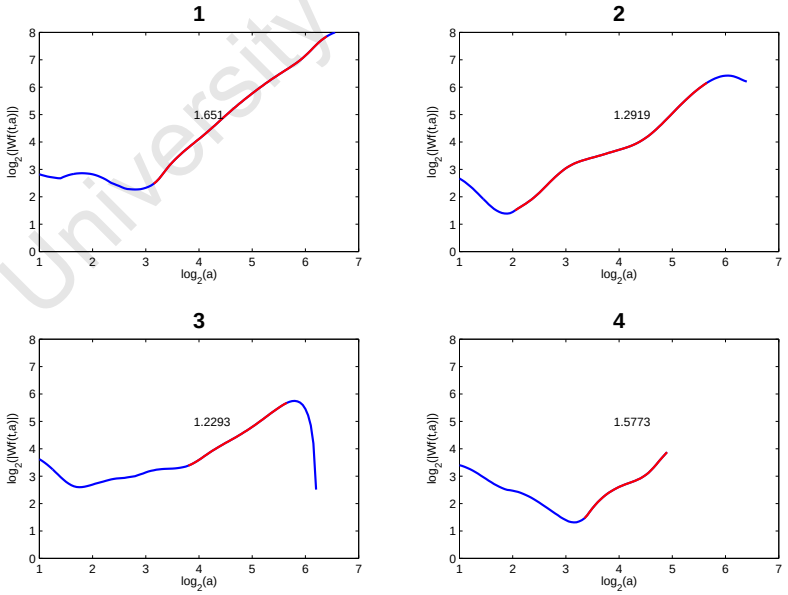

B.8 Eskaldelmuir (ESK)

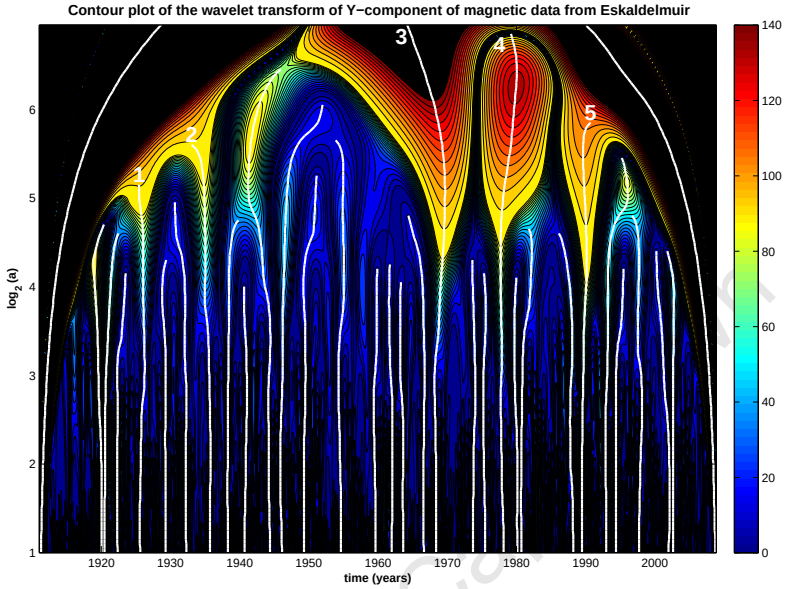

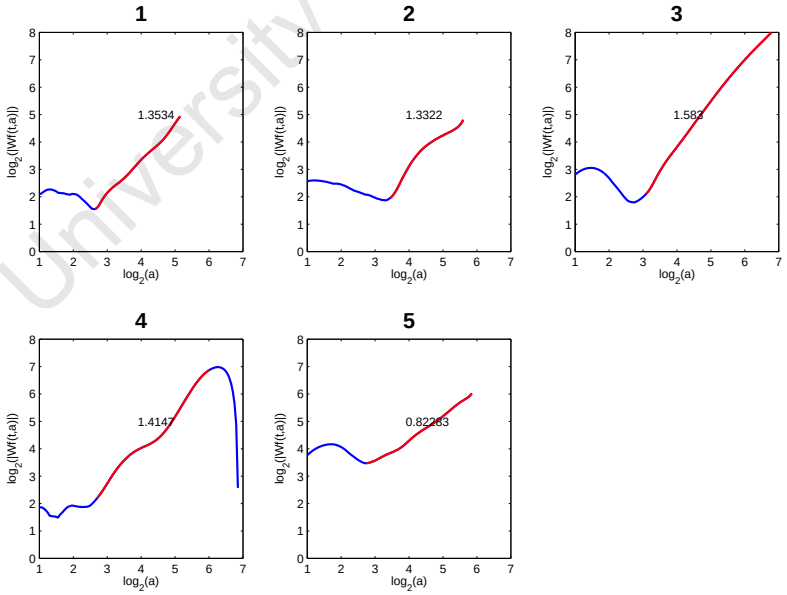

B.9 Fort Churchill (FCC)

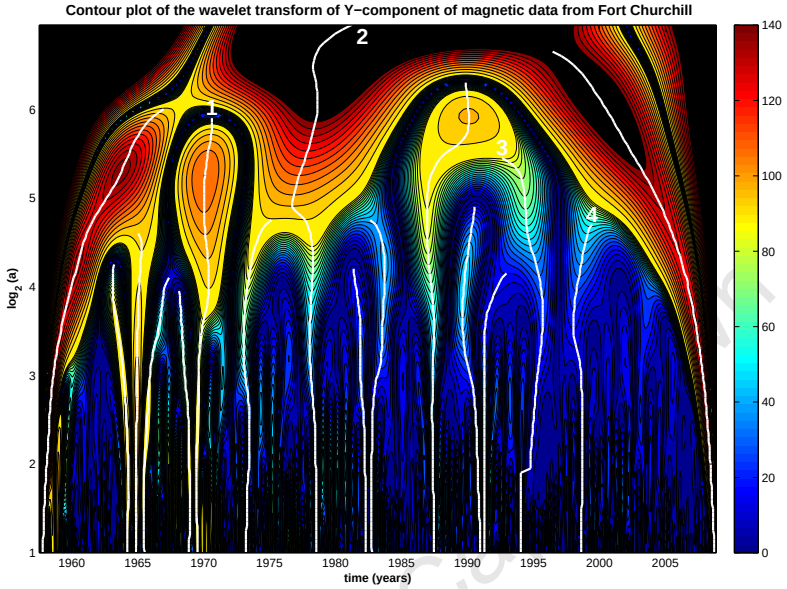

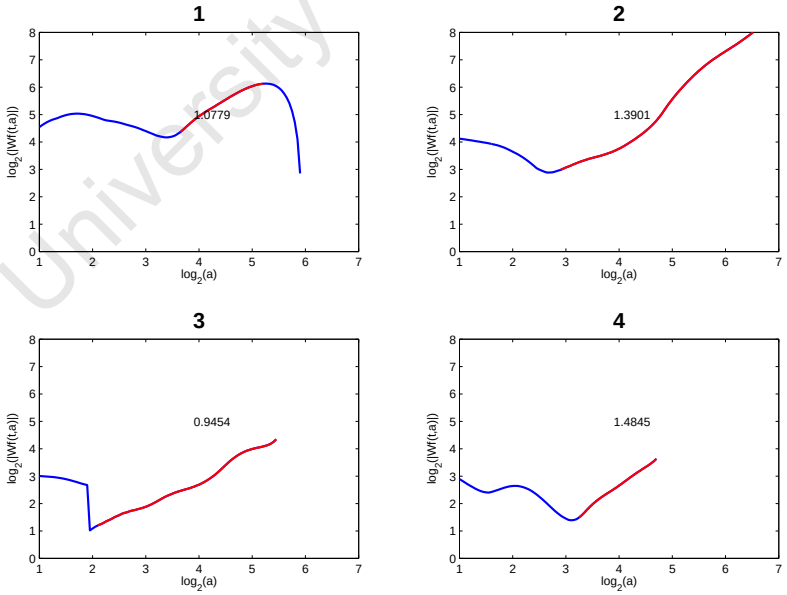

B.10 Fredericksburg (FRD)

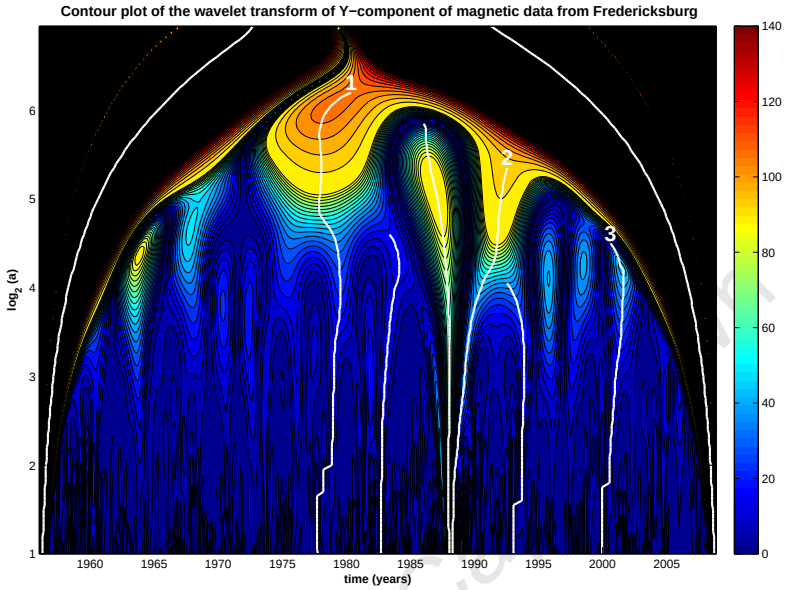

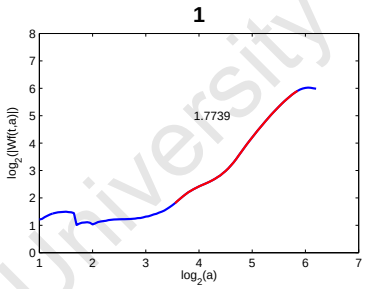

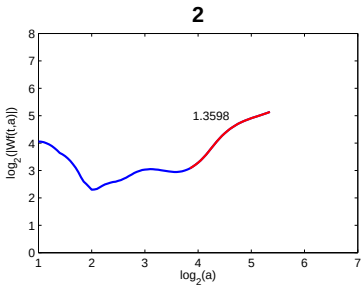

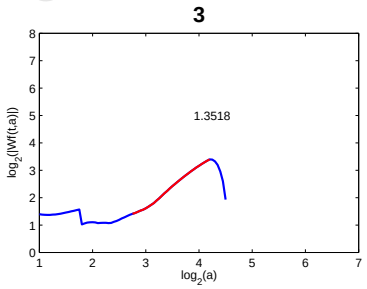

B.11 Furstenfeldbruck (FUR)

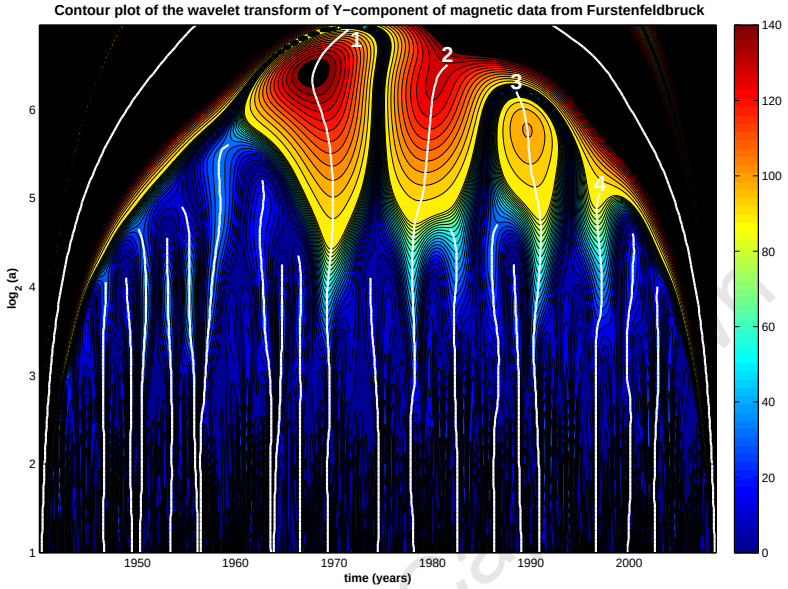

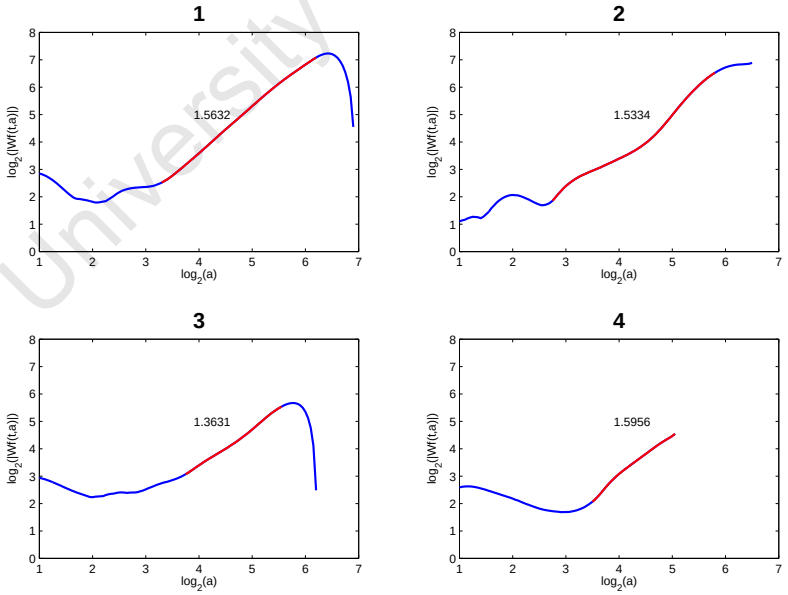

B.12 Gnangara (GNA)

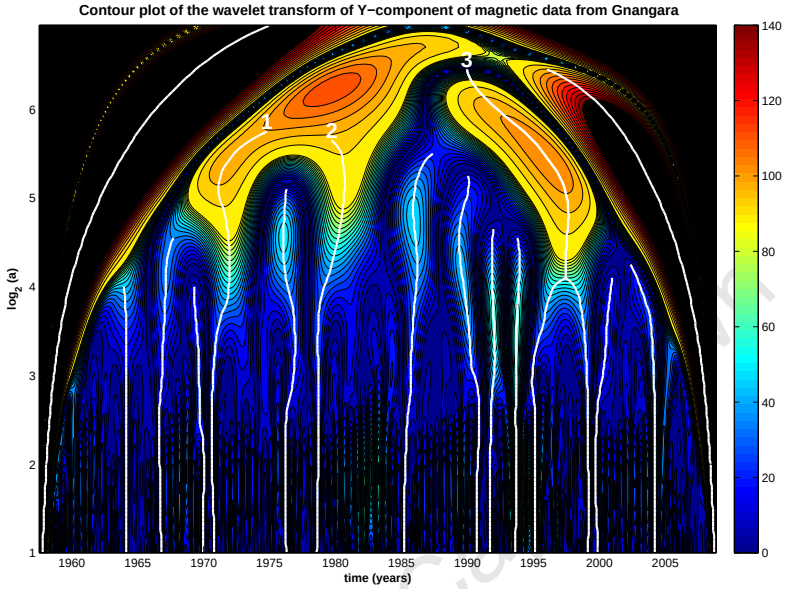

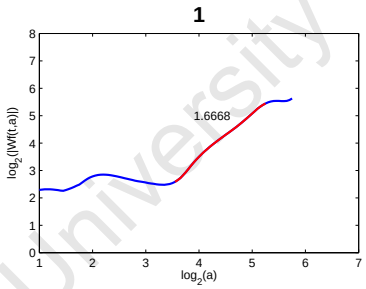

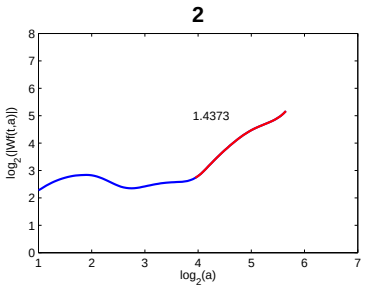

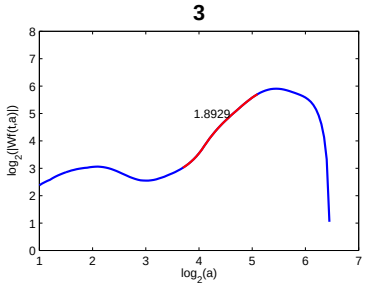

B.13 Guam (GUA)

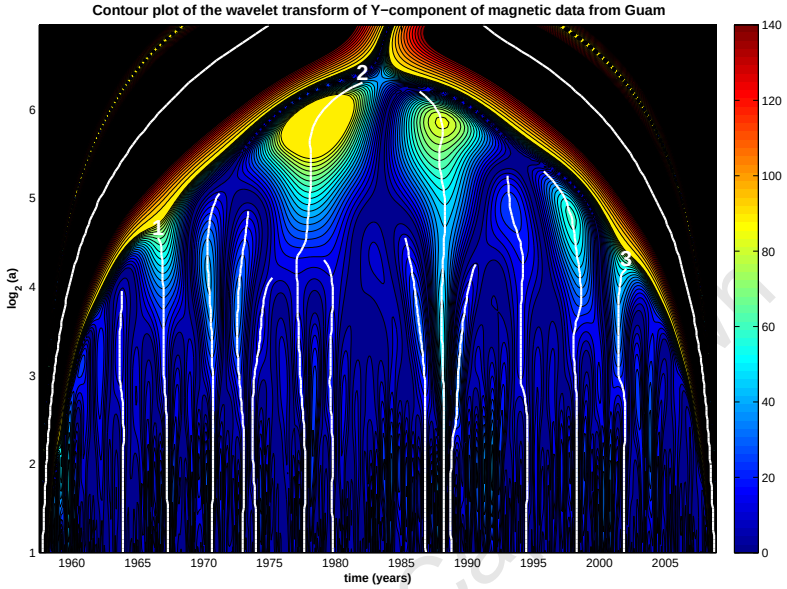

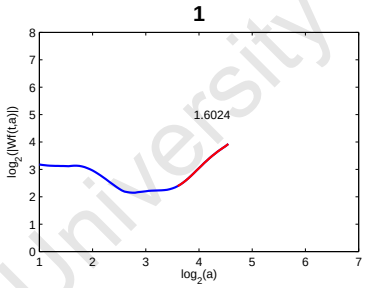

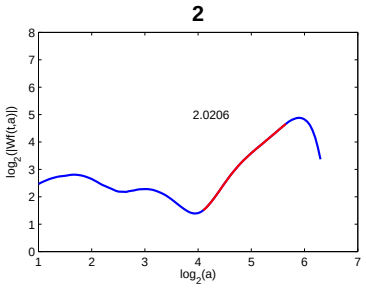

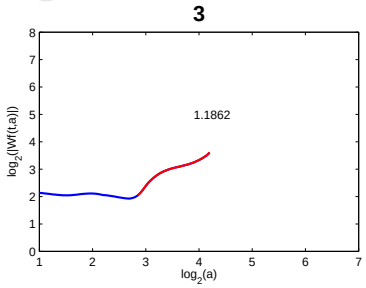

B.14 Hartebeesthoek (HBK)

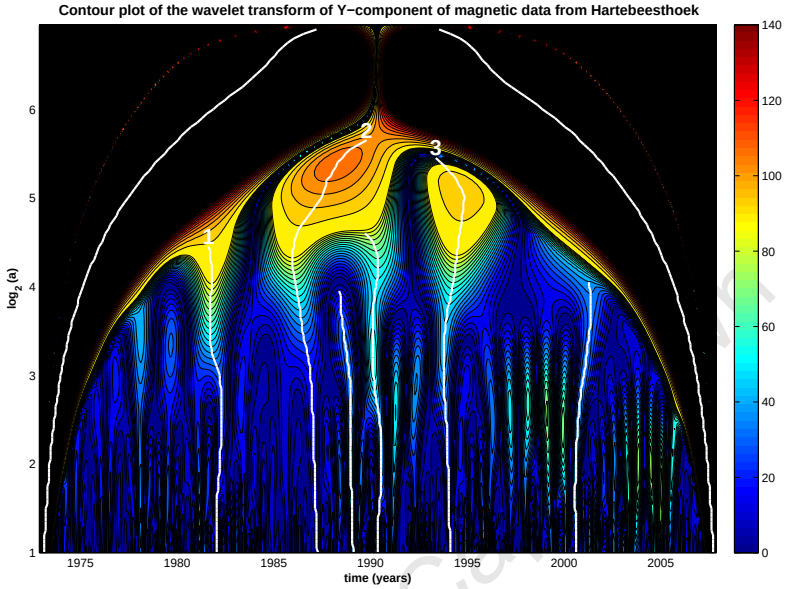

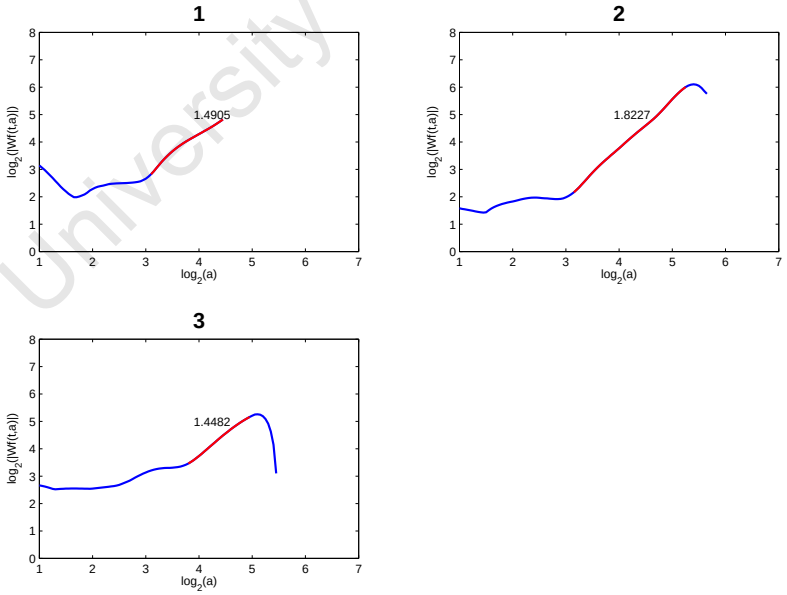

B.15 Hermanus (HER)

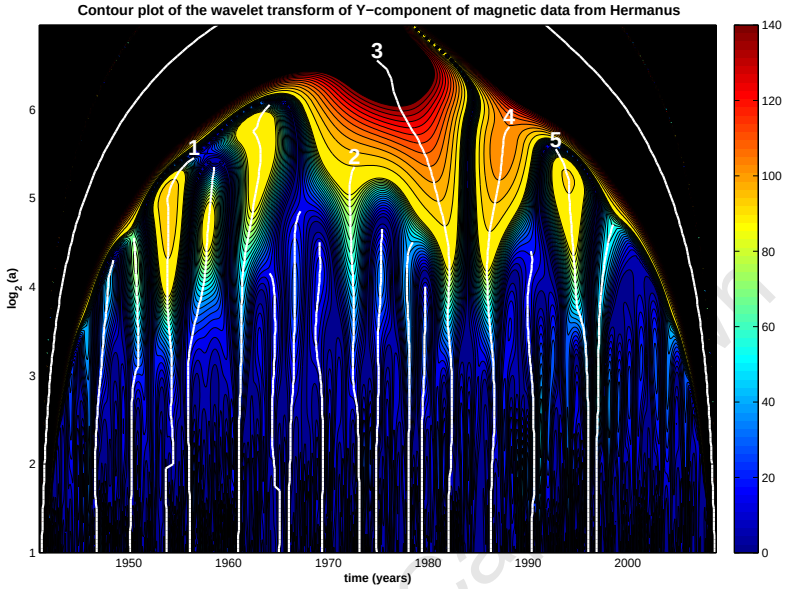

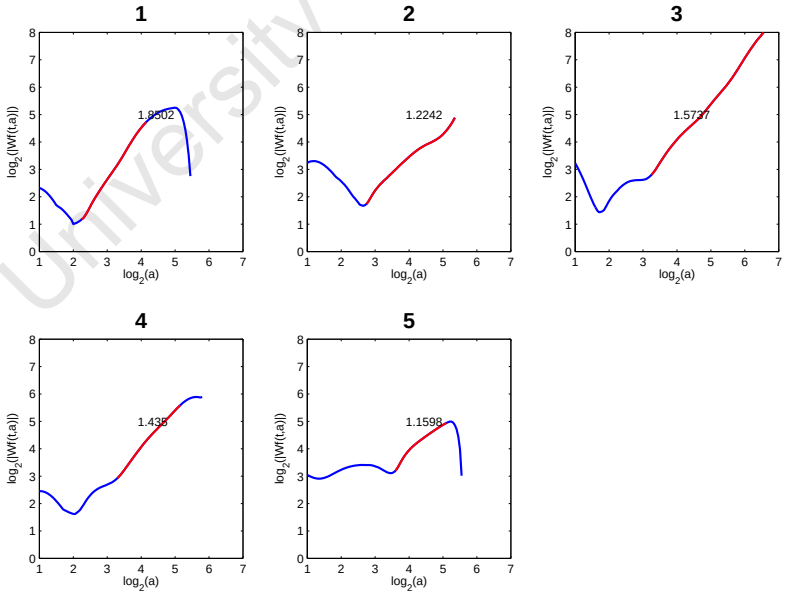

B.16 Honolulu (HON)

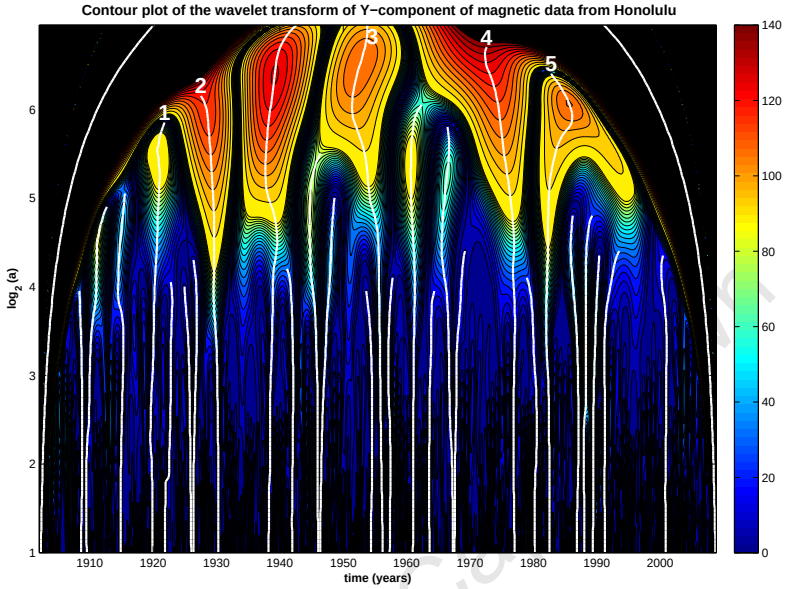

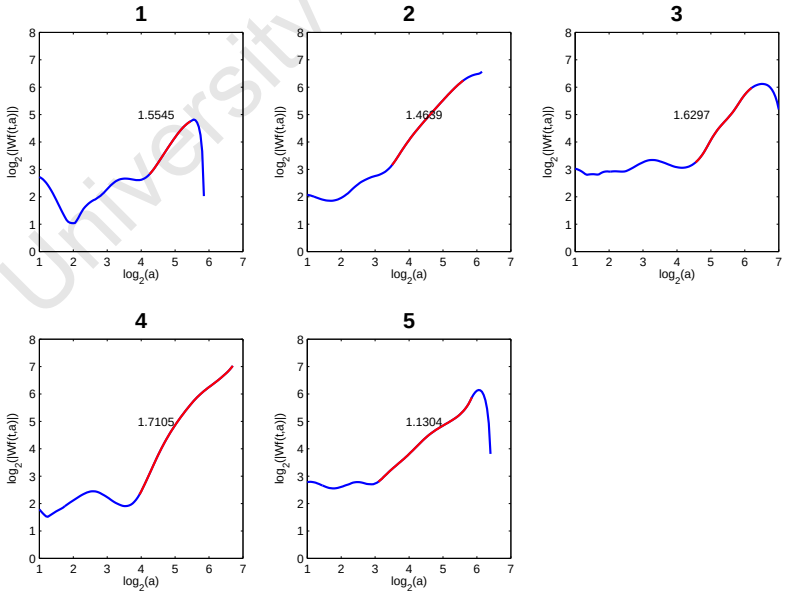

B.17 Huancayo (HUA)

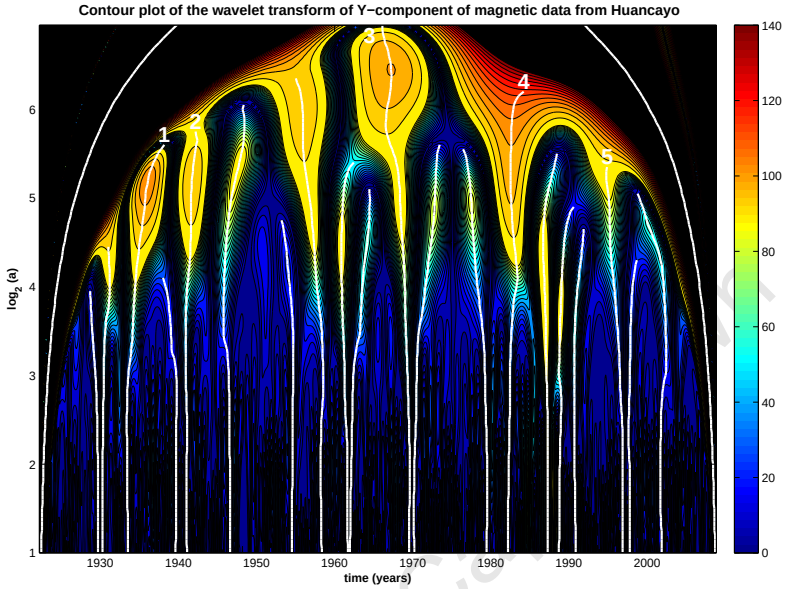

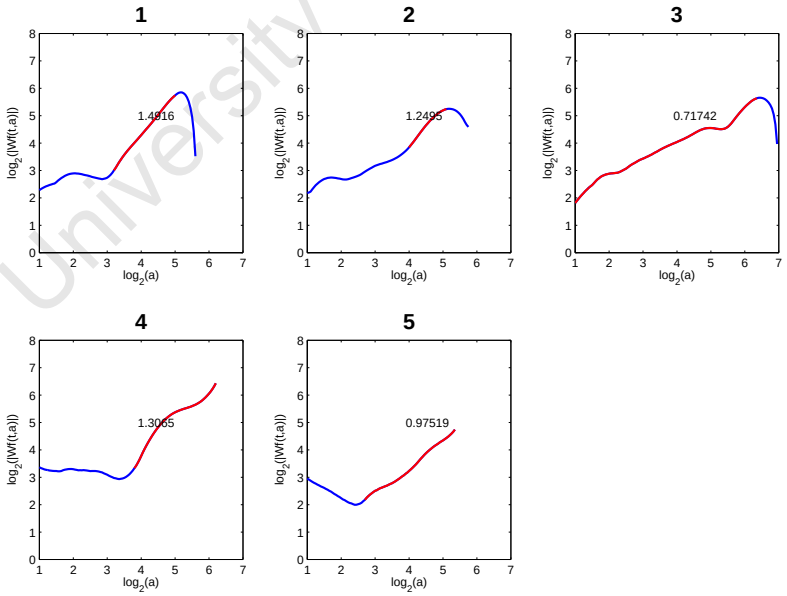

B.18 Hurbanovo (HRB)

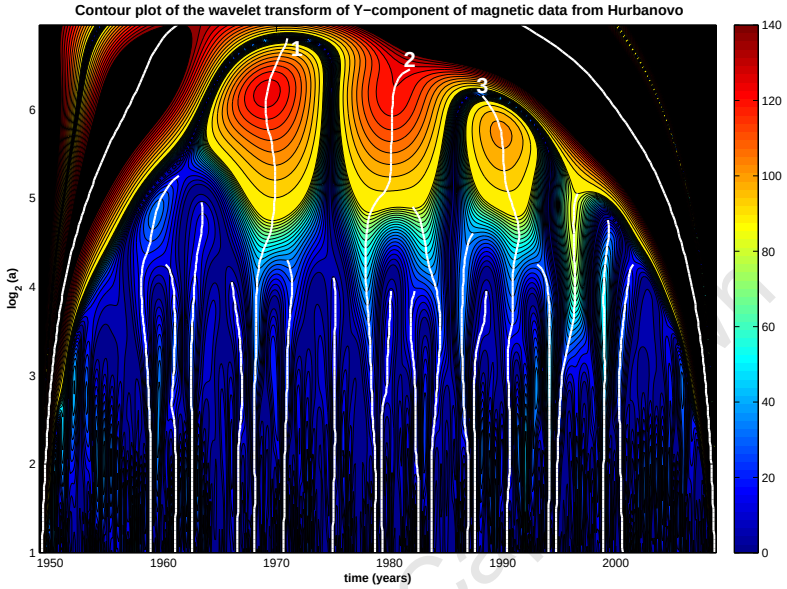

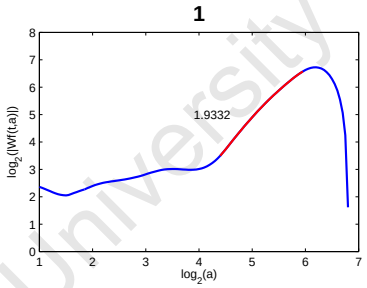

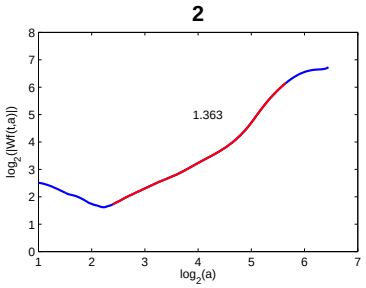

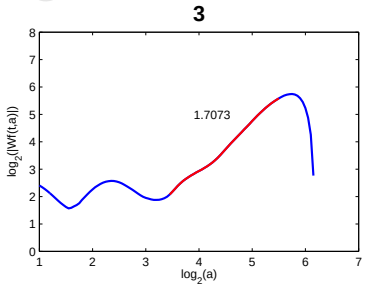

B.19 Kakioka (KAK)

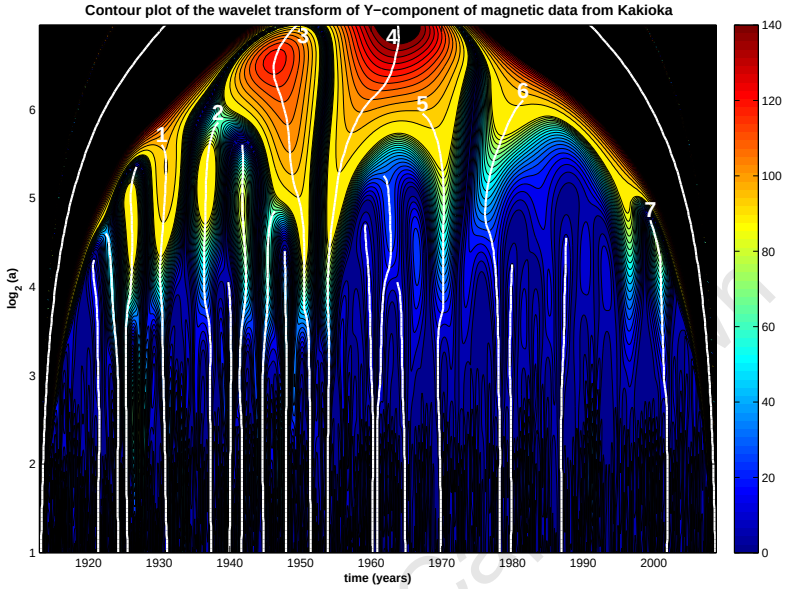

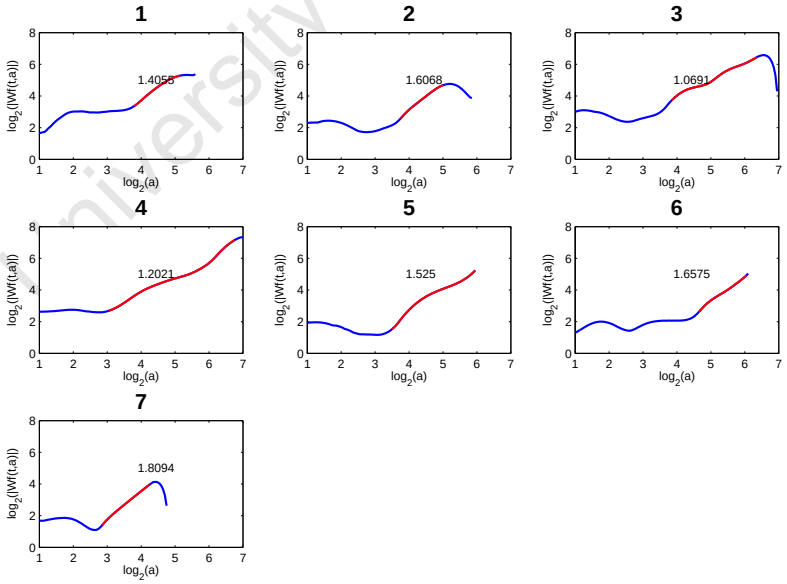

B.20 Kanoya (KNY)

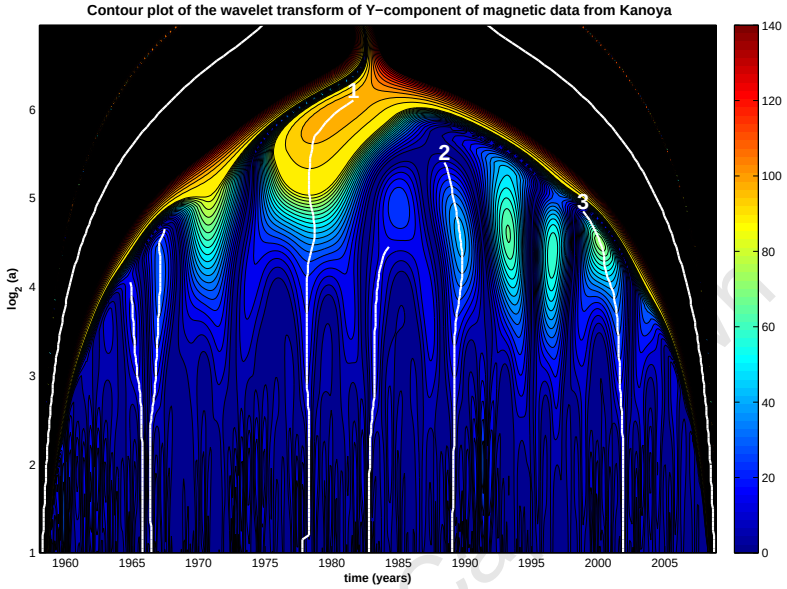

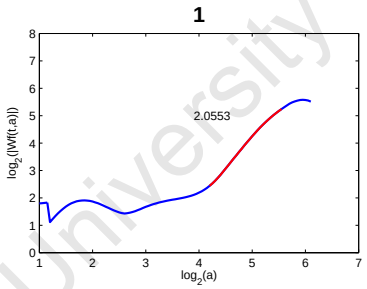

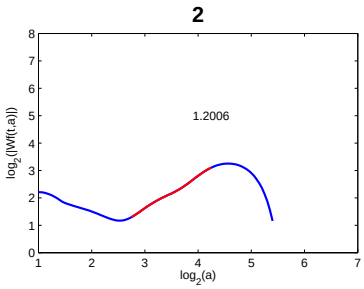

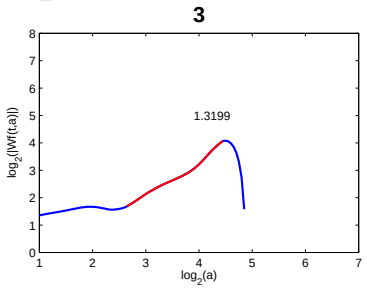

B.21 Lerwick (LER)

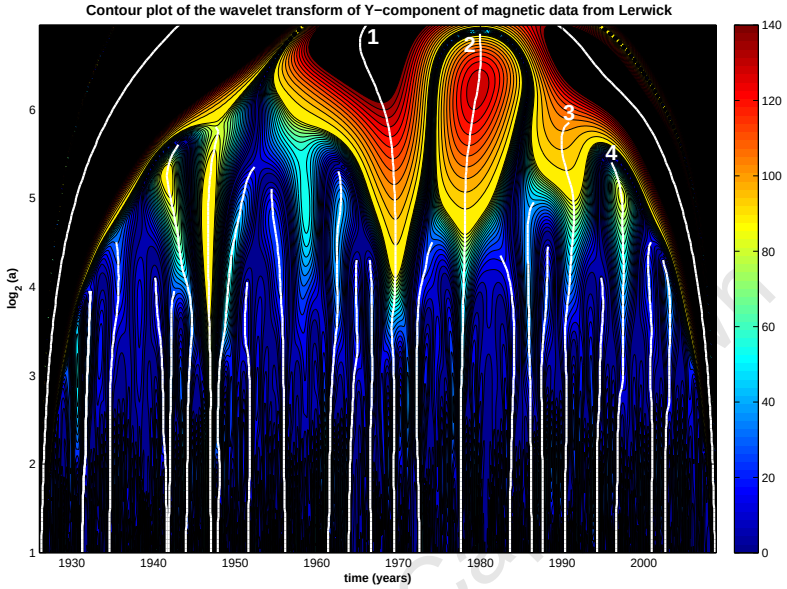

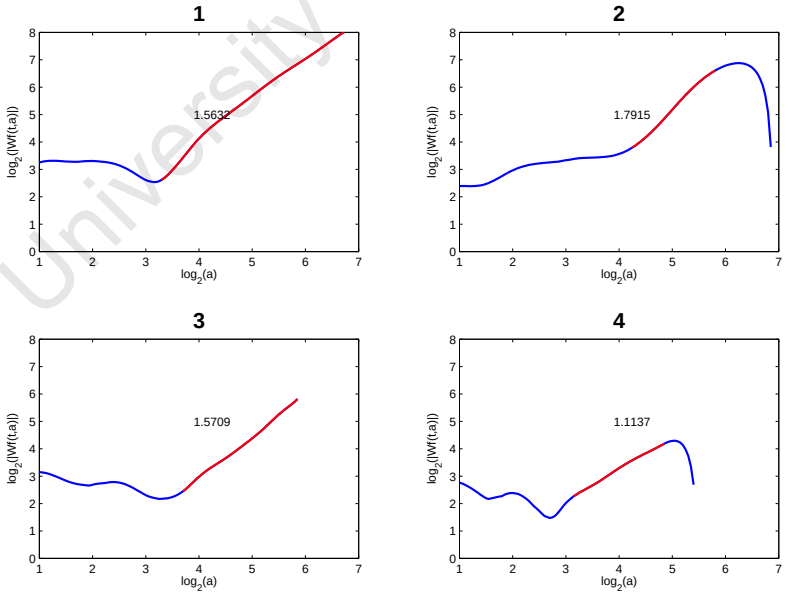

B.22 Lovoe (LOV)

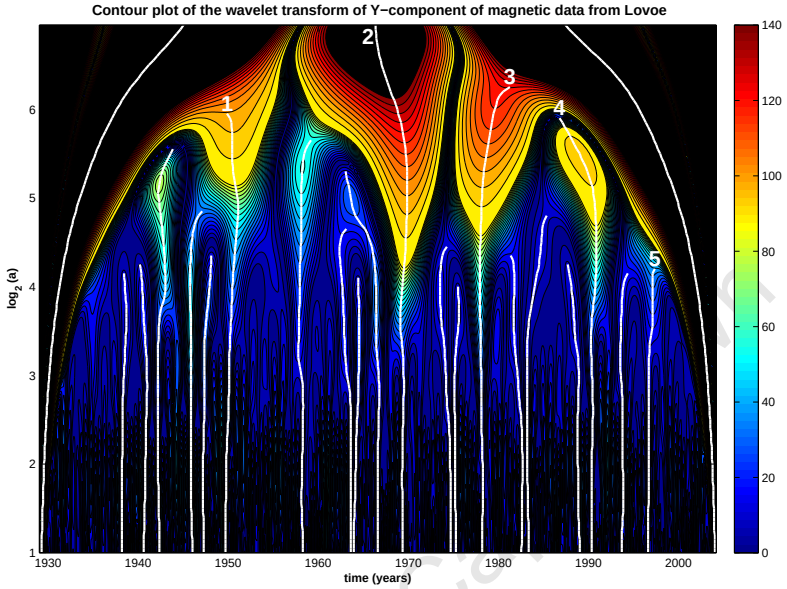

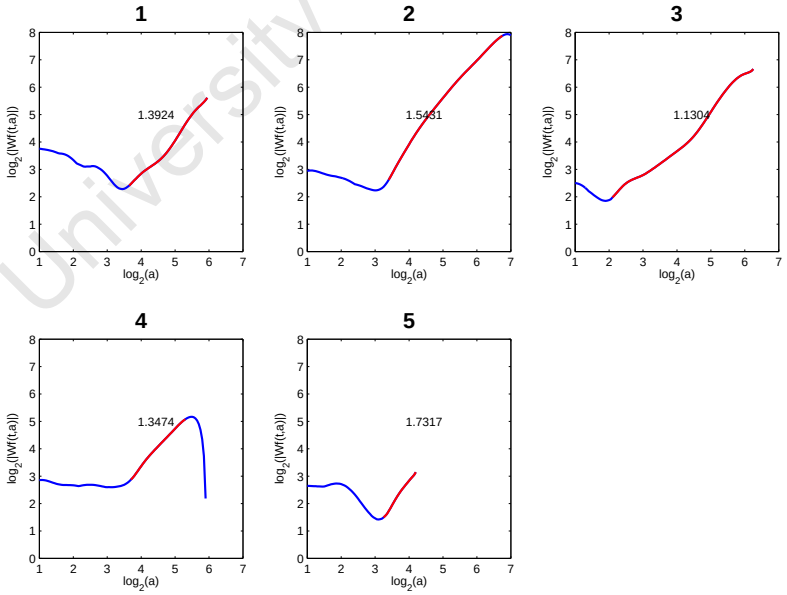

B.23 Mbour (MBO)

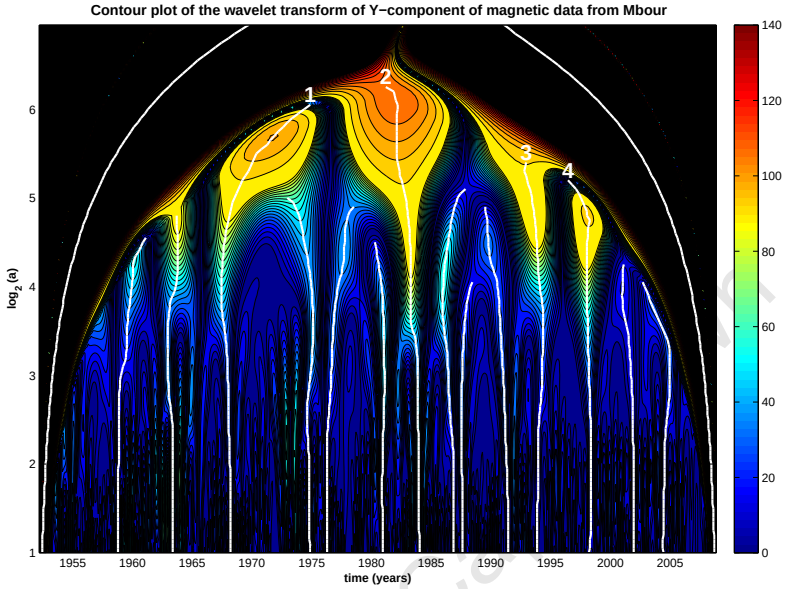

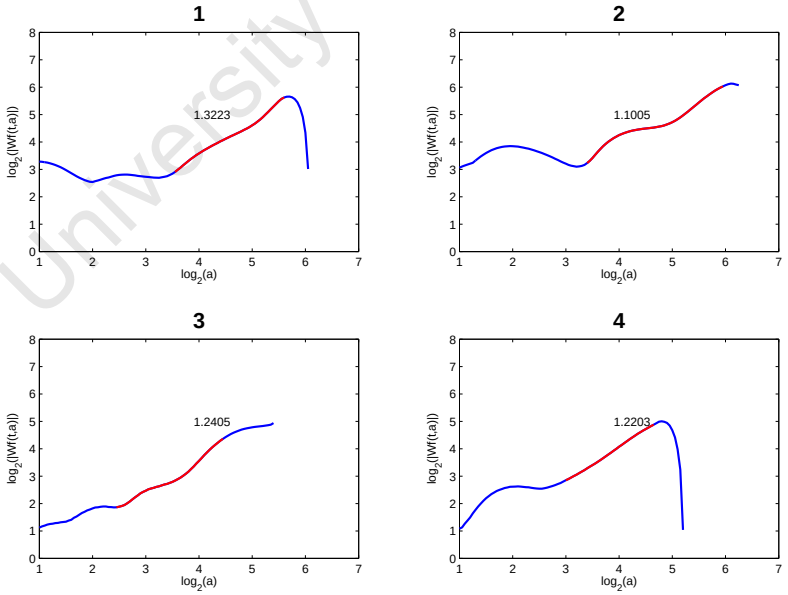

B.24 Meanhook (MEA)

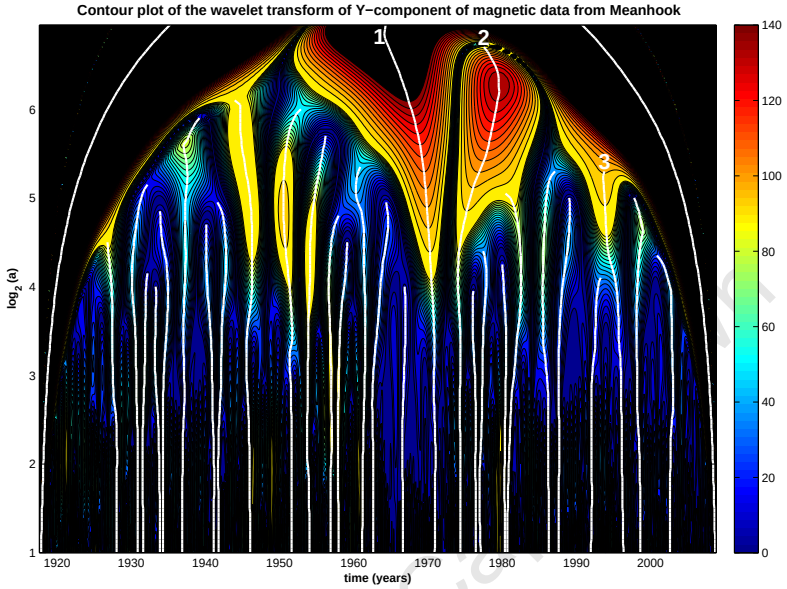

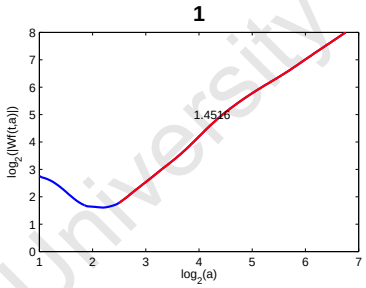

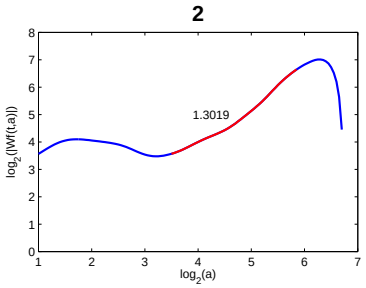

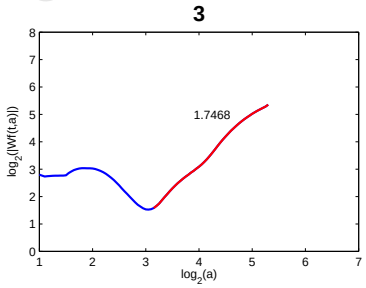

B.25 Memambetsu (MMB)

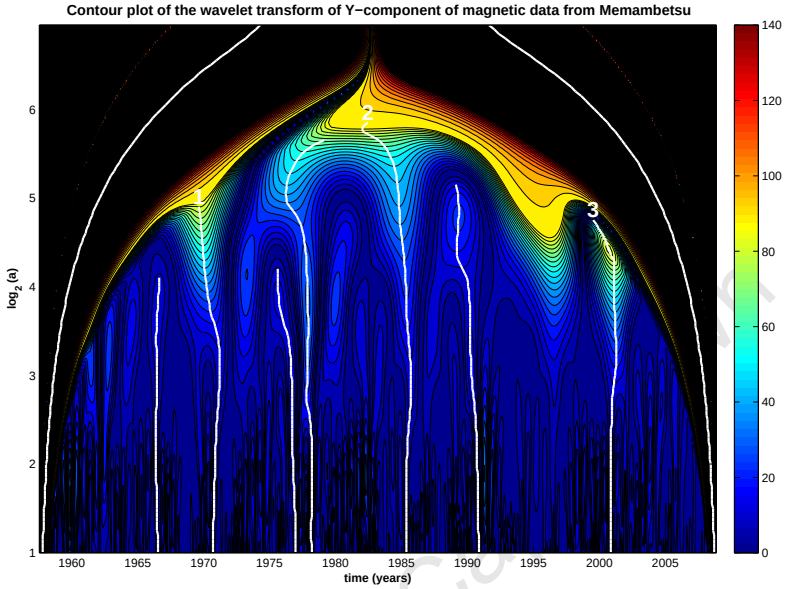

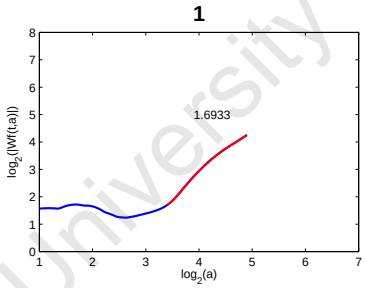

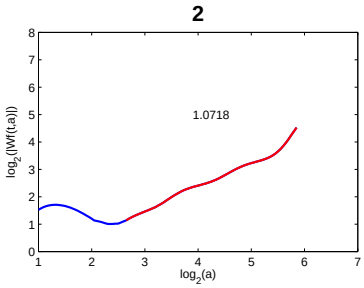

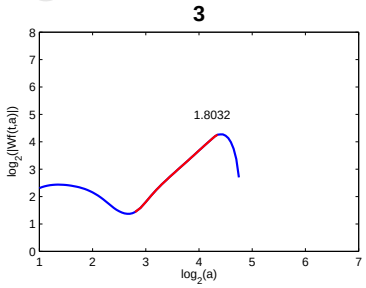

B.26 Niemegk (NGK)

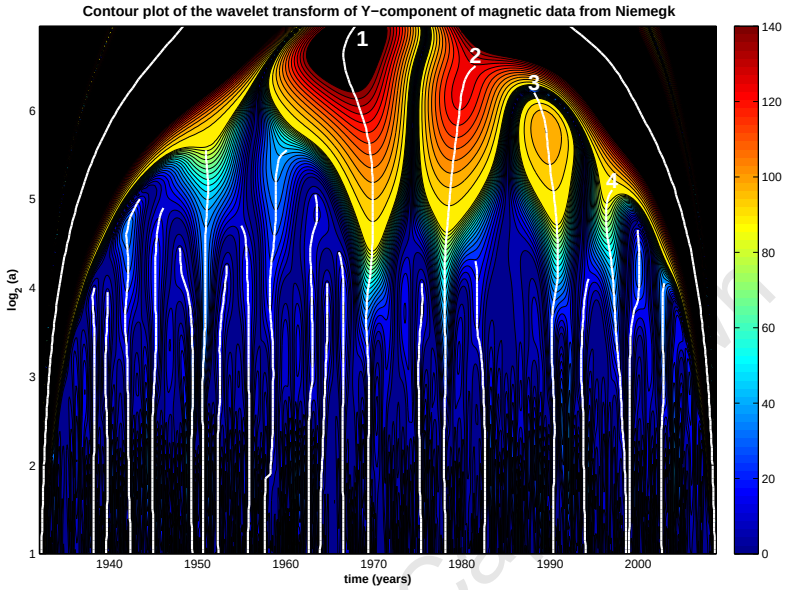

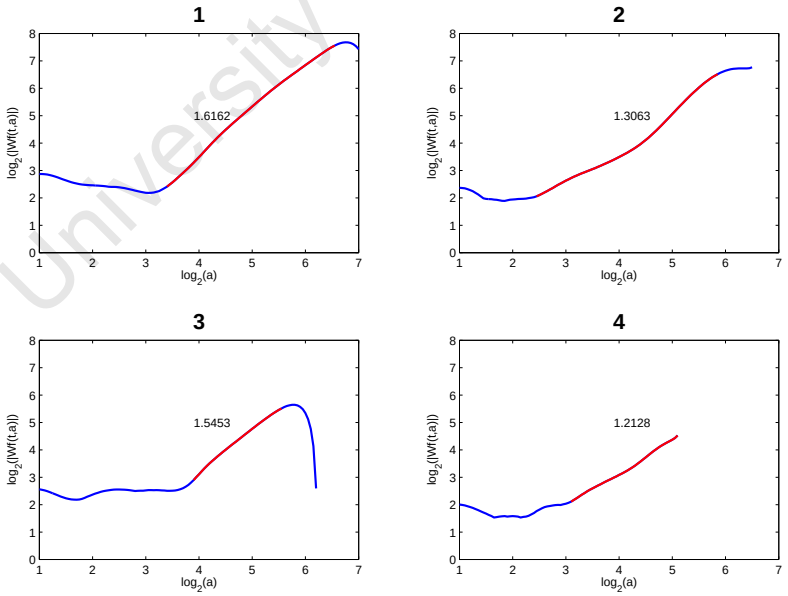

B.27 Novosibirsk (NVS)

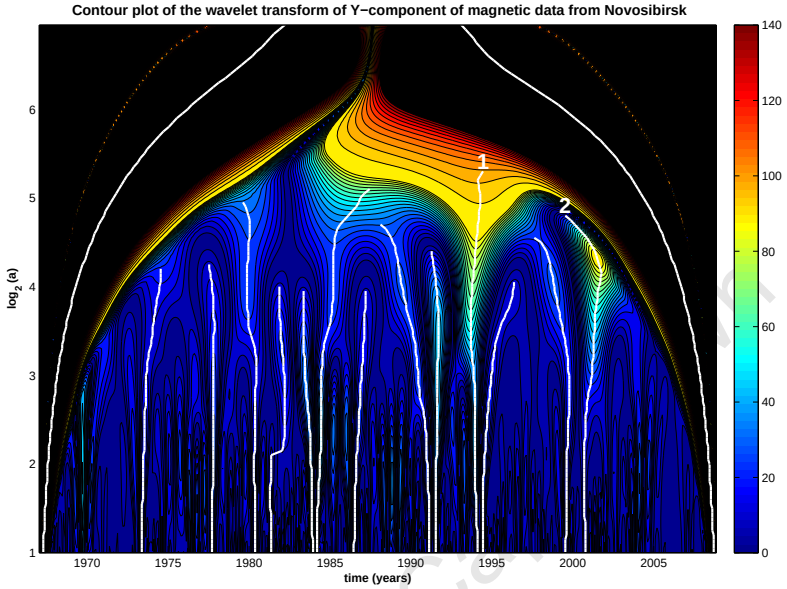

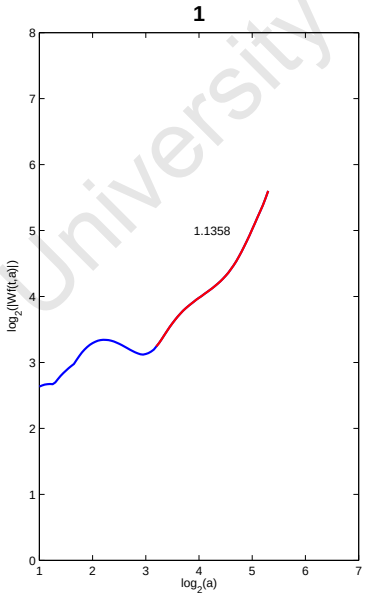

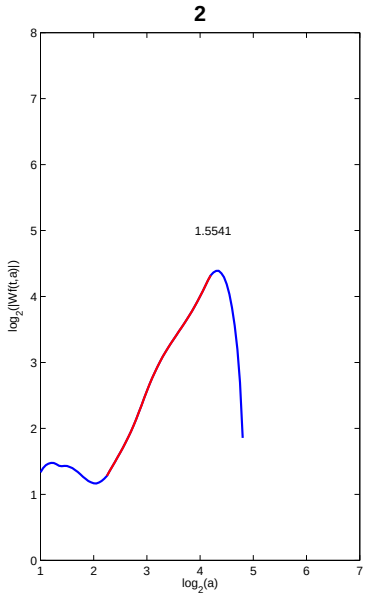

B.28 Nurmijarvi (NUR)

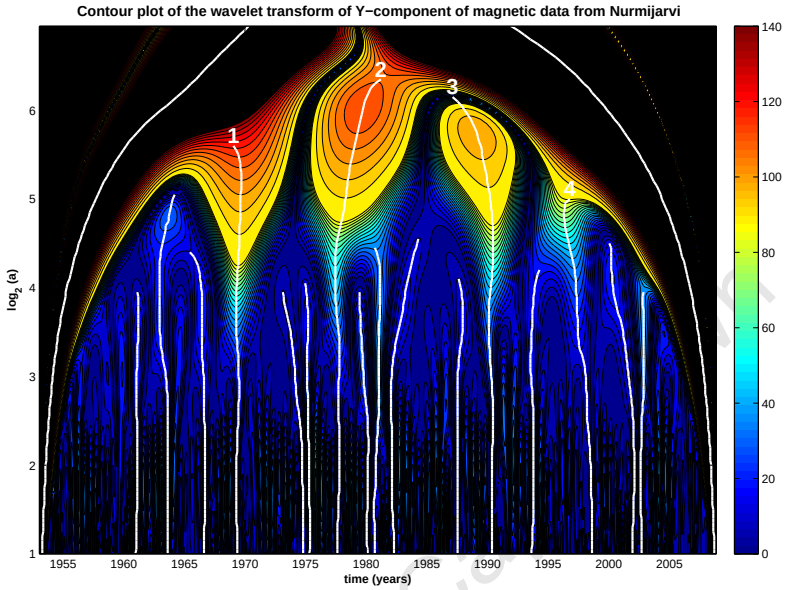

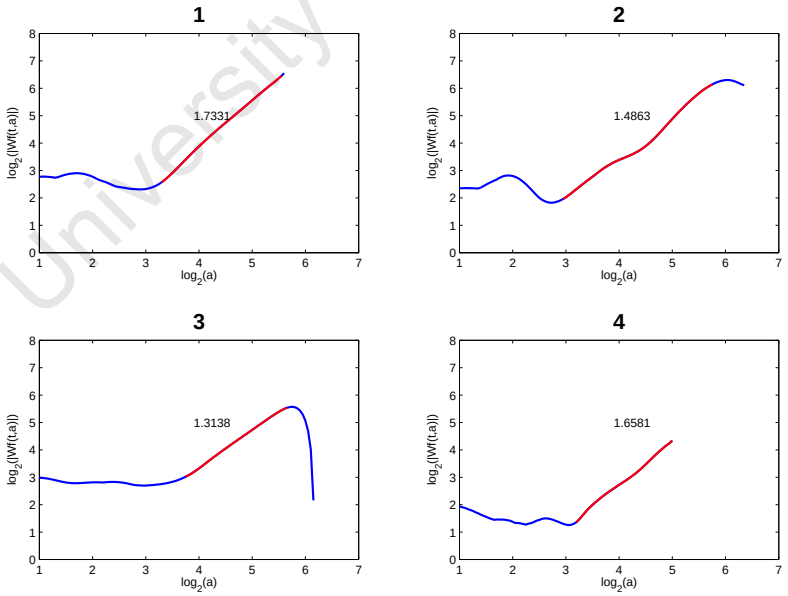

B.29 Pamatai (PPT)

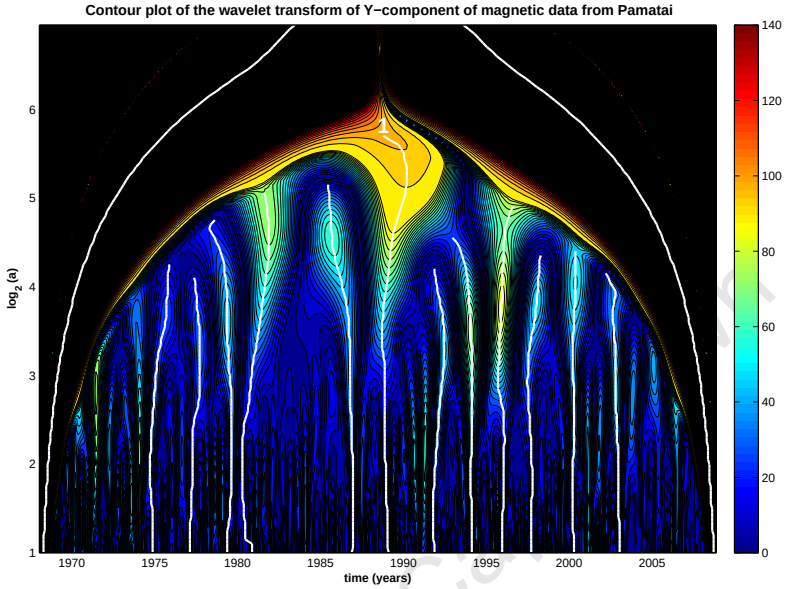

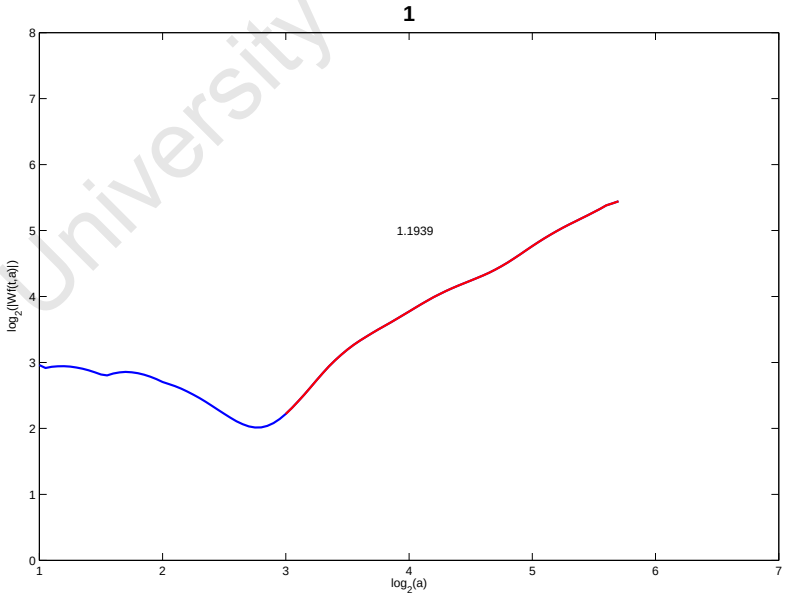

B.30 Port Aux Françis (ABK)

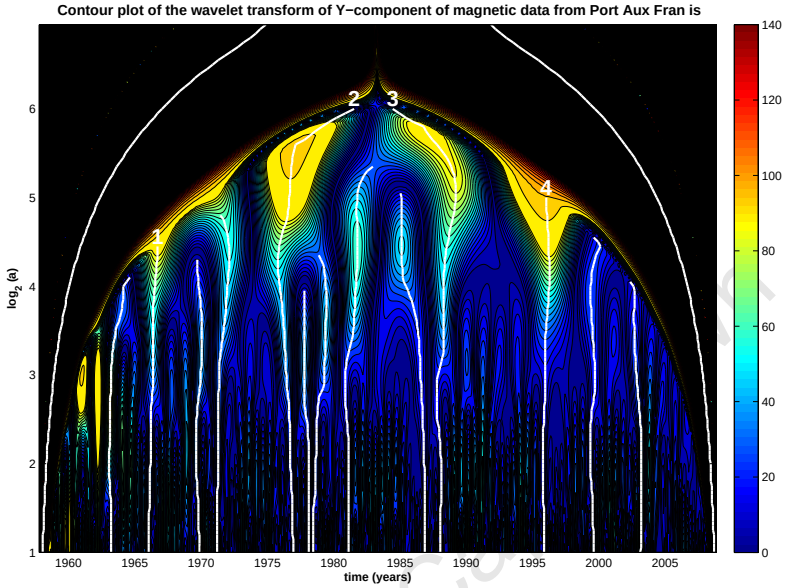

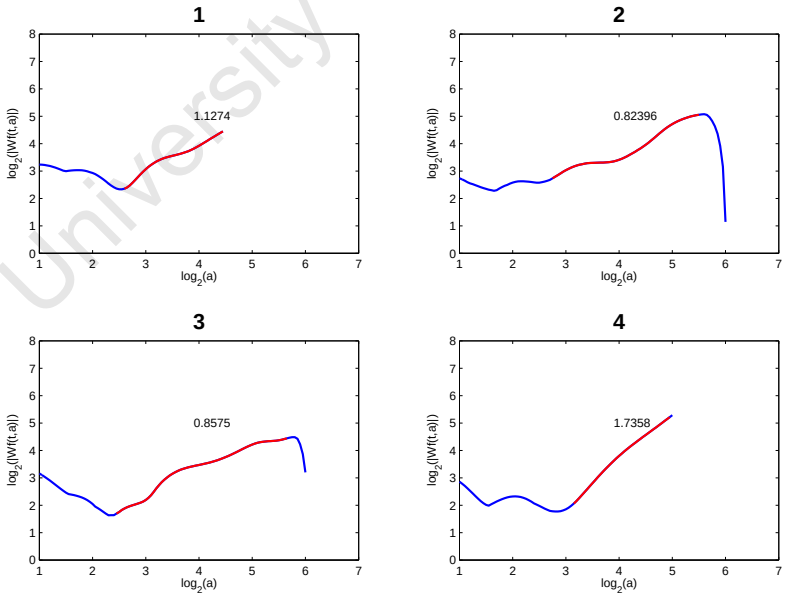

B.31 Resolute Bay (RES)

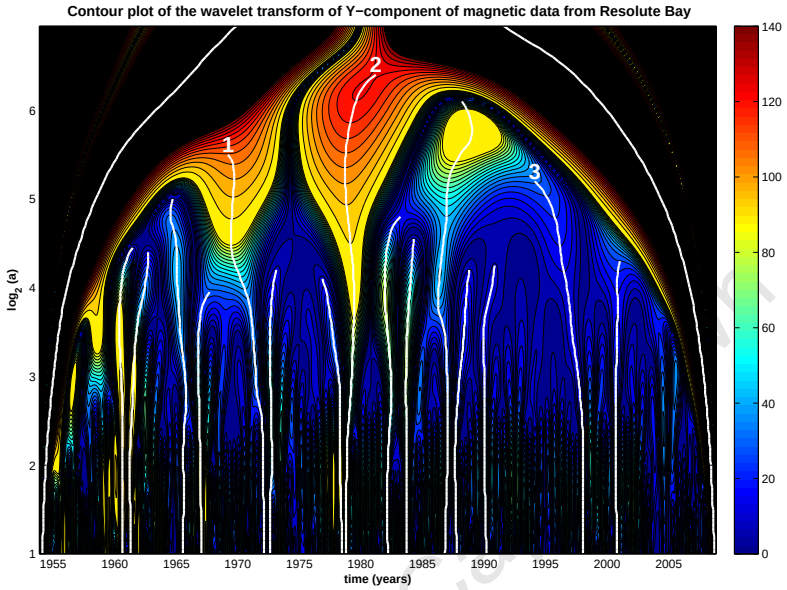

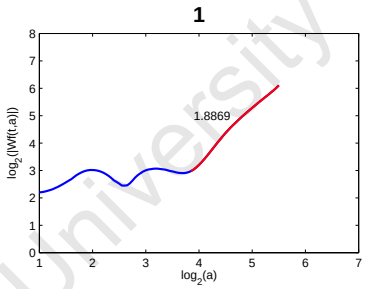

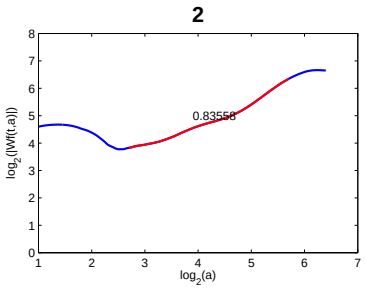

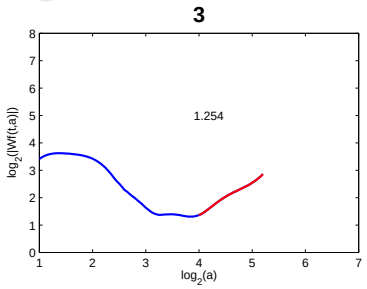

B.32 Rude Skov (RSV)

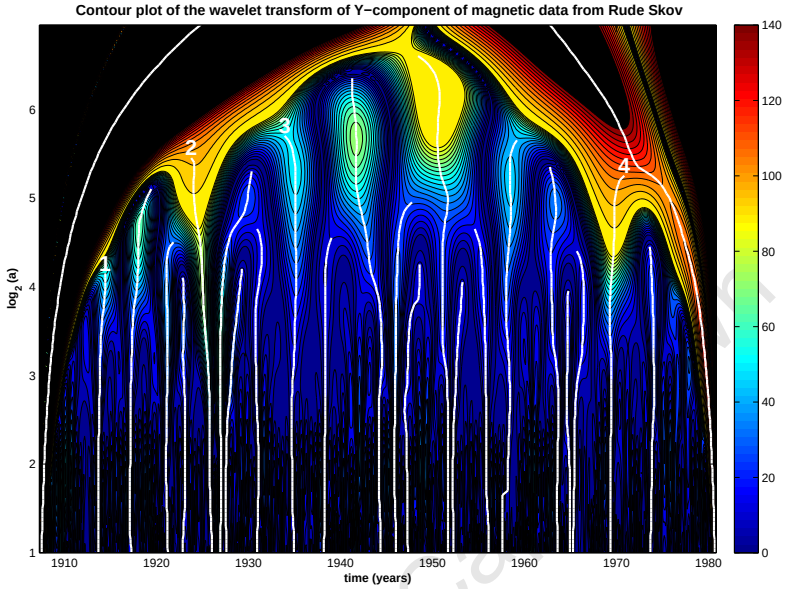

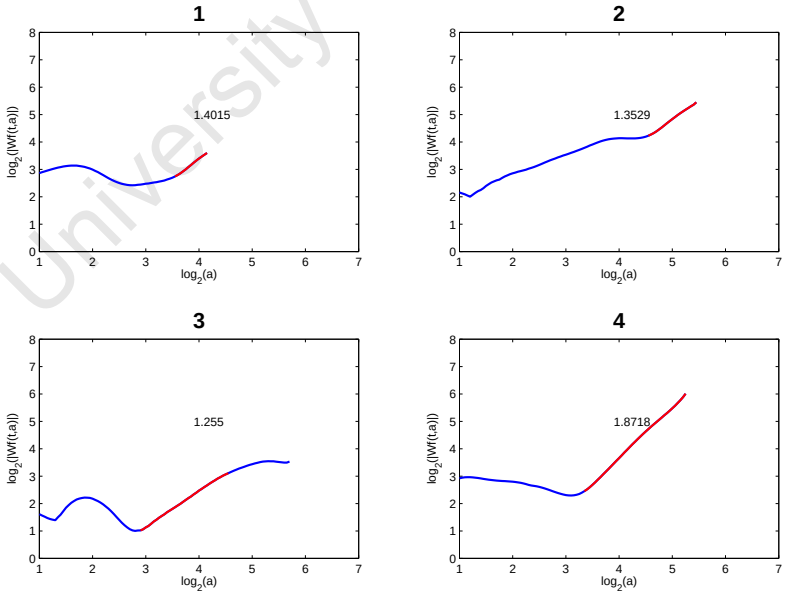

B.33 San Juan (SJG)

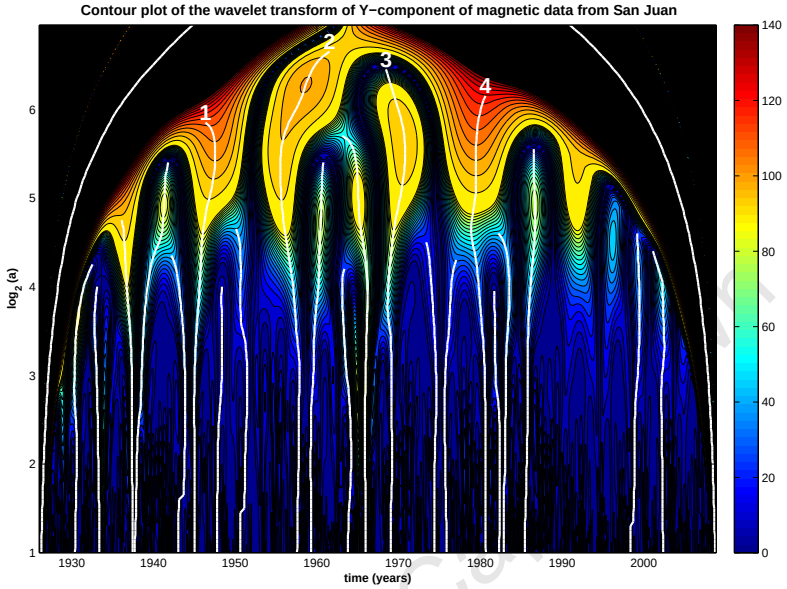

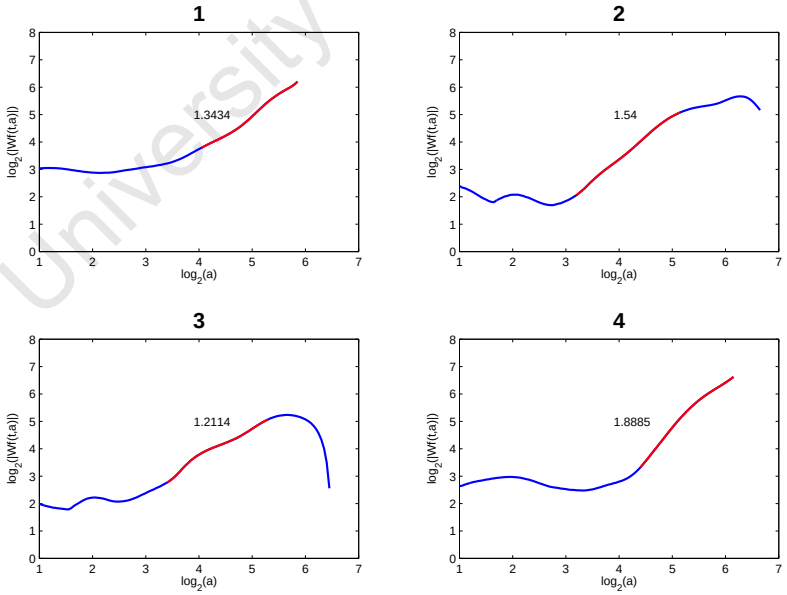

B.34 Scott Base (SBA)

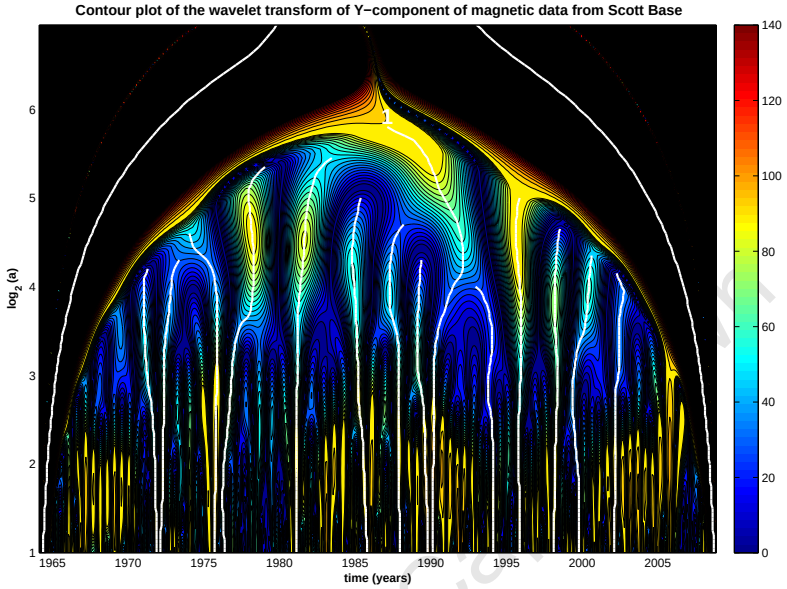

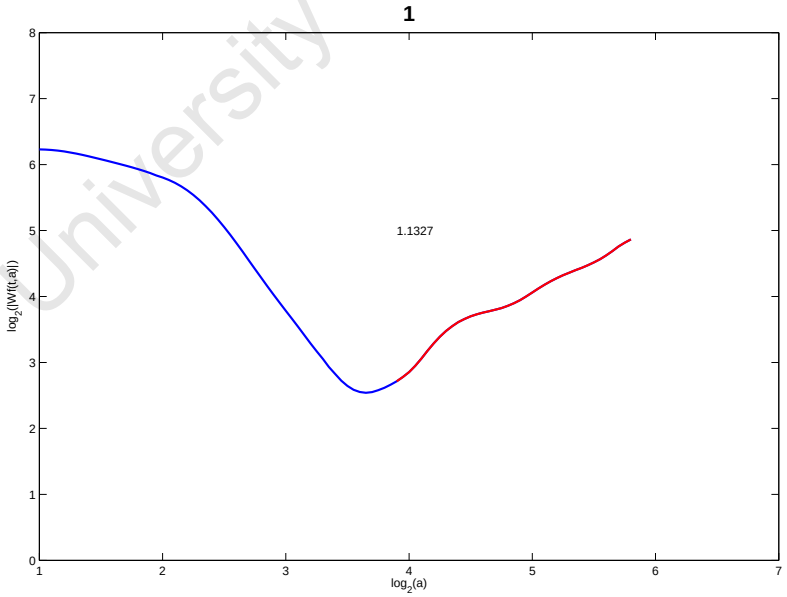

B.35 Sitka (SIT)

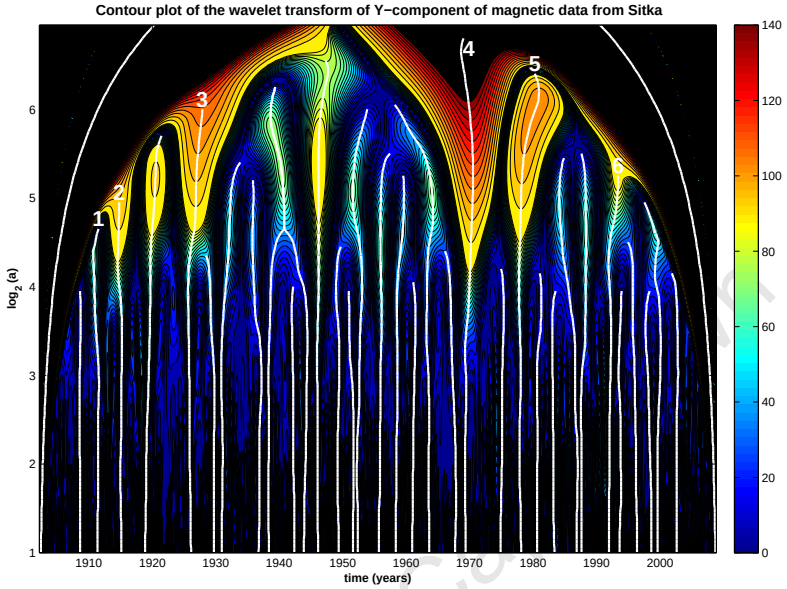

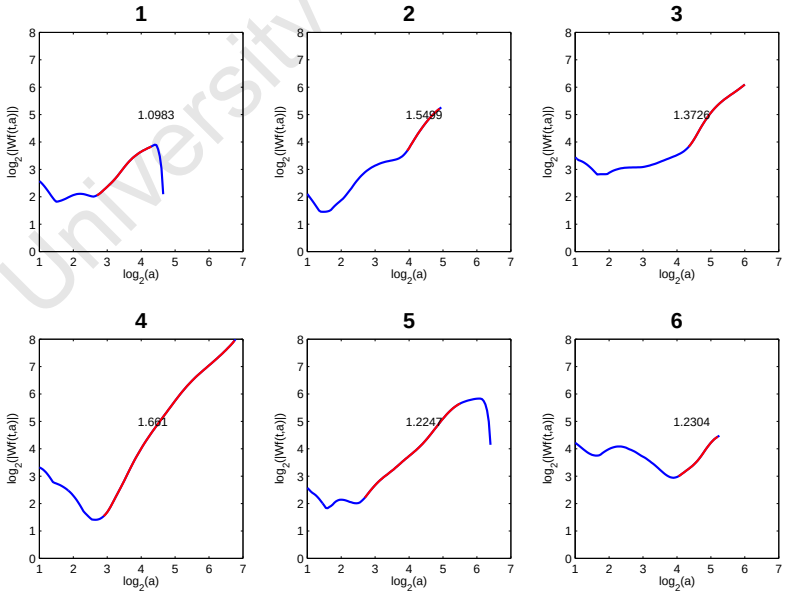

B.36 Sodankyla (SOD)

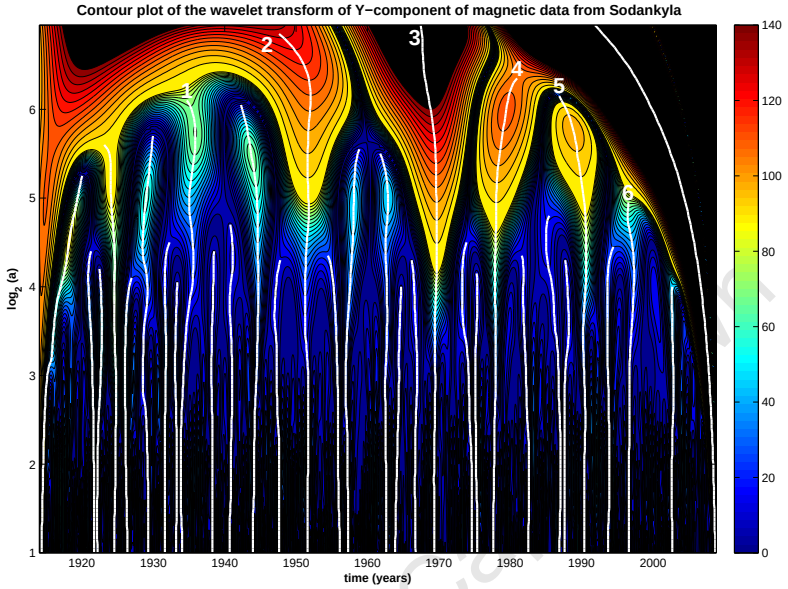

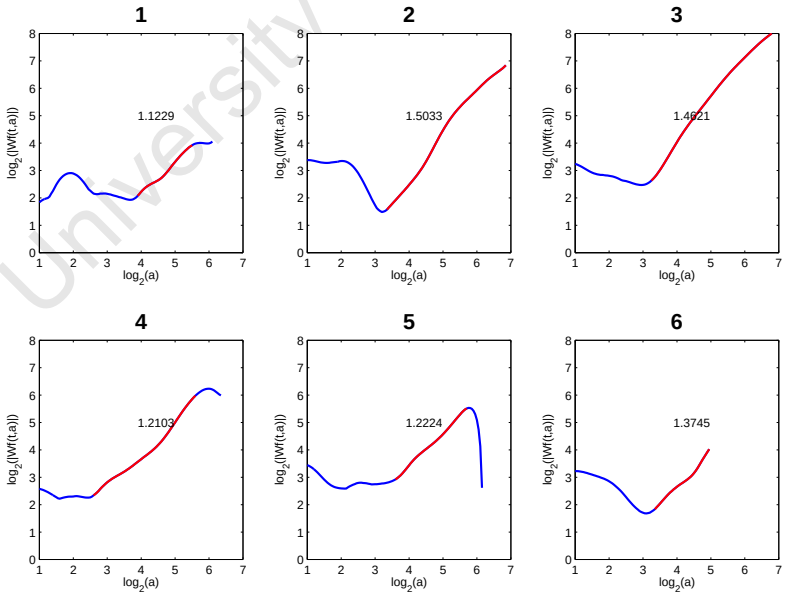

B.37 Tihany (THY)

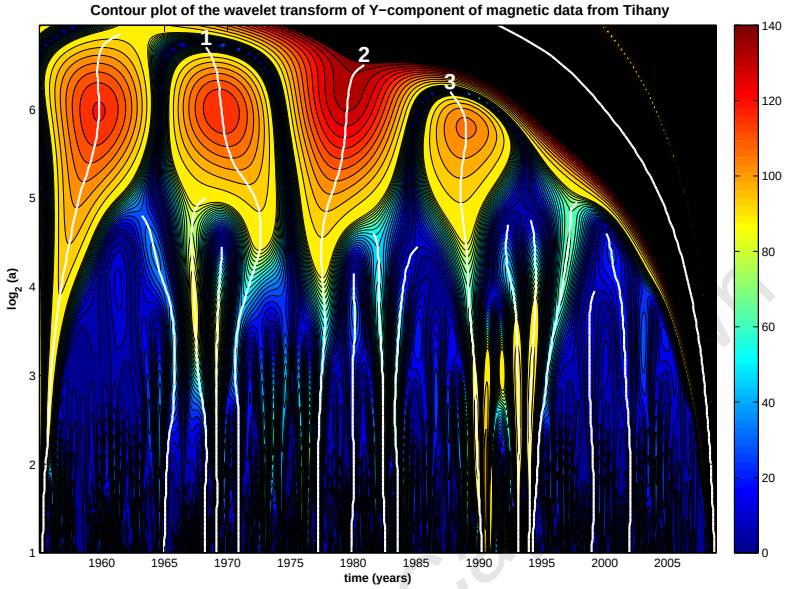

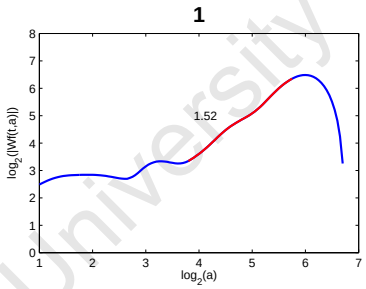

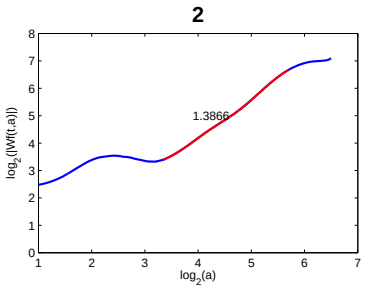

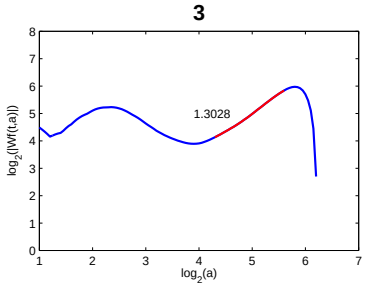

B.38 Toolangi (TOO)

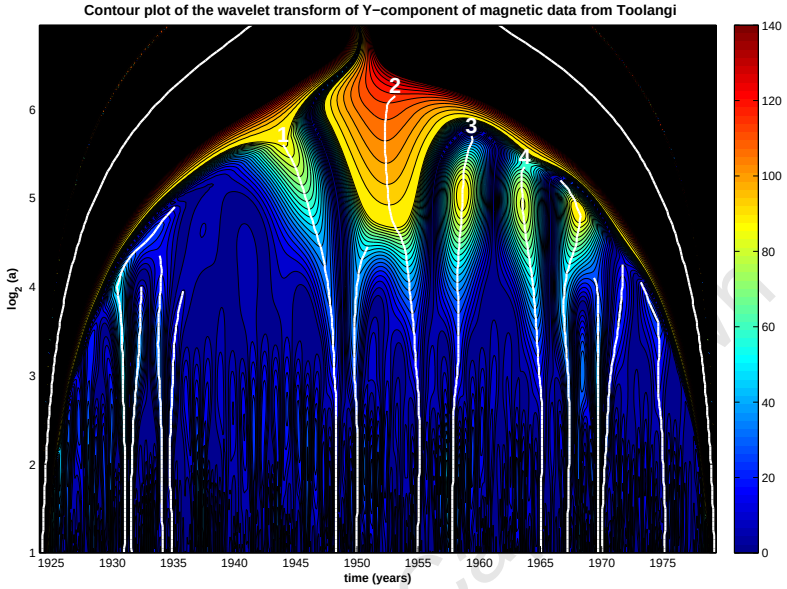

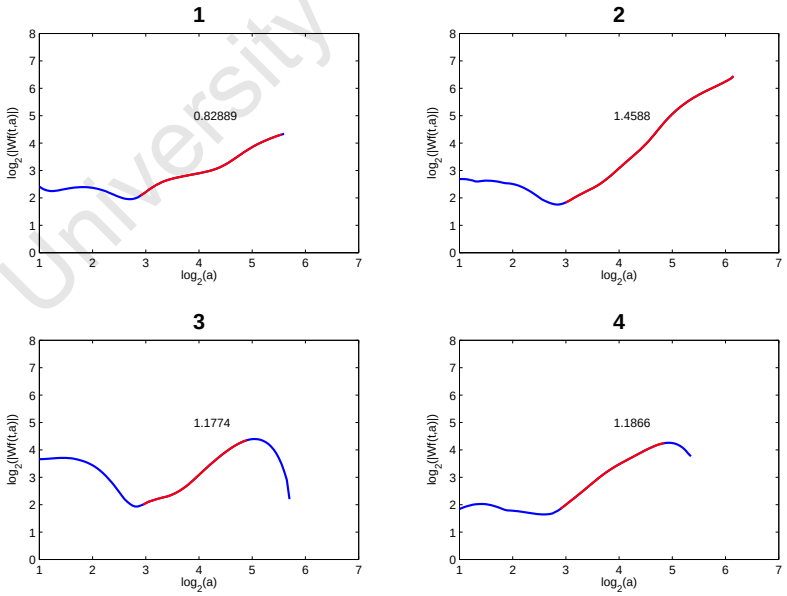

B.39 Tucson (TUC)

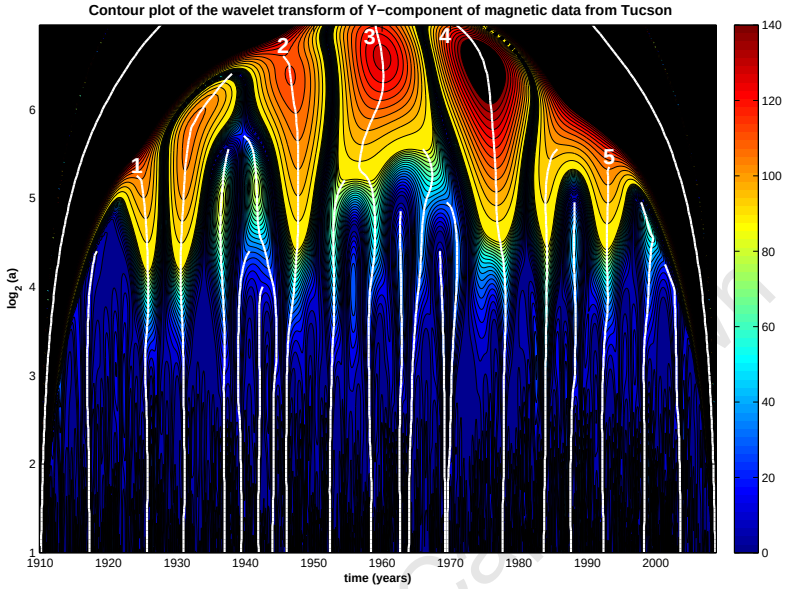

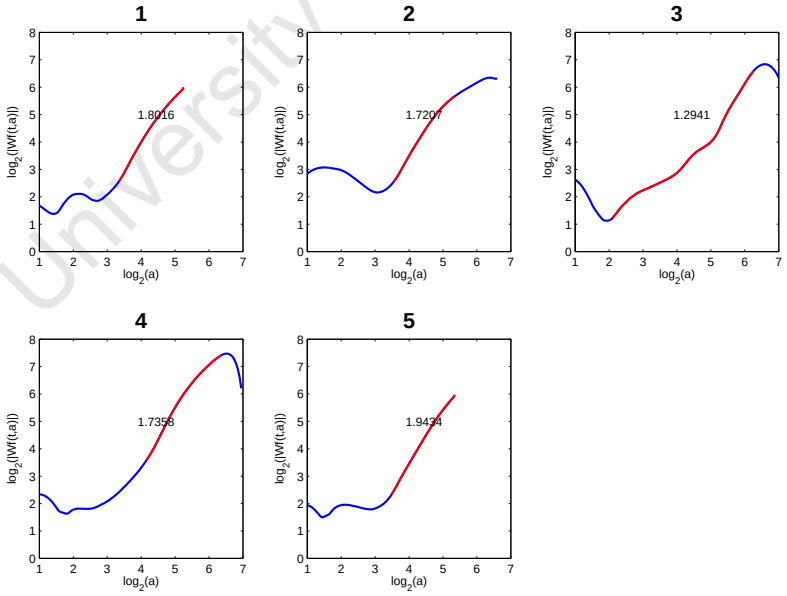

B.40 Val Joyeux (VLJ)

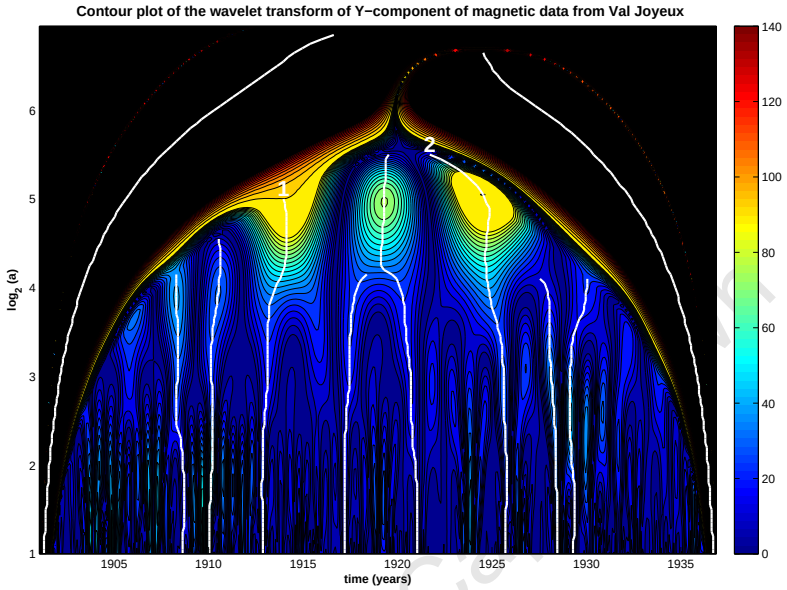

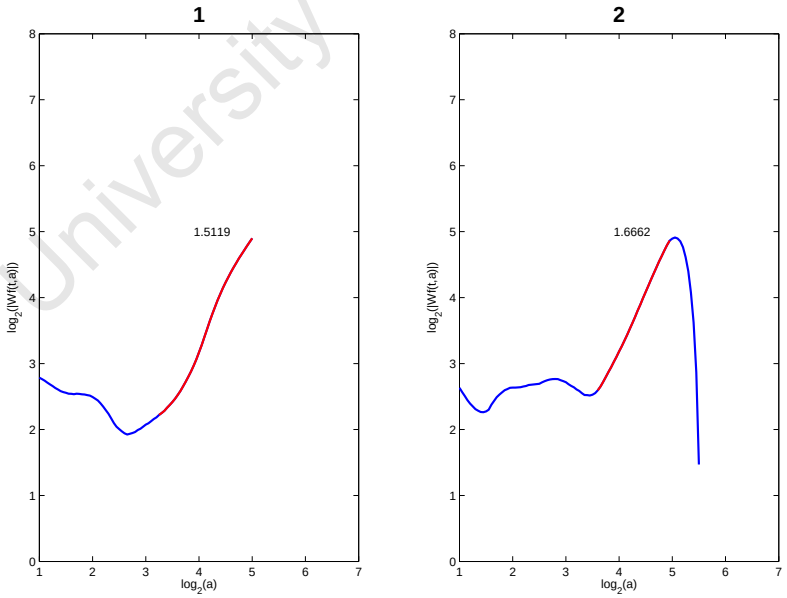

B.41 Valentia (VAL)

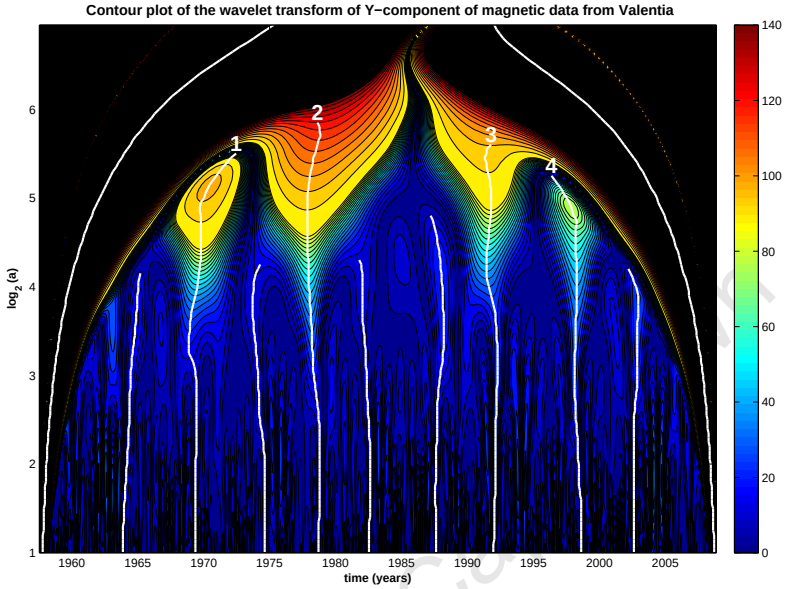

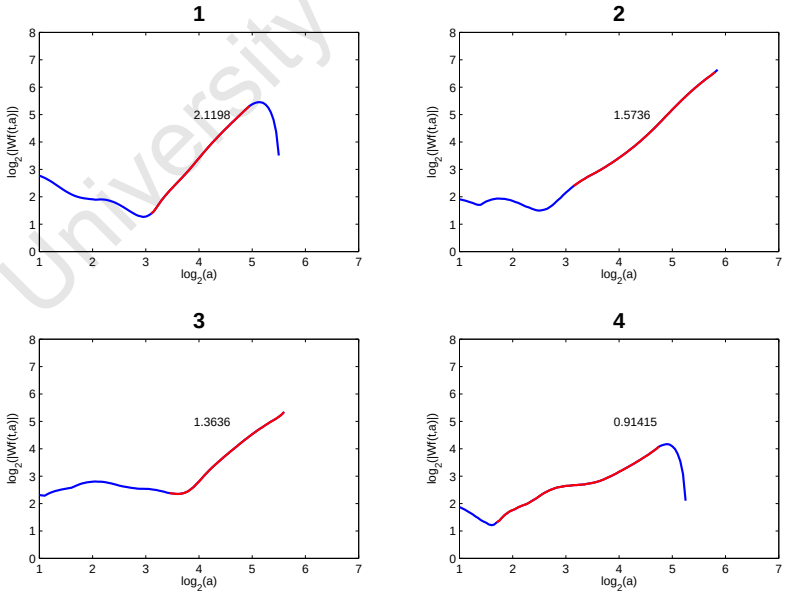

B.42 Victoria (VIC)

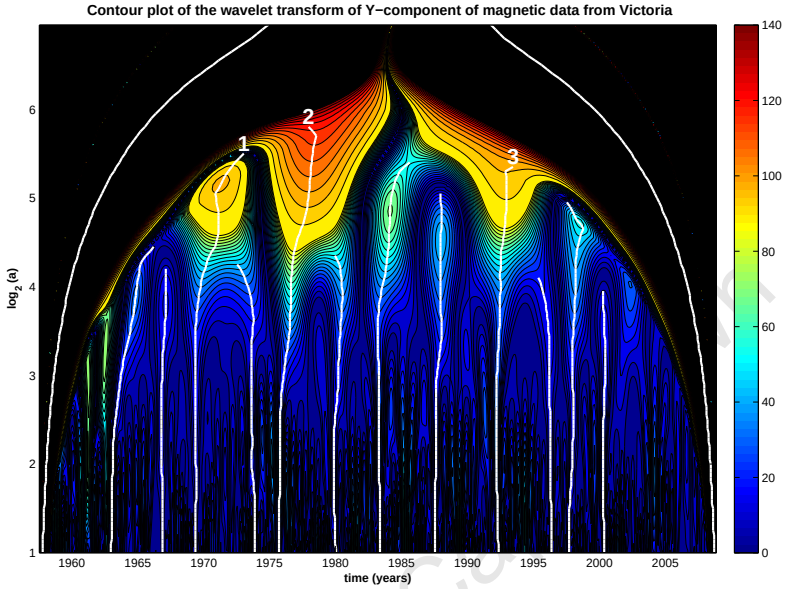

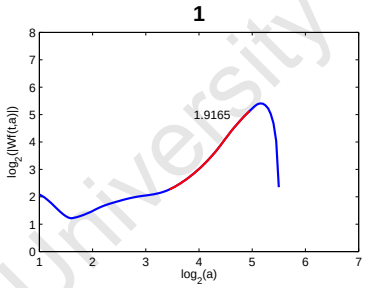

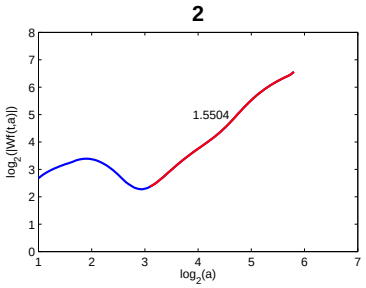

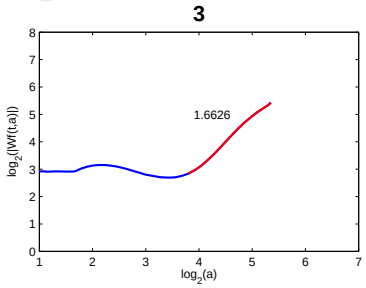

B.43 Watheroo (WAT)

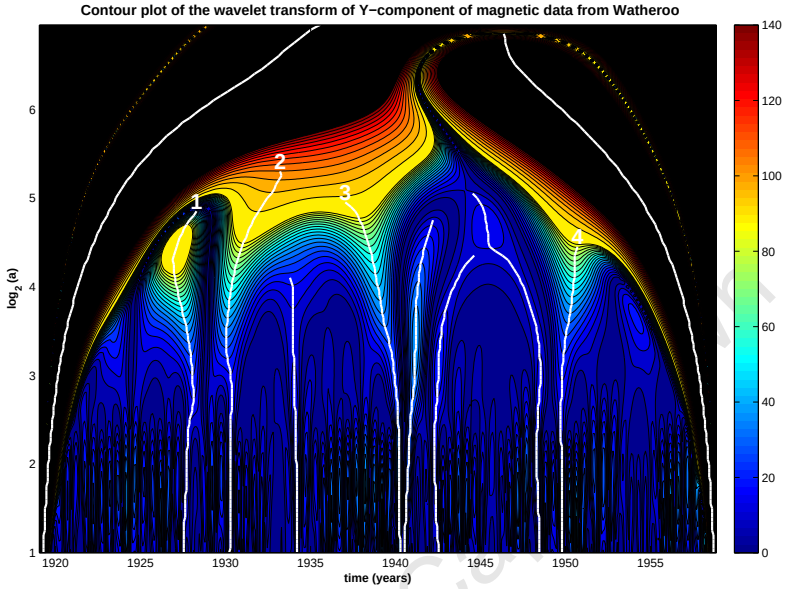

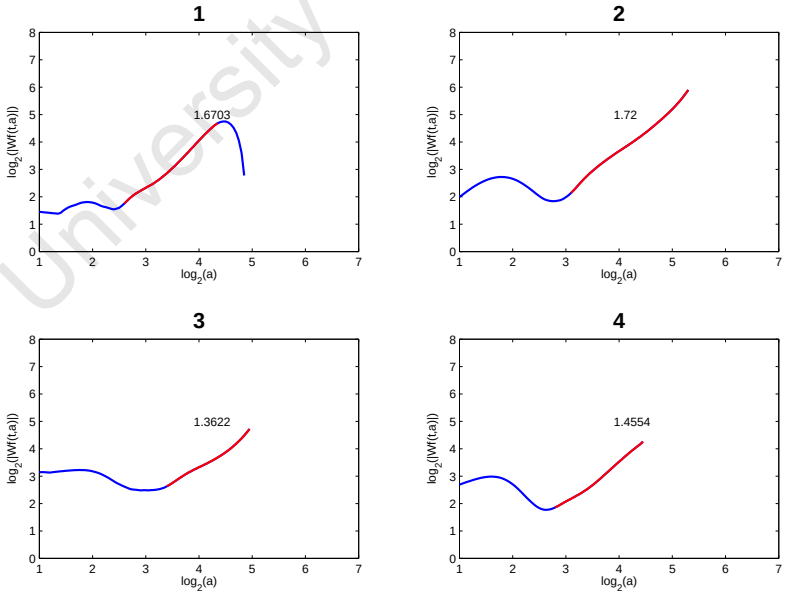

B.44 Wingst (WNG)